Title
Understanding correlated insulating ground states of magic-angle twisted bilayer graphene

Author
Soejima, Tomohiro

Publication Date
2023

Peer reviewed|Thesis/dissertation

Understanding correlated insulating ground states of magic-angle twisted bilayer graphene

by

Tomohiro Soejima

A dissertation submitted in partial satisfaction of the

requirements for the degree of

Doctor of Philosophy

in

Physics

in the

Graduate Division

of the

University of California, Berkeley

Committee in charge:

Professor Michael Zaletel, Chair
Professor Ehud Altman
Professor Daniel Bediako

Summer 2023

Understanding correlated insulating ground states of magic-angle twisted bilayer graphene

Abstract

Understanding correlated insulating ground states of magic-angle twisted bilayer graphene

by

Tomohiro Soejima

Doctor of Philosophy in Physics

University of California, Berkeley

Professor Michael Zaletel, Chair

When two layers of graphene are put on top of each another with a relative twist, their lattice mismatch gives rise to a moiré pattern. When the twist angle is near 1.1 degrees, a so-called magic angle, the band structure of twisted bilayer graphene becomes extremely flat around the Fermi energy, enhancing the effect of electron-electron interaction. Remarkably, magic-angle twisted bilayer graphene (MATBG) becomes superconducting at low temperatures. The origin of this superconducting behavior remains elusive.

Curiously, the superconducting behavior is usually accompanied by correlated insulating behavior in nearby parameter regions in the phase diagram. These correlated insulators cannot be described by non-interacting band theory, hinting at the importance of electron-electron interaction.

In this thesis, we attempt to understand these correlated insulators by a combination of numerical and analytical techniques. On the numerical side, we will utilize the density-matrix renormalization group (DMRG) extensively to obtain the ground states of MATBG. Owing to the complexity of the problem, this required us to develop a non-trivial routine for encoding the Hamiltonian. We find that DMRG often reproduces the findings from Hartree-Fock simulations. On the analytical side, we aim to understand different symmetry-breaking states of MATBG. Based on symmetry analysis, we propose using scanning tunneling microscopy (STM) to distinguish between different candidate ground states, and test our analytical prediction using numerical simulation.

Taken together, this thesis represents a significant step toward understanding the correlated insulating behavior of MATBG.

Contents

List of Figures

List of Tables

Acknowledgments

First and foremost, I want to thank my PhD advisor Prof. Mike Zaletel for his constant encouragement and passion for science. As I was choosing between experimental chemistry, experimental condensed matter physics, and theoretical condensed matter physics before joining grad school, it was his encouragement that convinced me to pursue theory. It was the right decision. I am happy to have learnt so much under him.

Perhaps the most important lesson of grad school was how comparatively little I can accomplish on my own, and how much more I can do with the help of others. I therefore want to thank Karthik Siva, Shubhayu Chatterjee, Nick Bultinck, Dan Parker, Sajant Anand, Jung Pyo Hong, Patrick Ledwith, Yijian Zou, Ryohei Kobayashi, Rahul Sahay, and Stefan Divic. You have helped me become a better scientist, and our collaboration was the most important source of enjoyment during my research career.

While I have not had the privilege of working with them, the rest of the CMT community has made my time on the fifth floor of Birge truly intellectually stimulating. The many many discussions we had in front of the white boards in the interaction room form my intellectual backbone.

I would be remiss not to mention my experimental collaborators, Canxun Zhang, Tiancong Zhu, Mike Crommie, Hryhoriy Polshyn, Andrea Young, Kevin Nuckolls, Ryan Lee, Myungchul Oh, Dillon Wong, and Ali Yazdani. Their hard work let me connect my simplified theoretical models with experimental reality. I do not pretend to know how hard it must be to get such high quality data, but I am happy to have been of some help in making sense of them.

Dan Parker's name deserves a second mention. Since his time as a graduate student at Berkeley and through his time as postdoc at Harvard, he has been an important collaborator, mentor, and a friend to me. His high standard for scientific communication has always inspired me to do better. Best of luck at UCSD!

I want to thank scientific mentors of mine from before my graduate school days: Nobuhiro Kihara, Carl Brozek, Mircea Dincă, Micheal Campbell, Lei Sun, Tomohiro Takayama, and Hidenori Takagi. I was fortunate to have learned so much experimental chemistry and physics under them. While five years away from lab has all but annihilated whatever experimental competence I used to have, I still carry with me the lessons I learnt from my experimental days about critically evaluating scientific results.

My junior high school teacher, Hiroshi Goto, deserves a special thanks. He instilled in me a passion for science, and my experience in the science club as built me the foundation of my scientific communication skills. I would not be where I am today without his passion for scientific education through research.

I remember the first occasion Chitraang Murdia offered to cook me something as we were walking down Telegraph. Little did I know he would end up feeding me and many others in the cohort for so many years. Our 1'Monday dinners" were my favorite social event at Berkeley. I was lucky to have Lizzy Dresselhaus as a friend and a colleague. Our "Quantum Gravity" performance together with Ezra at the physics holiday party remains a highlight

of my (admittedly limited) musical career. I hope the three of us will reconvene on the East Coast next time around.

I want to thank Daniel Gardeazabal, Max Smiley, Trevor Chistolini, and Chris Madsen for great Pathfinder sessions. Starting at the peak of the pandemic, our weekly sessions were a great source of reprieve even when things were crazy. I will miss playing the part of an egocentric diva.

Of my many friends outside of my cohort, I am particularly thankful to Stephen Chen, James Rowan, and Diptarka Hait for their friendship. Even in the age of remote work, it is impossible to understate the importance of proximity to friendship. I got to know them better through our many years together at MIT and Berkeley, and I hope we will remain in touch.

To close, I want to thank my family for their continued support. It must have been a surprise to my parents when their 17-year old son insisted on studying abroad. They have supported this unconventional decision of mine, and showed me how much they valued my academic development. I also want thank my grandparents for their constant support. Finally, I want to thank my wife Hana for her love and perseverance.

Chapter 1

Introduction

1.1 Brief history of magic-angle twisted bilayer graphene (MATBG)

Superconductivity in magic-angle twisted bilayer graphene was first reported in March 2018 in a jam-packed conference room at the APS March meeting in Los Angeles, concurrently with the publication of two articles [1, 2] that detailed the correlated insulating behavior and superconducting behavior of the system.

History tells us that new superconducting materials are uniquely good at exciting condensed matter physicists, and MATBG was no exception. The discovery was quickly reproduced (e.g. by Ref. [3]), and a flood of theoretical works attempted to explain the physics of MATBG. With the help of some hindsight, we can understand why the problem attracted so much attention:

1. The constituent material, monolayer graphene, has a simple description using a tight-binding model. Since its discovery in 2005, its properties have been extensively characterized, and high quality samples were readily available.

2. Two-dimensional materials can be probed by a wider array of techniques than three-dimensional materials, including 1) the ability to change electron-doping by gating, and 2) direct access using surface probes such as scanning-tunneling microscopy (STM).

3. There was a well-motivated theoretical starting point in the form of the Bistritzer-McDonald model (BM model) [4].

4. The prediction of the BM model indicated that electrons have small kinetic energy (flat band) for certain twist angles near the so-called magic angle, suggesting that it is a strongly-correlated electron system.

Many of these properties carry over to other two-dimensional materials. Starting from materials with more layers of graphene (monolayer-bilayer, chiral trilayer, and chiral tetralayer

and beyond), we also have a long list of moiré materials made from transition metal dichalcogenides (TMDs). However, MATBG has remained one of the most exciting materials in this newly emerging field.

In the rest of the introduction, we will briefly review the physics of MATBG, and highlight the main challenges in understanding its physics.

1.2 What does twisting do to graphene?

Let us begin by asking what happens upon twisting two layers of graphene with respect to each other when we limit ourselves to non-interacting description.

To start, we should understand the physics (and chemistry) of monolayer graphene. Graphene is a two-dimensional material made of a honeycomb lattice of carbon atoms. The four valence electrons of each carbon atom hybridize to form sp^2 orbitals and a p^z orbital. The former forms strong in-plane σ bonds, providing strong binding force between carbon atoms. For condensed matter physics, however, we focus our attention on p^z orbitals, which are lower-energy, and therefore more accessible, degrees of freedom.

The behavior of carbon p^z electrons is well-described by a nearest neighbor tight-binding model on a honeycomb lattice. Upon solving the tight-binding model, we find that 1) the Fermi energy crosses graphene bands at two separate "valleys", and 2) the dispersion relation near the valleys can be described by that of a massless Dirac electron:

$$H(\mathbf{k} \approx K) = -v_F(\mathbf{k} - K) \cdot \sigma, \tag{1.1}$$

where K is the momentum of one of the valleys, $\sigma = (\sigma_x, \sigma_y)^T$ is a vector of Pauli matrices, and the Hamiltonian at the other valley is given by time reversal. Therefore, we can treat electrons in graphene as consisting of two species of massless Dirac electrons.

When we put two layers of graphene on top of each other, we are allowing Dirac electrons to tunnel from one layer to the other. If the two layers are in the unrotated, stable "Bernal" structure, the result is a quadratic band dispersion [5].

The relative rotation between the two layers introduces a "twist" into this story. The lattice mismatch between the top layer and the bottom layer gives rise to a moiré superlattice. The size of the superlattice is determined by the ratio between the mismatch and the lattice constant. Concretely, given the reciprocal lattice vector of graphene G_i and the twist angle θ, the reciprocal lattice vectors for moiré superlattice are given by

$$g_i = (R(\theta/2) - R(-\theta/2))G_i, \tag{1.2}$$

where $R(\theta)$ is the rotation matrix. We see that a small rotation angle θ gives rise to a small g_i, and therefore a large moiré superlattice. As a result, the tunneling between the two layers become spatially modulated with the same periodicity as the moiré superlattice, altering the bandstructure.

At first sight, the task of computing the bandstructure of twisted bilayer graphene appears daunting. The computation will need to keep track of all carbon atoms in a moiré unit cell,

which could be as large as 10,000 even at the modestly small twist angle of 1 degree. However, it turns out that a small twist angle allows for a continuum approximation [6]. By focusing only on low-energy degrees of freedom, the continuum approximation greatly reduces the complexity of the problem, and we can quite accurately obtain the low-energy bandstructure of twisted bilayer graphene. Remarkably, Bistritzer and MacDonald noticed that two low-energy bands at the Fermi energy become extremely flat around a series of "magic" angles, the largest of them being around 1.1 degree. Twisting, therefore, significantly alters the electronic properties of twisted bilayer graphene.

The flatness of the bands means that the kinetic energy is quenched, enhancing the importance of electron-electron interaction, giving rise to a wider range of interesting possibilities. The effect of electron-electon interaction in magic-angle twisted bilayer graphene (MATBG), however, could not be understood based on the non-interacting BM model. Therefore, the experimental observation of superconductivity and correlated insulators in MATBG came as quite a bit of surprise.

1.3 Superconductivity and correlated insulating behavior in MATBG

A long line of experiments, starting with the initial reports [1, 2] have now established that MATBG shows striking phenomena: superconductivity, mostly at fractional number of electrons per moiré unit cell, and correlated insulating behavior at integer filling.

While the appeal of superconductivity is immediately clear to many of us, one may wonder why correlated insulating behavior is a mystery worth our attention. After all, there are many more insulators in the world than there are superconductors. However, the presence of these correlated insulating states serve as a strong indirect evidence for the importance of electron-electron interaction in MATBG. To see this, we must understand why we are justified in calling them "correlated" insulators. Suppose, for the moment, that the system is described by non-interacting electrons. The band structure tells us MATBG should be (semi-)metallic at electron filling fraction between -4 and 4 [1]. This is because there are two connected bands around the Fermi energy, and they are four-fold degenerate from spin and valley degrees of freedom. We must go beyond band theory by taking electron-electron interaction and correlation into account to understand correlated insulating behavior [2].

[1] The filling is measured with respect to charge neutrality

[2] To someone with quantum chemistry backgroud, our use of the term "correlation" might appear strange. In quantum chemistry parlance, correlation energy is defined as the difference between the true ground state energy and the variational energy obtained from Hartree-Fock calculation. In condensed matter physics, it is common to refer to phenomena driven by electron-electron interaction as electron-electron correlation, regardless of the resulting state is Slater-determinant like or not. In some cases, such as those we describe in Chapters 2 and 3, the ground state might be very close to a Slater determinant, but we still call them correlated insulators

One way electron-electron interaction can go beyond the non-interacting theory is by driving spontaneous symmetry breaking (SSB). For example, it can give rise to a ferromagnet from the following mechanism: Due to the Pauli exclusion principle, electron interaction acts differently between different species of electrons. If the system consists of spin-up electrons, adding a spin-up electron costs less interaction energy than adding a spin-down electron [3]. In the language of band theory, this means the energy of the spin-up bands becomes lower than the energy of the spin down bands, giving rise to a ferromagnet. If the shift is large enough, we can obtain a state with full polarization. As this state fully filles the spin-up bands while keeping the spin-down bands empty, the state is an insulating ferromagnet.

MATBG hosts a wealth of symmetries that can be broken, giving rise to a large family of possible SSB insulators. The original BM model contains $U(2) \times U(2)$ symmetry corresponding to independent charge and spin conservation within each valley. In addition, a series of careful theoretical analysis has found a limit of MATBG Hamiltonian where the symmetry is enhanced to $U(4) \times U(4)$ [7–9]. The interacting Hamiltonian can be solved exactly in this limit, and the ground states are shown to be SSB states with distinct symmetry properties. We will spend the bulk of this thesis on trying to understand various SSB insulators, some related to this solvable limit, some not.

It is worth stressing that it is *a priori* not obvious whether superconductivity observed in MATBG is a strongly correlated phenomenon. It is hard to exclude a more conventional possibility, such as BCS superconductor mediated by electron-phonon coupling. However, the presence of correlated insulators in proximate regions of the phase diagram hints at the important role electron-electron interaction plays for superconductivity. At the very least, it shows that a model of MATBG without electron-electron interaction is woefully incomplete.

In fact, there has been a proposal that electron-electron interaction might play a more direct role in establishing superconductivity [10]. In the so-called "skyrmionic superconductivity" theory of MATBG, we start from one of the many broken symmetry insulators. These insulators support topological skyrmions that carry charge. A subtle interplay between skyrmion physics and the band topology of MATBG acts to create a binding force for charged skyrmions, creating skyrmionic Cooper pairs. Such prediction further enhances the importance of understanding the correlated insulators.

1.4 Numerical challenges of simulating MATBG

Away from the aforementioned exactly solvable limit, it is difficult to obtain the ground states of MATBG analytically. We must therefore turn to numerical simulations.

Arguably the most principled approach is to perform *ab initio* calculations with all 10,000 carbon atoms. However, the large number of atoms involved makes this task quite challenging. Moreover, the standard methods used for solid state *ab initio* tasks, such as the density functional theory (DFT), are inadequate for capturing correlated phenomena. While DFT can serve as a useful guide, especially when it comes to less correlated phenomena such as

[3] This is nothing other than the exchange energy and the Hund's coupling in chemistry parlance

the deformation of the lattice structure in the presence of twist, they cannot be trusted to understand low-energy correlated behavior of MATBG.

Luckily, we can reduce the number of degrees of freedom drastically from $O(10,000)$ by projecting to low-energy part of the Hilbert space. The band structure obtained from the BM model provides a natural starting point for this: we can project our Hilbert space to the two flat bands near the Fermi energy[4]. We can then apply computationally intensive techniques, such as those we describe below, within this subspace.

A popular choice has been the Hartree-Fock(HF) method. It is a variational algorithm based on Slater determinants. It can correctly capture the aforementioned SSB insulators in the exactly solvable limit, and if the ground state remains similar to the SSB insulators, we expect the HF method to work well. However, the method is known to overestimate the degree of electron localization, and often give an insulating solution even when the true ground state is metallic. We therefore need a more unbiased approach to tackle this problem.

Our method of choice is the density-matrix renormalization group (DMRG) method [11], which is known to work well for 1D systems. We apply this method to 2D MATBG by considering putting it on a finite×infinite cylinder geometry. DMRG is a variational method based on matrix product states (MPS), where we represent quantum states by a product of matrices. It is unbiased in the following sense: the variational set is dense in the space of states in the limit of the matrix dimension going to infinity. DMRG can thus go beyond the Hartree-Fock method.

Performing DMRG on MATBG comes with its own set of challenges. Even after projecting to a subspace, the Hamiltonian is highly complex. Electrons interact via long-range Coulomb interaction, and we must keep track of many terms to accurately represent this interaction. If we do this in a brute-force manner, the computational cost of representing the Hamiltonian becomes prohibitively high. We will spend much of Chapter 2 on how we solve this challenge.

1.5 A tiny strain on moiré changes physics of MATBG

A recurring theme in the study of MATBG is that a seemingly minor perturbation can drastically alter its physics. Consider stretching the top layer of graphene by a small amount ϵ. This changes the reciprocal vector of the top layer from $R(\theta/2)G_i$ to $(R(\theta/2)+\epsilon)G_i$. The new moiré reciprocal lattice vector is now given by

$$g_i' = (R(\theta/2) + \epsilon S - R(-\theta/2))G_i, \tag{1.3}$$

where S is a 2 by 2 matrix with entries of size $O(1)$ that characterize the response of graphene to stretching. Therefore, the change of the reciprocal lattice vector is given by

[4]When using less computationally-demanding methods such as Hartree-Fock, we sometimes include more than two bands

$\Delta g_i = g_i' - g_i = \epsilon S G_i$. Noting $|g_i| \sim |\theta||G_i|$, we see g_i changes by ratio $\sim \epsilon/\theta$. When θ is small, as is the case for MATBG, even a tiny ϵ can cause a large change in the moiré superlattice. For example, an ϵ of order 0.1% can change g_i by around 5%.

The change in the geometric structure is accompanied by the change in electronic structure, stabilizing states that are not competitive in the absence of strain. In Chapter 3, we take a careful look at the effect of strain, showing the existence of a quantum phase transition driven by a change in strain.

Our subsequent numerical works [12, 13] considered the effect of strain at a broader region of the phase diagram. We identified yet another state called Incommensurate Kekulé spiral (IKS) can be stabilized by strain. This further underscores the importance of taking such seemingly small perturbation seriously.

1.6 How can I see SSB in MATBG?

Theoretical and analytical works on MATBG, including those done by us, strongly support SSB in the ground states. It is, however, an altogether different problem to ascertain the nature of the ground state experimentally. One of the challenges is in the large symmetry of MATBG. In addition to $U(2) \times U(2)$ symmetry coming from spin rotation in each valley, we must also take into account the space group symmetry of MATBG. No single experimental method can probe all these symmetries simultaneously, so we must wisely identify the best probe for detecting SSB.

Scanning tunneling microscopy (STM) is a promising candidate for this task, since it can access spatially-resolved properties of MATBG. The best STM devices available can achieve atomic resolution, a feat nigh impossible for most other probes.

To make the most out of the incredible precision of STM, we must understand how various competing ground states appear under STM. In Chapter 4, we describe a Hartree-Fock based study on this question. We identify that different ground states of MATBG have clearly observable signal in STM.

Subsequent to our theoretical prediction, an STM study on MATBG indeed confirmed atomic-scale symmetry breaking [14]. In fact, based on a theoretical analysis we developed, we could identify the STM data as the aforementioned IKS state. While there are many more mysteries to be resolved, this kind of fruitful interaction between theory and experiment will undoubtedly further our understanding of this intriguing system.

1.7 Organization of the rest of the thesis

- In Chapter 2, we describe the method for performing DMRG calculations of MATBG. Because of the long-range Coulomb interaction and the large number of orbital degrees of freedom, tBLG is difficult to study with standard DMRG techniques — even constructing and storing the Hamiltonian already poses a major challenge. To overcome

these difficulties, we use a recently developed compression procedure to obtain a matrix product operator representation of the interacting tBLG Hamiltonian which we show is both efficient and accurate even when including the spin, valley and orbital degrees of freedom. To benchmark our approach, we focus mainly on the spinless, single-valley version of the problem where, at half-filling, we find that the ground state is a nematic semimetal. Remarkably, we find that the ground state is essentially a k-space Slater determinant, so that Hartree-Fock and DMRG give virtually identical results for this problem. The content of this chapter is based on [15].

- In Chapter 3, we consider the effect of strain on MATBG. Using both self-consistent Hartree-Fock and density-matrix renormalization group calculations, we find that small strain values ($\epsilon \sim 0.1 - 0.2\%$) drive a zero-temperature phase transition between the symmetry-broken "Kramers intervalley-coherent" insulator and a nematic semi-metal. The critical strain lies within the range of experimentally observed strain values, and we therefore predict that strain is at least partly responsible for the sample-dependent experimental observations. The content of this chapter is based on [16].

- In Chapter 4, we tackle the problem of experimentally identifying symmetry breaking in MATBG. We show how atomically-resolved scanning tunneling microscopy can be used as a fingerprint of symmetry breaking order. By analyzing the pattern of sublattice polarization and "Kekulé" distortions in small magnetic fields, order parameters for each of the most competitive symmetry-breaking states can be identified. In particular, we show that the "Kramers intervalley coherent state," which theoretical work predicts to be the ground state at even integer fillings, shows a Kekulé distortion which emerges only in a magnetic field. The content of this chapter is based on [17].

Chapter 2

Density matrix renormalization group study of twisted bilayer graphene

2.1 Introduction

Magic angle twisted bilayer graphene (tBLG) hosts a diverse array of correlated insulating and superconducting phases [1–3, 18–37]. This rich system has inspired intensive theoretical efforts to understand the origin and mechanism(s) behind these phases, and a large number of theories already have been proposed. One way to assess these proposals — especially when they are not associated to clear experimental signatures — is numerical calculation. To that end, this chapter presents a proof-of-concept density matrix renormalization group (DMRG) [11] study of a microscopically realistic, strongly interacting model of tBLG.[38]

Challenges of tBLG Numerics

Let us review what makes the tBLG problem so numerically challenging, and identify a viable path around the obstacles. The first obstacle is the separation in scales between the graphene lattice constant a and the moiré length scale L_M; at the magic angle $L_M/a \sim 1/\theta_M \sim 50$, so the moiré unit cell contains over $10,000$ carbon atoms, and consequently the superlattice band structure contains $N_B \sim 10,000$ bands. Fortunately, various treatments of the band structure [4, 39–41] (including the Bitzritzer-MacDonald (BM) continuum model [4] used here) reveal that the flat bands of interest are separated from the tower of "remote" bands by gaps of order 20 meV–25 meV (see Fig. 2.2(c)). Since these gaps are larger than the Coulomb scale $E_C = \frac{e^2}{4\pi\epsilon_0\epsilon_r L_M} \sim 10\,\text{meV}$–$20\,\text{meV}$ (using a relative permittivity $\epsilon_r = 12 - 6$), it is a reasonable starting point to project the Coulomb interaction $V(r)$ into the flat bands.[1] Each spin and valley of the graphene has *two* flat bands, for a total of eight, winning us a

[1] Hartree-Fock studies which include the remote bands do find that they have a quantitative effect (for example, on the magnitudes of the symmetry-broken gaps), but there are some discrepancies regarding their qualitative importance [8, 42].

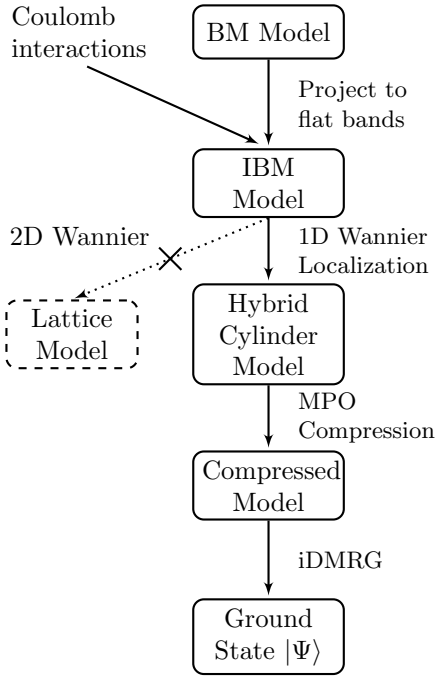

Figure 2.1: Flowchart of our approach to DMRG for tBLG. First we start from a continuum BM model, and add Coulomb interactions, projected to the flat bands to reduce the number of degrees of freedom down to a manageable level. Second, we perform hybrid Wannier localization, which maps the model to a cylinder in mixed-xk space, thereby avoiding a topological obstruction and allowing all symmetries to act locally. Third, we use a compression procedure to represent the long-range interactions with a reasonable bond dimension to make DMRG numerically tractable. This allows us to perform DMRG with all $N_B = 8$ components at moderate cylinder radius ($L_y = 6$).

reduction from $N_B = 10,000 \searrow 8$. We refer to this as the "Interacting Bitzritzer-MacDonald (IBM) model," although our method works just as well for improved continuum models of tBLG which take into account effects like lattice relaxation. The touching of these two bands is locally protected by a crucial $C_2\mathcal{T}$ symmetry (a 180-degree rotation combined with time-reversal), which distinguishes tBLG from other moiré materials. The Coulomb scale E_C is much larger than the bandwidth $t \sim 5\,\text{meV}$, so *a priori* unbiased, strongly-interacting numerical approaches such as exact diagonalization [43], determinantal quantum Monte Carlo, or DMRG are required.

Most strongly-interacting approaches proceed from a real space lattice model, so a natural next step is to construct a lattice model via 2D Wannier localization of the continuum Bloch bands. In real space, the density of states of the flat bands is predominantly located on the AA-stacking regions of the moiré unit cell, which form a triangular lattice (see Fig. 2.2d). So one might hope that the physics is then well-described by an 8-component triangular lattice Hubbard model. However, there is a topological obstruction which complicates this approach: the flat bands possess "fragile topology" which makes their Wannier localization

very subtle [41, 44–49]. In particular, the presence of $C_2\mathcal{T}$, valley conservation $U_v(1)$ and translation make it impossible to Wannier localize the flat bands in a manner where $U_v(1)$ and $C_2\mathcal{T}$ both act in a strictly local fashion. This is somewhat analogous to the obstruction to finding a Wannier basis for a 2D topological insulator under the requirement that $\mathcal{T}$ acts as a permutation of the orbitals [50].

Two resolutions to the Wannier obstruction issue have been proposed in the literature. The conceptually simplest is to include some number of remote bands, at minimum $N_B = 8 \to 20$, which removes the topological obstruction and allows for a local symmetry action [45]. But from a DMRG standpoint, a model with 20 orbitals per unit cell, all strongly-interacting, appears to be numerically intractable. The other approach is to simply ignore the symmetry considerations and Wannier-localize in a basis which hybridizes different valleys or $C_2\mathcal{T}$ sectors. In this approach, for example, valley number conservation $U_v(1)$ becomes slightly non-local, and the associated charge takes the form $Q_V = \sum_{i,j,m,n} Q^{ij}_{mn} \hat{c}^\dagger_{m,i} \hat{c}_{n,j}$ where the sum runs over all sites i, j and internal degrees of freedom m, n. The matrix elements Q^{ij}_{mn} fall off with distance $|r_i - r_j|$ [44]. Intriguingly, the Wannier orbitals then take the shape of three-lobed "fidget spinners" connecting three nearby AA regions [44, 51, 52]. In this basis, the Coulomb interaction is not dominated by a $U\hat{n}^2$ Hubbard interaction, but instead contains a profusion of all allowed $V^{ijk\ell}_{mnop} \hat{c}^\dagger_{m,i} \hat{c}^\dagger_{n,j} \hat{c}_{o,k} \hat{c}_{p,\ell}$ terms which decay exponentially over a few moiré sites [51–53]. Numerically, however, the interactions must be cut off at some finite range, which will spuriously break either the $U_v(1)$ or $C_2\mathcal{T}$ symmetry due to the non-local form they take. This runs the risk of biasing the results by explicitly breaking a symmetry which should be preserved, and would require careful extrapolation of the tails to ensure the correct results. While not necessarily unworkable (in particular, see Ref. [54]), in our estimation this approach makes numerical results delicate to interpret.

Fortunately, DMRG is a 1D algorithm, which allows us to avoid the construction of 2D Wannier orbitals altogether. When DMRG is applied to the cylinder geometry, the model must be in a localized basis along the length of the cylinder, to ensure favorable entanglement properties, but it does not need to be in a localized basis around its circumference. Therefore, we can consider "hybrid" real-space/momentum-space Wannier states which are maximally localized along the length of the cylinder x, but T_y-eigenstates around its circumference y (see Fig 2.3). There is no topological obstruction to the construction of hybrid Wannier states, making them an attractive basis for the flat bands of magic angle graphene, as was also recognized by the authors of Refs. [38, 55–57]. Geometrically, this defines a model on a cylinder, with real-space in the x direction and k-space around the circumference[58]. The hybrid approach allows the $U_v(1)$, $C_2\mathcal{T}$, and translation symmetries to all act locally without adding extraneous degrees of freedom. This is exactly the approach used by Kang and Vafek in their recent DMRG study of tBLG [38], and it is the approach we take as well.

The hybrid approach is not without challenge, however, because upon mapping the orbitals to a 1D fermion chain for input into the DMRG, the effective Hamiltonian is quite long-ranged. The localization width of the Wannier orbitals is comparable to the moiré scale, so all the sites in a single column of the cylinder are strongly overlapping, generating

a panoply of couplings $V^{ijk\ell}_{mnop}\hat{c}^\dagger_{m,i}\hat{c}^\dagger_{n,j}\hat{c}_{o,k}\hat{c}_{p,\ell}$. Though these decay exponentially with distance, a cylinder with circumference $L_y = 6$ with both spin and valley has on the order of $850,000$ non-negligible (i.e. above 10^{-2} meV) matrix elements per unit cell.

A similar problem is encountered in the context of cylinder-DMRG for the fractional quantum Hall effect [59], or finite-DMRG simulations for quantum chemistry problems [60]. There, as here, it is essential to use tensor network methods to "compress" the V^{ijkl} as a matrix product operator (MPO). To do so, we leverage a recent algorithm for black-box compression of Hamiltonian MPOs with various optimality properties [61]. We find that for a circumference $L_y = 6$ cylinder, the spinless / single-valley problem ($N_B = 2$) requires an MPO bond dimension of $D \sim 100$ for physical observable to obtain a relative precision of 10^{-2}, while in the spinful / valleyful $N_B = 8$ case, we estimate the required bond dimension to be $D \sim 1000$. While large, these values are tractable, especially when exploiting the charge, spin, valley, and k_y quantum numbers.

Overview of DMRG Results

After presenting details of the interacting tBLG Hamiltonian and its MPO compression, we apply our approach in detail to a "toy" $N_B = 2$ problem in which we keep only valley K and spin $\uparrow$; more physical models will be considered in the next chapter. When filling 1 of the 2 bands, this scenario is conceptually similar to fillings $\nu = -3, 3$ of tBLG under the assumption that these fillings are spin and valley polarized. However, we caution the reader that our results are not a quantitative prediction for these fillings because the toy model differs from $|\nu| = 3$ of tBLG by a $4\times$ difference in the magnitude of the Hartree potential generated relative to neutrality. We've made this choice so that we can quantitatively compare with Refs. [38] prior results; the "physical" $|\nu| = 3$ result, which differs in some interesting respects, will be presented in a future work [13].

Following Ref. [38], we fix $\theta = 1.05°$ and vary the ratio of the AA and AB inter-layer tunneling hopping strengths w_0/w_1 from 0 to 0.9. While physically $w_0/w_1 \sim 0.8$ [39, 40, 52], the resulting phase diagram is conceptually interesting because the dominant effect of w_0/w_1 is to redistribute the Berry curvature of the flatbands, rather than changing their bandwidth, revealing that the former is crucial to the physics. As a précis of our findings,

1. In agreement with Ref. [38], we find that below a critical value $w_0/w_1 \lesssim 0.8$, the ground state spontaneously breaks the $C_2\mathcal{T}$ symmetry, forming a quantum anomalous Hall state (Chern insulator), with $C = \pm 1$.

2. In agreement with Ref. [38], above $w_0/w_1 \gtrsim 0.8$, the $C_2\mathcal{T}$ is restored. In this region the DMRG results of Ref. [38] did not reliably converge, but their mean-field calculations suggested either a "nematic $C_2\mathcal{T}$ symmetric semimetal" first proposed in Ref. [62], or a gapped $C_2\mathcal{T}$-symmetry stripe [38]. Our DMRG numerics reliably converge to a state in excellent agreement with the nematic $C_2\mathcal{T}$-semimetal, with two band touchings near the Γ point.

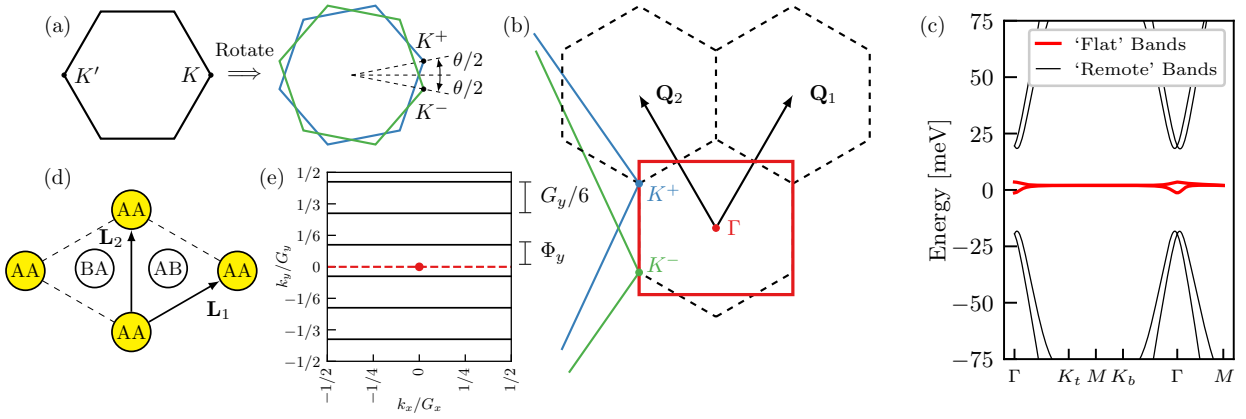

Figure 2.2: (a) The BM model for bilayer graphene is constructed from two regular graphene Brillouin zones, rotated by $\pm\theta/2$. (b) Zoomed view of (a) showing the mini (or moiré) Brillouin zone. We choose a square mBZ (thick red lines) for numerical convenience. (c) The band structure of the BM model over the mBZ showing the flat bands (red lines). The interacting BM model is defined by adding Coulomb interactions to the BM model and projecting to the flat bands. (d) Schematic of the real space moiré unit cell with Bravais lattice vectors $\mathbf{L}_{1,2}$. (e) The IBM model on a cylinder has N_y discrete momentum cuts at k_y values given by Eq. (2.3), offset by Φ_y.

3. We analyze the k-space electron correlation function $P_{mn}(\mathbf{k}) = \langle c^\dagger_{n,\mathbf{k}} c_{m,\mathbf{k}} \rangle$ of the DMRG ground state, which can be directly compared with Hartree-Fock calculations. We find that both phases are extremely well captured by a single k-space Slater determinant (to within $\approx 1\%$), strongly supporting the validity of recent Hartree-Fock studies [8, 18, 35, 38, 42, 56, 57, 62–64].

4. Finally, we compare the energy of the DMRG ground state with various competing variational ansatz such as the $C_2\mathcal{T}$-stripe ansatz proposed in Ref. [38]. In agreement with their result, we find that the nematic semimetal and the $C_2\mathcal{T}$ stripe compete at the order of 0.1 meV per unit cell.

The remainder of this chapter is organized as follows. Section 2.2 introduces our model: an interacting Bistritzer-MacDonald model, equipped with long range Coulomb interactions, and projected to the flat bands. Section 2.3 discusses how the model may be expressed as a Matrix Product Operator and both why and how it must be compressed to perform DMRG. Section 2.4 provides the results of DMRG calculations, and shows that Hartree-Fock accurately captures the ground state physics in this model. Section 2.5 discusses the nature of the nematic $C_2\mathcal{T}$-semimetal. We conclude in Section 2.6. Extensive Appendices describe all details needed to reproduce our results. Appendix A.1 details the IBM model. Appendix A.2 deals with the Wannier localization and the gauge choice we make. App. A.3 constructs the pre-compression MPO: an infinite MPO with arbitrary long range 4-body interactions. App. A.4 provides the algorithm for MPO compression, as well as rigorous error bounds.

Finally, App. A.5 explains the extensive numerical cross-checks we performed to ensure the accuracy of our results.

2.2 The IBM Model

This section describes the interacting generalization of the Bistritzer-MacDonald (BM) model. We first briefly recall the BM model and the geometry of the mini-Brillouin zone (mBZ), then discuss how interactions are added. We then show how the model can be placed on a cylindrical geometry, and conclude with the symmetries of the model.

Continuum Model

Our starting point is the single-particle Bistritzer-MacDonald (BM) model [4], composed of two layers of graphene, with relative twist angle θ, coupled together by a spatially-varying moiré potential. The potential is governed by two parameters, w_0 and w_1, which specify the AA / AB interlayer tunneling respectively. DFT calculations which account for lattice relaxation find that $w_1 = 109\,\text{meV}$ and $w_0/w_1 \approx 0.8$ [39, 40, 52], but here we will treat w_0/w_1 as an axis of the phase diagram. We maximize the ratio of band gap to band width for the flat bands by setting $\theta_{BM} \sim 1.05°$. Figure 2.2 details our choice of conventions. In particular, we work with a rectangular mBZ grid for numerical convenience.

We now define an interacting Bistritzer-MacDonald (IBM) model where double-gate screened Coulomb interactions are added to the single-particle model. As the interactions are much larger than the spectral width of the flat bands, but smaller than the gap to nearby bands, we expect interactions to act quite non-perturbatively inside the flat bands and perturbatively between seperated bands. We therefore project the interactions to the two flat bands, akin to models of the fractional quantum hall effect [65]. Our presentation will focus on a single spin and valley, but their inclusion is conceptually identical: we promote $2 \to 8$. Consider a vector of fermions $\mathbf{f}_\mathbf{k}^\dagger = \left(f_{1,\mathbf{k}}^\dagger, f_{2,\mathbf{k}}^\dagger\right)$ running over the two nearly flat bands. The Hamiltonian is then given by

$$\hat{H} = \sum_{\mathbf{k}\in\text{mBZ}} \mathbf{f}_\mathbf{k}^\dagger h(\mathbf{k}) \mathbf{f}_\mathbf{k} + \frac{1}{2A}\sum_\mathbf{q} V_\mathbf{q} : \rho_\mathbf{q}\rho_{-\mathbf{q}} : \,. \tag{2.1}$$

The single-particle term $h(\mathbf{k})$ contains not only the flat band energies of the BM model, but also band renormalization terms coming from the interaction with the filled remote bands, and a subtraction to avoid double counting of Coulomb interaction effects. We refer to Appendix A.1 for more details.

The second term in Eq. (2.1) corresponds to the dual gate-screened Coulomb interaction, with A being the sample area and $V_\mathbf{q} = e^2 \tanh(|\mathbf{q}|\, d)/(2\epsilon_r\epsilon_0\,|\mathbf{q}|)$. The screened Coulomb potential depends on two parameters ϵ_r and d, which respectively are the relative permittivity and the distance between the twisted bilayer graphene device and the metallic gates. While

the effective dielectric constant of the typical substrate, hBN, is $\epsilon_r \approx 4.4$, here we use $\epsilon_r = 12$ in order to phenomenologically account for screening from the remote bands of the tBLG A.1. This sets the typical interaction energy scale to be several meV. For the gate distance we choose $d = 10$ nm to facilitate comparison with Ref. [38]. The Fourier components of the flat-band projected charge density operator are given by

$$\rho_{\mathbf{q}} = \sum_{\mathbf{k}\in \mathrm{mBZ}} \mathbf{f}^{\dagger}_{\mathbf{k}} \Lambda_{\mathbf{q}}(\mathbf{k}) \mathbf{f}_{\mathbf{k}+\mathbf{q}}\,, \tag{2.2}$$

where the 2×2 form factor matrices $[\Lambda_{\mathbf{q}}(\mathbf{k})]_{ab} = \langle \psi_{a,\mathbf{k}} | e^{-i\mathbf{q}\cdot\mathbf{r}} | \psi_{b,\mathbf{k}+\mathbf{q}} \rangle$ are defined in terms of overlaps between the Bloch states of the BM model.

The model enjoys several global symmetries: time reversal followed by in-plane rotation $C_2\mathcal{T}$, out-of-plane C_{2x} rotation, and C_3 rotation. We will describe their action on the basis states explicitly below. In summary, the spinless, single-valley IBM model we have described is a strongly interacting many-body problem defined in momentum space over the mini-Brillouin Zone.

Cylinder Model

Our goal is to perform quasi-2D DMRG on Eq. (2.1). To this end, we work in an infinite cylinder geometry of circumference N_y with a mixed real and momentum space representation of the model. In the momentum space, this corresponds to having N_y momentum cuts through the mBZ at

$$k_y/G_y = \frac{n + \Phi_y/(2\pi)}{N_y} \pmod 1, \quad 0 \le n \le N_y - 1 \tag{2.3}$$

where Φ_y is the amount of flux threaded through the cylinder, which offsets the y momentum as shown in Fig. 2.2. We will Fourier transform each of these momentum cuts in the x direction, such that our basis states are hybrid Wannier orbitals, periodic in y direction and localized in x direction.[2] We will sometimes call this mixed xk representation.

The choice of real-space basis in the x direction is not unique, but we choose the basis of maximally localized Wannier orbitals. Using the maximally-localized orbitals ensures that the interactions are as short-ranged as possible and hence minimizes the range of the interaction terms in the Hamiltonian and the entanglement of the ground state. Due to the relation between maximal Wannier localization and the Bloch Berry connection $\mathbf{A}_{\mathbf{k}}$, this basis will also make manifest their topology. We perform the change of basis:

$$\begin{aligned} \hat{c}^{\dagger}_{\pm,k_x,k_y} &:= U_{\pm,b}(\mathbf{k}) \hat{f}^{\dagger}_{b,k_x,k_y}, \\ \hat{c}^{\dagger}_{\pm,n,k_y} &:= \int \frac{dk_x}{\sqrt{G_x}} e^{i\mathbf{k}\cdot\mathbf{R}_n} \hat{c}^{\dagger}_{\pm,k_x,k_y}, \end{aligned} \tag{2.4}$$

[2] A further advantage of this mixed representation over "snaking" around a real space cylinder is that k_y becomes a good quantum number, reducing the resource cost for a given radius[58, 66].

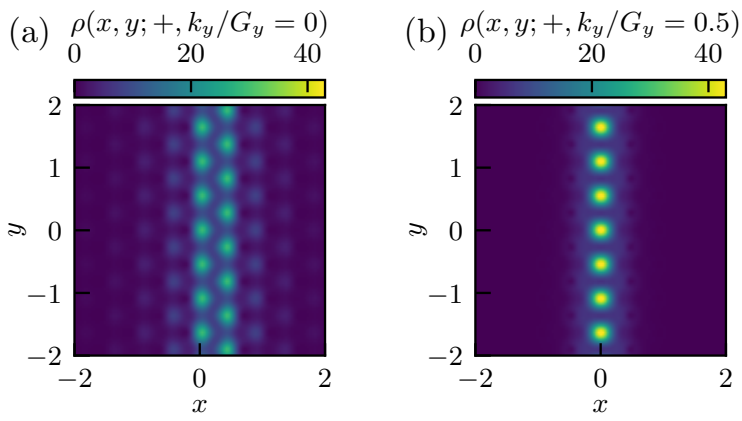

Figure 2.3: Real space charge density of Wannier orbitals. The orbitals are maximally localized in the x direction and periodic along y, with charge densities concentrated in AA stacked regions. The Wannier center and the character changes with k_y.

where $\hat{c}^\dagger_{\pm,n,k_y}$ is the creation operator for the Wannier orbital for unit cell n in the x direction, $\mathbf{R}_n = n\mathbf{L}_1$ with $\mathbf{L}_1$ the Bravais lattice vector, and $U(\mathbf{k})$ is a 2×2 change-of-basis matrix for the internal (band index) degrees of freedom. The non-trivial topology of the tBLG flat bands [41, 44–49] is made explicit in the hybrid Wannier basis by the fact that the states with subscripts $\pm$ are constructed from bands with Chern numbers ± 1. We will explain this in more detail below. We choose the internal rotations $U(\mathbf{k})$ so that the Wannier orbitals are maximally localized (i.e., their spread in the x direction is minimized). Since the problem is effectively 1D for each k_y cut, we can employ a well-known algorithm [67] to deterministically calculate the unique $U(\mathbf{k})$ (up to $(k_y, \pm)$ dependent phases). Fig. 2.3 shows examples of the Wannier orbitals. One can see they are localized in the x direction but extended and periodic in y. The charge density is also not uniform in the y direction, but is concentrated in certain regions corresponding to the AA region [4]. For later notational convenience, we also define $|w(\pm, n, k_y)\rangle = \hat{c}^\dagger_{\pm,n,k_y} |0\rangle$. We emphasize that the $\pm$ basis is not the energy eigenbasis of the single-particle Hamiltonian. In the $\pm$ basis with the gauge convention described later, the $k.p$ expansion of the two band Hamiltonian around $K^\pm$ points takes the form $h(K^\pm + \mathbf{q}) \propto \mp(q_x \cdot \sigma_x + q_y \cdot \sigma_y)$.

A key physical property of Wannier orbitals is their polarization $P_x(\pm, k_y)$, which can be derived via modern theory of polarization [68–71]. They can be thought of as the center of Wannier orbital inside the zeroth unit cell:

$$P_x(\pm, k_y) = \frac{\langle w(\pm, 0, k_y)|\hat{x}|w(\pm, 0, k_y)\rangle}{\mathbf{L_1} \cdot \mathbf{e}_1}, \tag{2.5}$$

where we normalize the polarization by the x extent of the unit cell. The polarization is related to the Berry phase along each momentum cut via the Wilson loop $e^{2\pi i P_x(k_y)} = e^{i \int A_x(k_x, k_y) dk_x / G_x}$, and is only defined modulo 1 [71]. Therefore P_x returns to itself as k_y

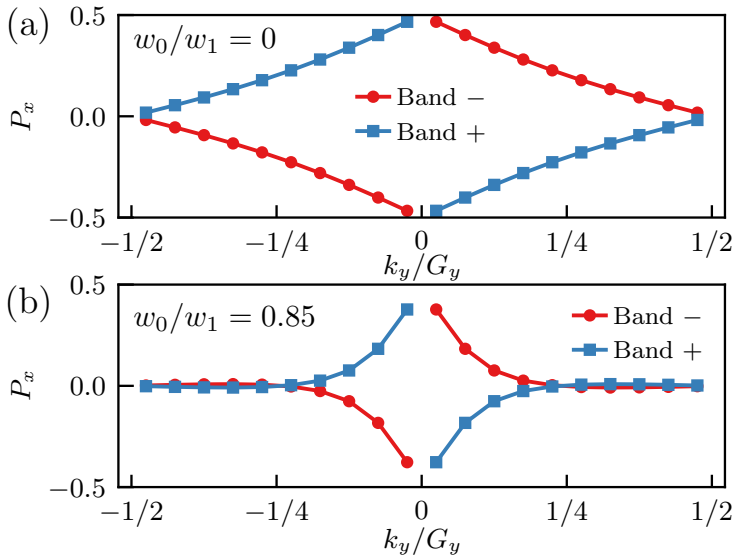

Figure 2.4: Polarization P_x as a function of k_y and w_0/w_1. At each value of w_0/w_1, there are two bands with Chern number ± 1, which wraps once as k_y/G_y increases by 1. This requires a single discontinuity in P_x, which we have chosen to place at $k_y = 0$. One can see that P_x is more linear for $w_0/w_1 = 0$, reflecting flatter Berry curvature.

sweeps across the (mini)BZ. Furthermore, the Chern number of a band is conveniently expressed in terms of the total winding of the polarization, $C = \int dk_y \frac{dP_x}{dk_y}$. In Fig. 2.4, we plot the polarization versus k_y momentum at various different w_0. We make two observations: first, we see that the polarization of the plus (minus) band winds from 0 to 1 (0 to -1) as momentum goes from -0.5 to 0.5. We may therefore identify these bands as having Chern numbers ± 1 — hence our index convention. On the other hand, the profile of the polarization changes as w_0/w_1 increases from 0 to 0.85. At $w_0/w_1 = 0$, the slope is constant, and the Wannier orbitals are almost equally spaced in the x direction, reminiscent of the lowest Landau level of a 2D electron gas in a magnetic field. At $w_0/w_1 = 0.85$, however, P_x is constant for most k_y values, and suddenly changes around the Γ point.

There is a subtle issue relating our convention for polarization to our choice of gauge for single-particle wavefunctions in the mBZ. Since the polarization increases by ± 1 as k_y increases by 2π, we must choose a k_y where the polarization wraps around. We pick the convention that the wrapping $P_x \to P_x \pm 1$ occurs at $k_y = 0$, as shown in Fig. 2.4. In terms of the Wannier orbitals, this means that their centers of charge move continuously with k_y, except at $k_y = 0$ where they "exit" the unit cell and "enter" the neighboring unit cell. In terms of the momentum space creation operator $\hat{c}^\dagger_{\pm,\mathbf{k}}$ this corresponds to a a choice of gauge that is smooth in the upper and lower halves of the Brillouin zone, but *discontinuous* across $k_y = 0$. This discontinuity will appear in several figures below.

Finally, let us give the explicit action of global symmetries on our basis states. We first note the C_3 symmetry of the continuum model is weakly broken by the cylindrical geometry

and is no longer an explicit symmetry of the model. We also note that for flux values $\Phi_y \neq 0 \mod \pi$, the C_{2x} symmetry is not present.

Similar to Ref. [38], we partially fix the gauge of the flat band Bloch states such that the symmetries act in a simple way on the hybrid Wannier orbitals:

$$\begin{aligned} T_{L_1} |w(\pm, n, k_y)\rangle &= |w(\pm, n+1, k_y)\rangle \\ T_{L_2} |w(\pm, n, k_y)\rangle &= e^{i2\pi k_y} |w(\pm, n, k_y)\rangle \\ C_2\mathcal{T} |w(\pm, n, k_y)\rangle &= |w(\mp, -n, k_y)\rangle \\ C_{2x} |w(\pm, n, k_y)\rangle &= \mp i e^{-i2\pi k_y n} |w(\mp, n, -k_y)\rangle \end{aligned} \tag{2.6}$$

where the last equation holds only at C_{2x} symmetric flux values. The first two definitions are the consequence of Eq. (2.4), while the latter two come from demanding the following actions in momentum space:

$$\begin{aligned} C_2\mathcal{T}\hat{c}^\dagger_{\pm,\mathbf{k}}(C_2\mathcal{T})^{-1} &= \sigma^x K \hat{c}^\dagger_{\pm,\mathbf{k}}, \\ C_{2x}\hat{c}^\dagger_{\pm,k_x,k_y}(C_{2x})^{-1} &= \sigma^y \hat{c}^\dagger_{\pm,k_x,-k_y}, \end{aligned} \tag{2.7}$$

where σ^x acts on $\pm$ indices, and K is the complex conjugation operator. This, together with a continuity criterion such that the Wannier functions are smooth function of k_y, fixes the phase ambiguity up to an overall minus sign (App. A.2).[3]

Now that we have described the interacting Bistritzer-MacDonald model in detail, we proceed to discuss how we will solve for its ground state using DMRG.

2.3 MPO Compression and DMRG

In this section we consider the practical details of performing infinite DMRG on the IBM model defined in the last section, and the necessity of MPO compression.

To perform infinite DMRG, we must express the Hamiltonian (Eq. (2.1)) as an infinite 1D Matrix Product Operator (MPO) whose size D is called the bond dimension[4] [72]. To map from 2D to a 1D chain, we order the Wannier orbitals $|w(\pm, n, k_y)\rangle$ by the positions $P_x(\pm, k_y) + n$ of their Wannier centers. Translation along $\mathbf{L}_1$ simply increments $|w(\pm, n, k_y)\rangle \to |w(\pm, n+1, k_y)\rangle$, so the 1D chain is periodic with a unit cell of size $N_B N_y$ sites ($N_B = 8$ with spin and valley). Once the MPO is obtained, we can in principle find its ground state with DMRG.

However, the long-range nature of the Coulomb interaction complicates matters. Although the screened Coulomb interaction decays exponentially in real space, truncating it at

[3] In the absence of C_{2x} symmetry, we use a heuristic such that the gauge is continuous as a function of Φ_y.

[4] The MPO bond dimension is always denoted by D, and χ is reserved for the MPS bond dimension.

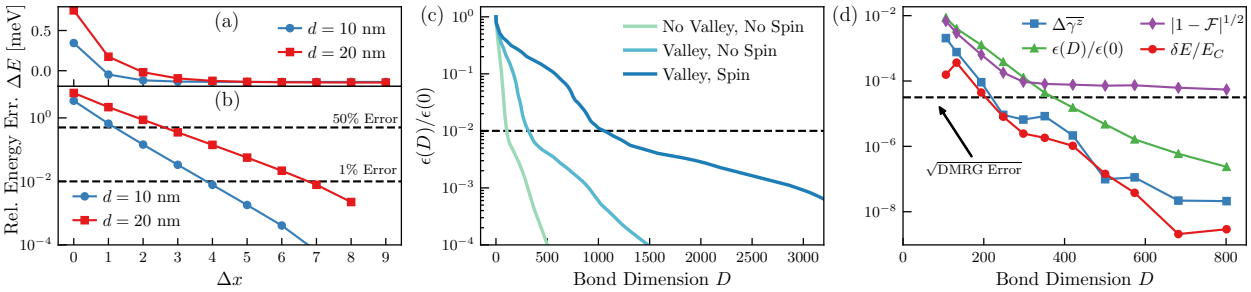

Figure 2.5: (a) Energy difference between the QAH and the SM ansatz at different gate distances at $w_0/w_1 \sim 0.8$. (b) The relative error in energy difference between the QAH and SM ansatz. The black dashed lines indicate 50% error and 1% error. (c) Precision of the compressed MPO as a function of bond dimension for the IBM model with and without spin and valley degrees of freedom. The Hamiltonian is the IBM model at the chiral limit $w_0 = 0$ with parameters given by Table 2.1. For (b), the cutoff range is reduced to $\Delta x = 3$. (d) Relative precision of MPO compression as a function of the post-compression bond dimension D. The precision is controlled by $\epsilon(D) = (\sum_{a=D+1} s_a^2)^{1/2}$, as described in Eq. (A.53). Here $\Delta E(D) = E(D = 1000) - E(D)$ is the energy error in the ground state, $\mathcal{F}$ is the fidelity per unit cell between the ground state at D and the ground state at $D = 1000$, and $\Delta\overline{\gamma^z}$ is the error in the polarization versus $D = 1000$, described in Sec. 2.4. One can see that the precision improves roughly in proportion to ϵ, except for $|1 - \mathcal{F}|^{1/2}$, which is limited by the precision of DMRG (black dashed line).

short range can lead to physically incorrect results. To demonstrate this, Fig. 2.5 (a) examines the energy of two ground state wavefunction ansätze "QAH" and "SM$_y$" as a function of the truncation distance of the interaction Δx [5] (these physical states are defined and used in Sec. 2.5 below). In particular, we examine the energy difference $\Delta E = E_{QAH} - E_{SM}$ in Panel (a), and the relative energy difference in Panel (b). The true energy difference between these states is $|\Delta E(\Delta x \to \infty)| \approx 0.1\,\text{meV}$, yet the energy difference achieves 0.1 meV precision only at $\Delta x \geq 3$. Going from $\Delta x = 1 \to 2$, for example, their energies change by almost 0.1 meV.

More importantly, the relative error in energy difference $(\Delta E(\Delta x) - \Delta E(\infty))/\Delta E(\infty)$ reaches 1% only at the cutoff $\Delta x \geq 4$. This means that in order to resolve closely competing ground state candidates — which we will encounter in practice in Section 2.2 below — we require a relatively large cutoff Δx.

Furthermore, the required cutoff is highly dependent on the model parameters. For example, if we increase the gate distance to 20 nm, then the screening distance is increased, and the relative energy gap does not achieve 50% precision until $\Delta x \approx 3$ (Fig. 2.5 (b)). [6] Together, these results suggest that premature truncation may lead to physically incorrect results, and we are forced to retain relatively long-range interactions in the Hamiltonian.

After mapping to a 1D chain, this means we must keep track of interactions up to range

[5] We define Δx as the distance between the first and last field operators along the cylinder

[6] Note, however, that larger *precompression* MPO bond dimension does not necessarily mean larger *postcompression* MPO bond dimension. The relationship between Hamiltonian parameters and the post-compression bond dimension is a subject of future work.

$R = N_B N_y \Delta x$ orbitals. An exact representation has an optimal bond dimension which scales as $D = O(R^2)$ (App. A.3). However, this still produces an MPO of size $D \sim 1 \times 10^4$ for $\Delta x \leq 4$ without spin and valley, and if we were to add in spin and valley it would be $D \sim 1 \times 10^5$. As the computational complexity of DMRG increases as $O(D^2)$, and D is usually a few hundred at most, the Hamiltonian for BLG is far too large for DMRG to be practical. The DMRG results of Ref. [38] considered a single spin and valley with interactions truncated at $\Delta x = 2$, resulting in an MPO of $D \sim 2000$ at $L_y = 6$. But increasing Δx, or adding spin and valley, makes the problem impractical.

On a finite system, the MPO can be viewed as a 2-sided MPS and compressed by SVD truncation (this approach is implemented in the `AutoMPO` feature of the `iTensor` library [73]). However, in the infinite limit we wish to take here, this naive SVD truncation is unstable and actually destroys the locality of the Hamiltonian. To avoid this, Ref. [61] developed a modification of SVD compression which guarantees that the compressed Hamiltonian remains Hermitian and local in the thermodynamic limit.

As in finite SVD compression, an intermediate step of the algorithm produces a singular value spectrum s_a, and the bond dimension can be reduced by discarding the lowest values of the spectrum. For an appropriate notion of distance this truncation is optimal, and when applied to a single cut, the discarded weight $\epsilon(D) = \sqrt{\sum_{i=D+1}^{D'} s_a^2}$ upper bounds the error in $\widehat{H}$ with respect to the Frobenius norm. In the Appendix A.4 we present efficient algorithms for finite-length unit cells and derive error bounds for various quantities. When exploiting quantum numbers, the algorithm is capable of compressing MPOs with bond dimensions 5×10^4 or larger on a cluster node.

With the bond dimension thus reduced to a reasonable value, we may perform DMRG. We use the standard `TeNPy` library [74], written by one of us, taking full advantage of symmetries. Careful checks guaranteeing the accuracy and precision of our code, benchmarks, and other numerical details are given in App. A.5.

Figure 2.5 showcases the precision of our DMRG results. We performed DMRG at the chiral limit $w_0 = 0$ and computed the relative error in the ground state energy, ground state fidelity, and expectation values as a function of post-compression bond dimension D, relative to $D = 1000$. The relative precision $\epsilon(D)/\epsilon(0)$ improves quickly with D, dipping below 10^{-6} by $D = 800$. In accordance with the error bound on H, the ground state energy, wavefunction, and expectation values converge quickly as $\epsilon \to 0$.

As a proof of principle, we also performed MPO compression for the IBM model with spin and valley at $L_y = 6$ and $w_0 = 0$. Due to constraints on the size of the uncompressed MPO we can handle, we chose a cutoff range of $\Delta x = 3$, which resulted in a $D \sim 35,000$ uncompressed MPO. The singular value spectrum of the MPO is shown in Fig. 2.5. If we define $\mathcal{F}$ as the fidelity per unit cell[7] between the ground state of the compressed MPO with bond dimension D and the ground state of the MPO with $D = 1000$, then we see from Fig. 2.5 that in the spinless, single-valley calculation, $\epsilon(D)/\epsilon(0)$ and $|1 - \mathcal{F}|^{1/2}$ have roughly the

[7]We define the fidelity per unit cell in the thermodynamic limit as $\mathcal{F} = \lim_{N\to\infty} |\langle \psi_{N,D} | \psi_{N,D=1000} \rangle|^{2/N}$, where N is the number of unit cells.

same order of magnitude. Using this fact as a guide, we can estimate the bond dimension where $|1-\mathcal{F}|^{1/2} \sim 10^{-2}$ by looking at the value of $\epsilon(D)/\epsilon(0)$. This gives us bond dimensions $D = \{106, 317, 1057\}$ for spinless/single-valley, spinless/valley, spin/valley MPO. While still relatively large, such bond dimensions are tractable with a standard workstation or cluster node when exploiting quantum numbers.

Of course the IBM model itself is only an approximation to the physical system, neglecting effects such as lattice relaxation, phonons and twist angle disorder which, though small, are expected to enter at the 1 meV level. This provides a limit on the amount of precision which is physically useful. To be safe, we choose $\Delta x = 10$, [8] $\epsilon = 10^{-2}$ meV, which results in post-compression bond dimensions of $D \approx 600 - 1000$, depending on the value of w_0/w_1. In conclusion, we have used MPO compression to reduce the Hamiltonian to a computational tractable size, incurring a precision error on the order of 10^{-2} meV — three orders of magnitude below the relevant energy scale of the problem. We now discuss the results of DMRG and the implications for the ground state physics of bilayer graphene.

2.4 Ground State Physics at Half Filling

In this section we report the results of our DMRG calculations and discuss the ground state physics of the (spinless, single valley) IBM model at half filling. We will show there is a clear transition from a quantum anomalous Hall state at small w_0/w_1 to a nematic semimetallic state at large w_0/w_1. Furthermore, we will show that these ground states are almost exactly described by the k-space Slater determinants predicted by Hartree-Fock.

Single particle projector and order parameter

We start by defining several crucial observables and order parameters. Because we find the DMRG ground state is translation invariant, all one-body expectation values can be obtained from the correlation matrix

$$P(\mathbf{k}) := \begin{pmatrix} \langle c^\dagger_{+,k_x,k_y} c_{+,k_x,k_y} \rangle & \langle c^\dagger_{-,k_x,k_y} c_{+,k_x,k_y} \rangle \\ \langle c^\dagger_{+,k_x,k_y} c_{-,k_x,k_y} \rangle & \langle c^\dagger_{-,k_x,k_y} c_{-,k_x,k_y} \rangle \end{pmatrix}. \tag{2.8}$$

This matrix is a projector when the expectation values are taken with respect to a Slater determinant, and it is the central variational object for k-space Hartree-Fock calculations. For DMRG in mixed-xk space, we calculate $P(\mathbf{k})$ by Fourier transforming two-point correlation functions. [9]

[8] This gives us an uncompressed bond dimension of order 5×10^4, close to what would be necessary for spinful/valleyful calculation.

[9] Explicitly, $P(\mathbf{k})$ is defined for $\mathbf{k}$ on a $108 \times L_y$ grid of $\mathbf{k}$ points in the mBZ by computing expectations $\langle c^\dagger_{\pm,0,k_y} c_{\pm,n,k_y} \rangle$ with respect to the DMRG ground state on the mixed-xk space cylinder for $-53 \leq n \leq 54$ and performing a discrete Fourier transform with respect to $\mathbf{L}_1$.

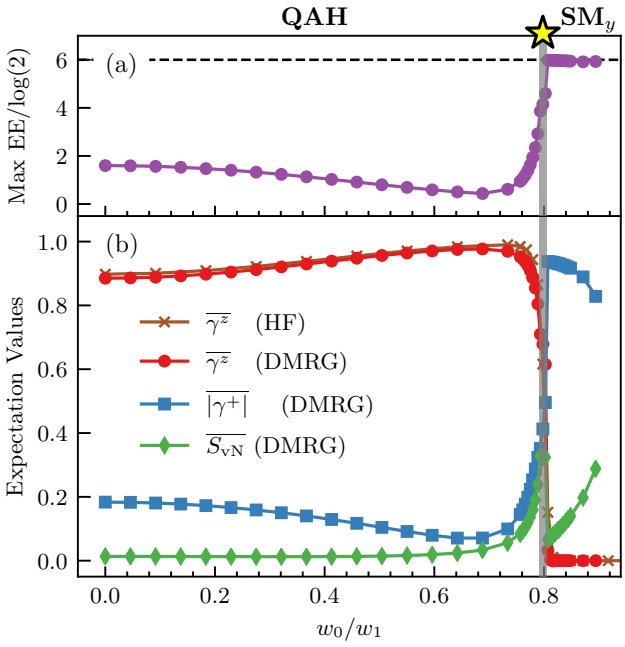

Figure 2.6: The phase diagram of the IBM at half filling as a function of w_0/w_1. There is a transition from a quantum anomalous hall (QAH) phase to a semimetallic (SM) phase at $w_0/w_1 = 0.798 \approx 0.8$, represented by a yellow star. (a) Entanglement entropy of the DMRG ground state with hybrid Wannier orbitals ordered according to their polarization, maximized over all 12 entanglement cuts dividing the system into left and right halves. (b) Expectation values of various observables (defined in the text) in the DMRG or Hartree-Fock(HF) ground states. The polarization in Chern band space $\overline{\gamma^z}$ is an order parameter for the transition. Its drop across the transition is accompanied by a commensurate increase in $\overline{|\gamma^+|}$, such that the DMRG ground state remains close to a Slater determinant. DMRG is performed at bond dimension $\chi = 1024$, $\epsilon_{\mathrm{MPO}} = 10^{-2}$ meV and is convergent away from the transition. (Gray shading indicates where DMRG is not well converged.).

The one-body observables are spanned by the expectation values of Pauli matrices σ in the $\pm$ band space,

$$\gamma^z(\mathbf{k}) := \mathrm{tr}[P(\mathbf{k})\sigma^z], \tag{2.9}$$

and similarly for $\gamma^x, \gamma^y, \gamma^+ = \gamma^x + i\gamma^y$. We denote mBZ averages by

$$\overline{\gamma^\alpha} := \frac{1}{A_{\mathrm{mBZ}}} \int_{\mathrm{mBZ}} d^2\mathbf{k}\, \gamma^\alpha(\mathbf{k}). \tag{2.10}$$

where A_{mBZ} is the area of the mBZ. We will focus particularly on $\overline{\gamma^z}$ — which is an order parameter for $C_2\mathcal{T}$ and C_{2x}, as follows from Eq. (2.6) which implies that $\gamma^z(\mathbf{k}) = 0$ for a $C_2\mathcal{T}$ symmetric state, and $\gamma^z(C_{2x}\mathbf{k}) = -\gamma^z(\mathbf{k})$ for a C_{2x} symmetric state.

In the case where the state is indeed a momentum-diagonal Slater determinant, $P(\mathbf{k})$ acquires several special properties. In particular, if a momentum mode $\mathbf{k}$ is occupied by one electron, $P(\mathbf{k})$ takes values on the unit sphere and can be parametrized in spherical

Parameter	Value(s)
θ_{BM}	$\sim 1.05°$
w_1	$\sim 109\,\text{meV}$
w_0/w_1	[0, 1]
Gate distance	10 nm
Relative permitivity	12
N_y	6
Φ_y	$\pi, \pi/10$
χ	≤ 1024
Δx	10
ϵ_{MPO}	$< 10^{-2}$ meV
Kinetic energy scale (t)	$< 1\,\text{meV}$
Interaction energy scale (V)	$< 10\,\text{meV}$

Table 2.1: Parameters of the IBM model, DMRG calculation, and relevant energy scales. See main text for the definition of each entry.

coordinates as

$$P(\mathbf{k}) = \frac{1}{2}(\sigma^0 + \cos\theta_{\mathbf{k}}\sigma^z + \sin\theta_{\mathbf{k}}\cos\varphi_{\mathbf{k}}\sigma^x + \sin\theta_{\mathbf{k}}\sin\varphi_{\mathbf{k}}\sigma^y) \tag{2.11}$$

which implies $|\gamma^+|^2 + |\gamma^z|^2 = 1$. If the projector respects $C_2\mathcal{T}$ and C_{2x} symmetries, then respectively $\theta_{\mathbf{k}} = \pi/2$ and $\varphi_{\mathbf{k}} = -\varphi_{C_{2x}\mathbf{k}} + \pi$ at all $\mathbf{k}$. Finally, since $P(\mathbf{k})$ is a projector for momentum-diagonal Slater determinants, it satisfies $S_{\text{vN}}(\mathbf{k}) := -\operatorname{Tr}[P(\mathbf{k})\log P(\mathbf{k})] = 0$. In general, then, $S_{\text{vN}}(\mathbf{k}) \geq 0$ measures the deviation of a state from a translationally-invariant Slater determinant.

iDMRG details and parameter choices

Infinite DMRG (iDMRG) calculations were performed using the open source `TeNPy` package [74]. The numerical parameters and physical energy scales of the problem are summarized in Table 2.1. In particular, we take $N_y = 6$ and $\Phi_y = \pi$ as the "default" values. The MPO bond dimension was compressed down to $600 - 1000$, such that the expected error is of order 10^{-2} meV, as described in Sec. 2.2. To ensure that iDMRG was converged, we varied the MPS bond dimension χ between 200 and 1024. We found that DMRG converged well even at very low bond dimensions, except near the transition. We also allowed ground states with broken translation invariance with a doubled unit cell, but we found a fully translation invariant ground state for all parameters we tested.

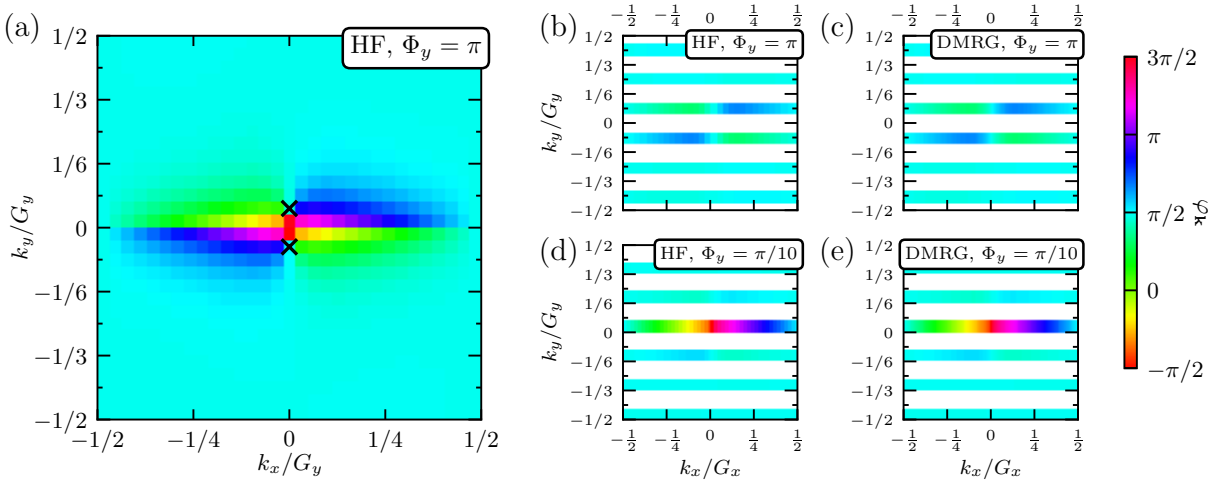

Figure 2.7: Comparison of HF and DMRG calculations of $\varphi_{\mathbf{k}} = \arg[\gamma^+(\mathbf{k})] \in [-\pi, \pi]$ over the mBZ at $w_0/w_1 = 0.85$. (a) HF on a 30×29 grid with $\Phi_y = \pi$. The crosses represent the approximate location of Dirac points. (b) HF on a 30×6 grid at $\Phi_y = \pi$. (c) DMRG correlation function on a 108×6 grid at $\Phi_y = \pi$. (d) HF on a 30×6 grid at $\Phi_y = \pi/10$. (e) DMRG correlation function on a 108×6 grid at $\Phi_y = \pi/10$. The horizontal bands in (b) – (d) are centered on the k_y cuts used, given by Eq. (2.3). One can see that the DMRG and HF calculations are virtually identical. DMRG are performed using $\chi = 1024$. The discontinuity at $k_y = 0^+$ is a gauge choice, described in 2.2.

Ground State Transition and the QAH phase

We performed iDMRG at 44 values of w_0/w_1 in the range $[0, 1]$. Fig. 2.6 (b) shows that the order parameter $\overline{\gamma^z}$ is non-zero for $w_0/w_1 \leq 0.8$, and vanishes for larger values of w_0/w_1, signaling a transition from a $C_2\mathcal{T}$ and C_{2x} broken phase to a $C_2\mathcal{T}$ and C_{2x} symmetric phase.

For low w_0/w_1, not only is $C_2\mathcal{T}$ broken, but the state is almost perfectly polarized, with $\overline{\gamma^z} \approx 1$. This implies that the state has a large overlap with the product state in which all "+" orbitals are occupied:

$$|\text{QAH}\rangle \approx \prod_{x,k_y} \hat{c}^\dagger_{+,x,k_y} |0\rangle \,. \tag{2.12}$$

Since the $\pm$ bands carry Chern number $C = \pm 1$, this state is a quantum anomalous hall (QAH) insulator [42, 55, 75]. This approximation is quite good: the QAH state is well described by a product state plus small corrections, $|\langle \Psi_0 | \Psi_{QAH} \rangle| \approx 0.846$ per unit cell at $w_0 = 0$. Consequently, the QAH state has low entanglement entropy (Fig. 2.6) and DMRG converges at quite moderate bond dimensions.

Above $w_0/w_1 \approx 0.8$, $\overline{\gamma^z} = 0$ and the state instead develops a large expectation value for $\gamma^+ = \gamma^x + i\gamma^y$. Section 2.5 below is devoted to the large w_0/w_1 phase, and we will see that it is a nematic semimetal [62], which we refer to as "SM$_y$", in reference to the ordering in the x/y plane. First, however, we analyze a surprising structure in the ground state correlations.

The remarkable accuracy of Hartree-Fock

The ground states of the strongly interacting IBM model are – quite surprisingly – very well described by k-space Slater determinants. For all values of w_0/w_1 away from the transition, the difference between the ground state and a Slater determinant as quantified by $S_{\mathrm{vN}}(\mathbf{k})$ is small. In particular, Fig. 2.6 shows that $\overline{S}_{\mathrm{vN}}$ is low in the QAH phase, increases or diverges near the transition, and is relatively small but growing in the SM_y phase. In the QAH phase this behavior is expected due to the large overlap with the simple Chern band polarized Slater determinant Eq. (2.12).

To provide further evidence that the ground state is essentially a Slater determinant, we compare DMRG results with Hartree-Fock (HF) calculations. Hartree-Fock determines an optimal Slater determinant approximation to the ground state of a many-body problem through a self consistent equation. Computationally, HF scales only polynomially in the number of k_y cuts (rather than exponentially for DMRG), so it provides a much cheaper alternative — when it is applicable. When the ground state of the IBM model is close to a Slater determinant, the HF ground state should be quite accurate and would have high overlap with the true ground state. We performed HF calculations on a $N_x \times N_y$ grid in the mBZ; numerical details of our HF calculations have been reported elsewhere [8].

We find that HF and DMRG results are nearly identical. The $C_2\mathcal{T}$ order parameter γ^z differs by around 2% (Fig. 2.6). Fig. 2.7 shows a side-by-side comparison of the DMRG and HF predictions for $\varphi_{\mathbf{k}} = \arg[\gamma^+(\mathbf{k})]$ in the SM_y phase, where it completely specifies the Slater determinant because $\theta \equiv \pi/2$ is fixed by $C_2\mathcal{T}$ symmetry (See Eq (2.11)). Panel (a) shows a high-resolution HF calculation with $N_x = 30, N_y = 29$, which shows that $\varphi_{\mathbf{k}} \approx \pi/2$ over most of the mBZ, but winds through 2π for k_y cuts that go near the Γ point. Panels (b) – (d) demonstrate that the same pattern appears with only $N_y = 6$ discrete momentum cuts. Both HF and DMRG produce a C_{2x} symmetric $\varphi_{\mathbf{k}}$ and the results obtained from both methods are almost indistinguishable. Other observables are similarly accurate in HF. We may therefore use HF to study large system sizes or observables that are not easily accessible in DMRG. For instance, Koopman's Theorem implies that the energies of single-fermion excited states are given by the self-consistent Hartree-Fock spectrum. We found the Hartree-Fock spectrum at the chiral limit has a gap of order 20 meV, showing the QAH state is gapped. We conclude that DMRG and HF agree to a remarkable degree and may be used almost interchangeably in this regime.

2.5 The Nematic Semimetal

We now show that the large-w_0/w_1 phase is a nematic semimetal, first described in Ref. [62], with energetics governed by the Berry curvature of the flat bands. This is an altogether different state than the Dirac semimetal which appears in the non-interacting BM model. Our analysis is based on combination of DMRG (at $L_y = 6$) and HF (at $L_y \sim 30$), which agree wherever they can be compared. After establishing the nature of the nematic semimetal,

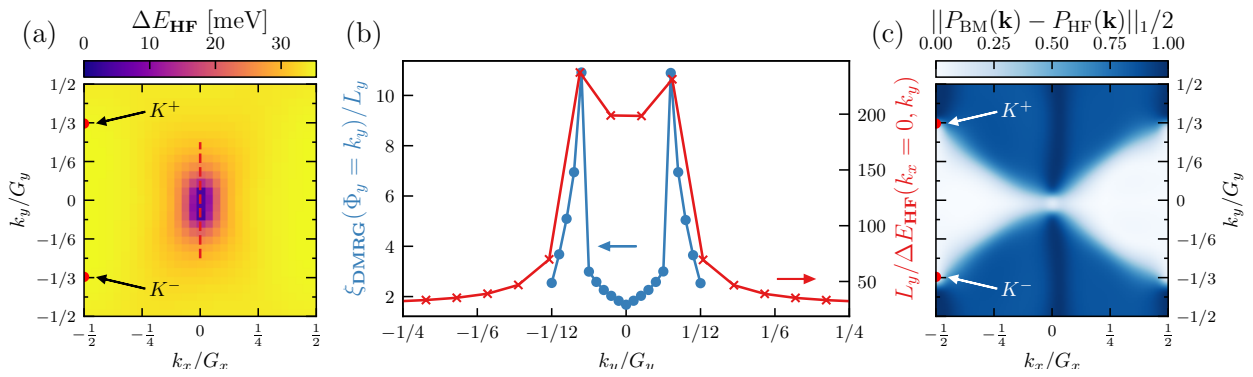

Figure 2.8: Result of HF calculation at $N_x \times N_y = 30 \times 29$. (a) Energy gap between the top band and the bottom band. We see there are two Dirac points near the gamma point. (b) Correlation length obtained from thin cylinder DMRG at different flux values and the inverse HF gap size as a function of k_y. We see the correlation length becomes large near the Dirac points found in HF calculation. (c) The trace distance between the density matrices for the BM ground state and Hartree-Fock ground state. One can see that they are unrelated over much of the mBZ.

we make contact with recent ideas in the literature [38, 55, 62]. Namely, we explain how the Ginzburg-Landau-like functional for the interband coherence φ proposed in Ref. [62] provides an intuitive description of the nematic state and the transition, and also confirm that the stripe state proposed in Ref. [38] is extremely competitive, with an energy only 0.2 meV / electron above the DMRG ground state.

The Large w_0/w_1 Phase is Nematic

The large w_0/w_1 phase is a nematic state which breaks C_3 but preserves $C_2\mathcal{T}$. $C_2\mathcal{T}$ requires $\gamma^z = 0$, but allows for finite $\gamma^{x/y}$, so within the spherical coordinate description of Eq. (2.11) the state is characterized by $\theta = \pi/2$ and an azimuthal angle $\varphi_{\mathbf{k}}$. This is clearly visible in Fig. 2.7 (a): throughout *most* of the mBZ, including at the mini-$K^{\pm}$ points, the state is $\gamma^y \approx 1$ ($\varphi \sim \pi/2$). A state with finite $\gamma^x + i\gamma^y$ at the $K^{\pm}$ points breaks C_3 symmetry (nematicity) because C_3 acts as $C_3 = e^{i\pi\sigma^z/3}$ there. This is in contrast to the BM ground state, which has Dirac nodes at $K^{\pm}$: the BM Dirac structure $h(K^{\pm} + \mathbf{q}) \propto q_x\sigma_x + q_y\sigma_y$ instead causes $\gamma^x + i\gamma^y$ to wind by $+2\pi$.

Consequently we denote the large w_0/w_1 state "SM$_y$." Presumably the other C_3-rotated versions are not found because the cylinder geometry weakly breaks the C_3 symmetry for finite N_y.

While the SM$_y$ phase is close to a Slater determinant, it is not a small perturbation to the non-interacting ground state. To quantify this, Fig. 2.8(c) shows the trace distance between the BM ground state projector and the SM$_y$ projector over the mBZ. Around the $K^{\pm}$ points, the trace distance rotates between complete agreement and orthogonality, consistent with the winding of γ^+ in the BM state versus the fixed $\gamma^y \approx 1$ in SM$_y$. The trace distance also

provides us with a gauge invariant way to identify the nematicity of the phase: the BM and SM_y projectors achieve near complete agreement along the y-axis.

$C_2\mathcal{T}$ protected Dirac points

Near the Γ point, however $\varphi_{\mathbf{k}}$ deviates from $\varphi = \pi/2$. We now show that this is because the SM_y phase features two Dirac points in the vicinity of Γ, which cause $\varphi_{\mathbf{k}}$ to wind there. This behaviour is in fact enforced by topological properties [44, 55]. For a generic two band problem in the presence of $C_2\mathcal{T}$, any Wilson loop is quantized: $W(C) := i\int_C \mathbf{A}\cdot d\mathbf{k} = n\pi$ with $n \in \mathbb{Z}$ [76].[10] In particular, $W(C) = (2n+1)\pi$ if and only if it encloses a Dirac cone.

This is the well-known topological protection of Dirac cones. In the case of the single valley BM model, Dirac cones at the mini $K^{\pm}$ points have the *same* chirality $W(C) = +\pi$. Therefore, not only are the Dirac cones locally protected, but even if they move away from $K^{\pm}$ they cannot meet and annihilate, enforcing the existence of either a pair of Dirac points or quadratic band touching.[11]

The semimetallic nature of SM_y is borne out in both HF and DMRG numerics. The spectrum of the self-consistent HF Hamiltonian, shown in Fig. 2.8 (a), has a large ($\Delta \approx 30\,\mathrm{meV}$) gap across most of the mBZ, except near the Γ point. The structure of Δ near the Γ point is consistent with two Dirac points at $\mathbf{k}_{\pm} := (k_x, k_y) \approx (0, \pm 0.05 G_y)$ (Fig. 2.8(b)). In contrast, the BM model is gapless at the $K^{\pm}$ points, but gapped near Γ.

DMRG numerics can also detect these nodes, but special care is required. This is because the allowed momentum cuts, Eq. (2.3), generically avoid $\mathbf{k}_{\pm}$. To confirm their existence, we continuously adjust the flux Φ_y through the cylinder (see Fig. 2.2 (e)) and monitor the behavior of the DMRG ground state as the allowed momenta pass through the putative Dirac points. Fig. 2.8(b) shows that the DMRG correlation length appears to diverge right as the allowed momenta pass through the location of the Dirac points $\mathbf{k}^{\pm}$ found in HF, consistent with the gap closing.

We conclude that the large w_0/w_1 phase is a nematic semimetal: SM_y preserves $C_2\mathcal{T}$, breaks C_3, and has two Dirac nodes on the y axis near Γ.

Ginzburg-Landau-like Description of the SM_y Phase

There is a very appealing Hartree-Fock picture for why the Coulomb interactions reconstruct the single particle Dirac semimetal into the nematic SM_y semimetal. When $C_2\mathcal{T}$ is preserved, the state is specified entirely by the phase of the inter-band coherence $\varphi_{\mathbf{k}}$, so the HF energy is a functional $E_{\mathrm{HF}}[\varphi_{\mathbf{k}}]$. Ref. [62] analytically computed this functional for the IBM model,

[10] The Berry phase is computed for the filled band only.

[11] Note however that this "global" protection implicitly assumes translation symmetry: if the unit cell doubles, the bands fold and the band count doubles. Beyond two bands, $W(C)$ is only defined modulo π, so Dirac points can meet and annihilate. This mechanism underlies the $C_2\mathcal{T}$ stripe phase[38].

Eq. (2.1), and found that the dominant contribution takes the form

$$E_{\mathrm{HF}}[\varphi_{\mathbf{k}}] = E_{\mathrm{HF}}^{\mathrm{QAH}} + \frac{1}{2}\int g_{\mathbf{k}}(\nabla_{\mathbf{k}}\varphi_{\mathbf{k}} - 2\mathbf{a}_{\mathbf{k}})^2 d^2\mathbf{k} + \cdots$$
$$g_{\mathbf{k}} = \frac{1}{A}\sum_{\mathbf{q}} V_{\mathbf{q}}\,\mathbf{q}^2 |\Lambda_{\mathbf{q}}(\mathbf{k})|^2 \tag{2.13}$$

Here $g_{\mathbf{k}}$ is a E_C-scale function independent of $\varphi_{\mathbf{k}}$, and $E_{\mathrm{HF}}^{\mathrm{QAH}}$ is the Coulomb energy of the QAH state. Finally, $\mathbf{a}_{\mathbf{k}}$ is a U(1) vector potential which encodes the band geometry: due to the $C_2\mathcal{T} = \sigma^x K$ symmetry, the SU(2) Berry connection of the Bloch states is constrained to take the diagonal form $\mathbf{A}(\mathbf{k}) = \sigma^z \mathbf{a}_{\mathbf{k}}$, reducing it to a $U(1)$ connection. [12]

We see that the energy is similar to the Ginzburg-Landau functional for a superconductor in a magnetic field $F_{\mathbf{k}} = \mathrm{d}\mathbf{a}_{\mathbf{k}}$. This isn't a coincidence: $\nabla_{\mathbf{k}}\varphi_{\mathbf{k}}$ can only appear via a gauge-covariant derivative because $\varphi_{\mathbf{k}}, \mathbf{a}_{\mathbf{k}}$ transform as a gauge pair under a $C_2\mathcal{T}$-preserving phase redefinition of the Bloch states, $\hat{c}_{\pm,\mathbf{k}} \to e^{\pm i\phi_{\mathbf{k}}}\hat{c}_{\pm,\mathbf{k}}$. However, there is no exact U(1) symmetry, so the small "$\cdots$" terms we neglect (for example the dispersion h) do couple directly to φ.

The superconducting analogy can be made more concrete by applying a particle-hole transformation to only the $C = -1$ band, so that the coherence φ between $C = \pm 1$ bands maps to "superconducting pairing" between two $C = 1$ bands [55]. The Berry curvature $F_{\mathbf{k}}$ then appears with the same form as a magnetic field, albeit in k-space, similar to how Berry curvature manifests as a "k-space magnetic field" in the semiclassical equations of motion for Bloch electrons [77].

If we treat the mBZ as the unit cell, the Chern number $\frac{1}{2\pi}\int F_{\mathbf{k}}\, d^2\mathbf{k} = 1$ implies that there is one flux quantum per unit cell. Just like the vortex lattice of a superconductor in a magnetic field $F_{\mathbf{k}}$, this forces φ to have two vortices per unit cell. Each vortex ($+2\pi$ winding) is equivalent to a Dirac point, so this recovers the topological protection of the Dirac points discussed earlier. In the BM ground state, the two vortices are pinned to the $K^{\pm}$ points, while in the SM_y state they lie near Γ (Fig. 2.7 (a)).

The vortices lead to an energy penalty relative to the QAH state, explaining Eq. (2.13). However, in our case the Berry curvature $F_{\mathbf{k}}$ is not uniform: instead, $F_{\mathbf{k}}$ is concentrated near the Γ point (Fig. 2.9(a)). By analogy to a superconductor in a non-uniform field, the lowest energy configuration of Eq. (2.13) will place the vortices in the region of concentrated $F_{\mathbf{k}}$, explaining their shift from $K^{\pm} \to \Gamma$. In Fig. 2.9(b), we confirm that $\nabla_{\mathbf{k}}\varphi_{\mathbf{k}} - 2\mathbf{a}_{\mathbf{k}} \approx 0$ in the region where $F_{\mathbf{k}}$ is small, but is finite near Γ where $F_{\mathbf{k}}$ is concentrated. Accordingly, most of the energy penalty comes from near the Γ point. Increasing w_0/w_1 makes $F_{\mathbf{k}}$ increasingly concentrated, reducing the Coulomb penalty of SM_y relative to QAH.

The final ingredient driving the finite w_0/w_1 transition are the small terms like the dispersion h hidden in "$\cdots$", which slightly prefer the SM_y phase.[13] As w_0/w_1 increases, the

[12] Note that $\mathbf{a}_{\mathbf{k}}$ here does not have a quantized Wilson loop, unlike $\mathbf{A}_{\mathbf{k}}$ discussed in Sec. 2.5. This is because $\mathbf{a}_{\mathbf{k}}$ is defined in terms of Chern bands, which are not invariant under $C_2\mathcal{T}$.

[13] For example, in the SM_y phase, $\varphi_{\mathbf{k}}$ can perturbatively deform to follow the dispersion h, particularly in the vicinity of Γ.

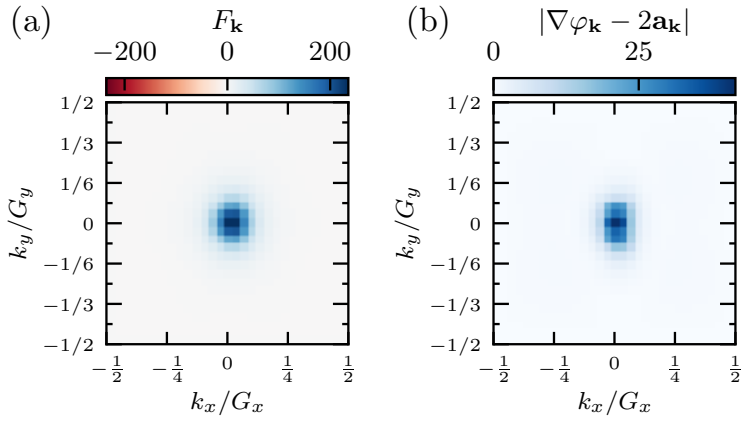

Figure 2.9: (a) The Berry curvature $F_{\mathbf{k}}$ for $w_0/w_1 = 0.85$ shows concentration at the Γ-point. (b) The k-space "supercurrent" $|\nabla\varphi_{\mathbf{k}} - 2\mathbf{a}_{\mathbf{k}}|$ is concentrated in the same region as $F_{\mathbf{k}}$. Both (a) and (b) are calculated in the units $G_x = G_y = 1$, $A_{BZ} = 1$.

Coulomb penalty for the SM_y phase decreases due to the Berry curvature concentration, and these subleading terms win out. Consequently, while increasing w_0/w_1 does slightly increase the bandwidth, its primary effect is actually via the redistribution of Berry curvature, which enters at the Coulomb scale ($g_{\mathbf{k}} \sim E_C$).

"Thin cylinder" DMRG Analysis

The DMRG ground state at $N_y = 6$ can be approximated by a particularly simple "thin cylinder" ansatz, provided none of the momentum cuts cross the region of large Berry curvature near Γ. We ensure this by taking $\Phi_y = \pi$ and focus on $w_0/w_1 \approx 0.85$. In this case, the DMRG ground state has a relatively small particle number fluctuation in the unit cell. This is because away from Γ, $P(\mathbf{k})$ varies slowly with k_x, so in the xk-space the correlations are local (intra-unit cell).

Table 2.2 shows the probability for each momentum mode in the unit cell to be occupied by 0, 1, or 2 electrons. All modes have $p(N_{k_y} = 1)$ larger than 0.9, and many of them larger than 0.95. This suggests there is a simple "thin-cylinder" ansatz with no particle number fluctuation per momentum mode: following Ref. [38], we define

$$|\Psi_{\mathrm{TC}}\rangle = \prod_{x,k} \left(\cos\frac{\theta(x,k_y)}{2} \hat{c}^\dagger_{+,x,k_y} + \sin\frac{\theta(x,k_y)}{2} e^{i\varphi(x,k_y)} \hat{c}^\dagger_{-,x,k_y} \right) |0\rangle \,. \tag{2.14}$$

It is easy to check that if θ and φ are independent of x, these θ and φ corresponds to those in Eq. (2.11). By inspecting Fig. 2.7 (b), we find $\theta = \pi/2$ and $\varphi = \pi/2$ is a good

k_y	$-\frac{5}{12}$	$-\frac{1}{4}$	$-\frac{1}{12}$	$\frac{1}{12}$	$\frac{1}{4}$	$\frac{5}{12}$
$p(N_{k_y}=0)$	0.021	0.021	0.049	0.049	0.021	0.021
$p(N_{k_y}=1)$	0.958	0.959	0.902	0.902	0.959	0.958
$p(N_{k_y}=2)$	0.021	0.021	0.049	0.049	0.021	0.021

Table 2.2: Probability that some states are occupied by 0, 1, or 2 electrons in a given unit cell at $w_0/w_1 = 0.85$, $\Phi_y = \pi$, and $\chi = 1024$. N_{k_y} is the number of electrons with momentum k_y in the unit cell.

approximation for the SM_y state[14] so long as the momentum cuts are not close to $k_y = 0$. The fidelity per unit cell of the resulting ansatz $|\Psi_{\mathrm{SM}}\rangle$ and the DMRG ground state is $\mathcal{F} \sim 0.98$ — remarkably accurate for such a simple ansatz. This ansatz also captures well the behavior of entanglement entropy in Fig. 2.6: each momentum mode contributes a "Bell pair" to entanglement, making the maximum entanglement $6 \log 2$ with our choice of orbital ordering.

We can further motivate the thin-cylinder ansatz from the value of the polarization $P_x(\pm, k_y)$. (Fig. 2.4). At large w_0/w_1, P_x is close to 0 for most k_y values, and orbitals in one unit cell are well separated from those in neighboring unit cells. The interaction therefore strongly couples modes within the same unit cell, resulting in vanishing number fluctuation per unit cell.

We also see why the thin-cylinder ansatz breaks down near the Γ point: $P(\mathbf{k})$ changes rapidly there (Fig. 2.7 (e)), leading to inter-unit cell correlations. We stress that the ansatz is thus a crude approximation to the true HF ground state, since it fails to capture the complex Berry curvature contribution to the energy that is dominant near the Γ point. As $N_y \to \infty$, the momentum cuts unavoidably approach Γ, and the thin-cylinder ansatz will break down.

Finally, we comment on the energy competition between different candidate ground states. The simple form of the ansatz enabled Kang and Vafek [38] to put forward another candidate for the ground state, which breaks translation symmetry in the $\mathbf{L}_1$ direction in favor of a period-2 stripe state with screw symmetry $C_{2x}T_{L_1}$. To crude approximation, this state corresponds to $\theta(n, k_y) = \pi/2$ and $\varphi(n, k_y) = (-1)^n \pi/2 + \pi/2$ in the parametrization of Eq. (2.14). In order to test this ansatz, we computed the energy of the SM ansatz and the stripe ansatz and compared it to the DMRG ground state energy (Table 2.3) and the QAH ansatz ($\theta = 0$). We also computed the energy of the ground state of the BM model with respect to the IBM model to establish the relevant Coulomb energy scale. We find that the energy of the QAH, SM_y, and the stripe ansatz are within 1/3 meV of the DMRG energy. While the stripe is not the true ground state for the parameter values studied here,[15] this

[14] Taking our different gauge convention into account, this is in agreement with [38].

[15] We verify this by initializing the DMRG using the doubled unit cell stripe ansatz, and find the stripe reverts to the SM_y phase at convergence.

State	Energy [meV]
DMRG Ground State (SM_y)	-28.24
QAH Ansatz (Eq. 2.14)	-28.04
SM_y Ansatz (Eq. 2.14)	-27.92
$C_2\mathcal{T}$ - Stripe Ansatz (Eq. 2.14)	-28.08
Dirac (BM Ground State)	-20.62

Table 2.3: Energy per electron of various trial states, evaluated with respect to the IBM Hamiltonian at $w0/w_1 = 0.85$. Here "Dirac" refers to ground state of the single-particle BM Hamiltonian, and the parameters for SM and Stripe Ansätze are described in the text. We see that the Stripe is very close to the DMRG ground state, and the Dirac state is well-separated from the rest, reflecting the dominant importance of the Coulomb interactions. Note that the energies are negative because we have subtracted off the $q = 0$ part of the Coulomb interaction.

confirms the assertion in Ref. [38] that the stripe is a viable candidate in the wider phase diagram.

2.6 Conclusions

In this chapter we have introduced a method for studying tBLG (and any other moiré material) using DMRG. Our method (Fig. 2.1) starts with the BM model, adds interactions, and compresses the resulting MPO down to a reasonable size so that the DMRG is computationally tractable. We carefully verified the correctness of our approach and showed that it is sufficiently precise to capture the ground state physics of the IBM model. To benchmark our approach we focused mostly on the spinless, single-valley case. However, we showed in Section 2.3 that our method can be extended to the spinful, two-valley case with only moderately greater computational resources. Therefore we have identified a method to study the ground state physics of tBLG using DMRG.

Even though the spinless, single-valley model is not strictly physical, our results have several important conceptual implications for the study of tBLG. Remarkably, we found that the DMRG ground state is well-approximated as a k-space Slater determinant for all w_0/w_1. However, we stress that the ground state nevertheless has *no* relation to the ground state of the single-particle BM model: it mixes states very far from the Fermi surface of the BM Hamiltonian (Fig. 2.8 (c)). At least near the magic angle this suggests that weak-coupling approaches to tBLG, which rely on various details of the BM Fermi surface, will miss the essential physics. Instead, the energetics are dominated by the exchange physics of the Coulomb interaction. As a result, the effective band structure (as would be computed from the self-consistent Hartree-Fock Hamiltonian) is entirely different than that of the BM model, with a width set by E_C (Fig. 2.8(a)). This is true even in the large w_0/w_1 nematic semimetal phase SM_y, which may have some relation to the $\nu = 0$ semimetallic resistance

peak found in experiment.

Furthermore, it is subtle to describe the observed ground states within a 2D Wannier-localized "Mott insulating" picture. For small w_0/w_1 we have a QAH phase: the filled states have net Chern number, so the projector onto the filled states cannot be 2D Wannier localized. This is not to say that it is impossible to find these states within a numerical approach which starts from 2D Wannier orbitals (which is just a change of basis), but rather that in such a basis the order would manifest as a set of coherences $\langle c_i^\dagger c_j \rangle$ between sites rather than an onsite order parameter. Presumably this would complicate any mean-field approach which depends on a site-local self energy.

Taken together, this supports the point of view that tBLG is more closely related to quantum Hall ferromagnetism, where symmetry breaking is driven by the combination of band topology and Coulomb exchange, than it is to the Mott insulating physics of the Hubbard model. But of course in contrast to quantum Hall systems, tBLG comes with time-reversal symmetry, making it amenable to superconductivity. Future work will explore the physics of tBLG upon restoring the spin and valley degrees of freedom.

Chapter 3

Effect of strain on twisted bilayer graphene

3.1 Introduction

In this chapter, we will focus on the role strain plays on the phase diagram of MATBG. Experiments on different twisted bilayer graphene (TBG) devices, all close to the first magic angle, have produced a broad variety of different low-temperature phase diagrams. For example, at the charge neutrality point (CNP), both semi-metallic [1–3, 30, 31, 78] and insulating [20, 21, 27, 34, 36] states have been observed. The insulating devices are thought to be divided into two groups. In the first group [20, 21], one of the graphene sheets is almost perfectly aligned with the hexagonal Boron-Nitride (hBN) substrate, which breaks the two-fold rotation symmetry and therefore generates mass terms for the Dirac cones [79–84] in the single-particle continuum model of TBG [4, 85, 86]. In the second group of devices [27, 34], those without substrate alignment, the Coulomb interaction is believed to be responsible for the insulating behavior. Both analytical and numerical studies [8, 42] of pristine TBG at the CNP indeed find an insulating ground state, due to spontaneous "Kramers inter-valley coherent" (KIVC) order [8]. The KIVC state is thus a promising candidate for the CNP insulators in Ref. [34], as well as the $|\nu| = 2$ insulators in general, but cannot explain the semimetals observed in Refs. [1, 3, 30, 31, 78]. Moreover, self-consistent Hartree-Fock (SCHF) predicts a KIVC gap of $\sim 20\,\text{meV}$ [8], while experiments measure a global transport gap of only $\sim 1\,\text{meV}$ [34].

An important question is thus: what weakens the insulators in some experimental devices, and destroys them in others? Twist-angle disorder is expected to be at least partly responsible for this [24, 87–89]. Another possible culprit is the presence of strain in the graphene sheets. Uniaxial heterostrain is characterized by a parameter ϵ, which scanning tunneling spectroscopy experiments have found to be in the range $\epsilon = 0.1 - 0.7\%$ [18, 32, 35]. Although these values seem small at face value, strain contributes to the Hamiltonian as a perturbation of order $\epsilon\hbar v_F/a$, which is ~ 20 meV for $\epsilon = 0.5\%$ — precisely the energy scale

at issue. Further evidence for the importance of strain comes from symmetry considerations. In the absence of strain, models at even integer filling show that although the ground state has KIVC order, there is a close competitor whose energy is only slightly higher: a nematic semi-metal [8, 15, 18, 38, 62]. As elucidated in Ref. [62], the semi-metal has two Dirac points close to, but not at, the mini-BZ Γ point, spontaneously breaking the three-fold rotational symmetry C_{3z}. The shear part of uniaxial strain breaks the C_{3z} symmetry, and thus one expects on general grounds that strain will lower the energy of the nematic semi-metal relative to the rotationally invariant insulating states. However, despite this expectation, Refs. [8, 62] found that if strain is modeled using the phenomenological method of Ref. [90], it cannot stabilize the semi-metal.

This chapter provides a careful treatment of the effects of strain on the correlated insulators using a more realistic model for strained TBG [91]. We find that physical strain values can drive a zero-temperature phase transition from the KIVC insulator to a semi-metal at even integer fillings. Our results at charge neutrality are obtained using SCHF, and our results at $\nu = -2$ (ν is the number of electrons per moiré unit cell relative to charge neutrality) using both density-matrix renormalization group (DMRG) and SCHF. Our DMRG considers both valley degrees of freedom, which is essential for correctly identifying the even-integer insulators. Similar to earlier works on single-valley models [15, 38], we find that DMRG and SCHF agree remarkably well. In particular, DMRG confirms the presence of KIVC order at $\nu = -2$ in the absence of strain.

3.2 Continuum model with strain

To add uniaxial strain to the Bistritzer-MacDonald (BM) continuum Hamiltonian [4, 85, 86], we follow Ref. [91]. Uniaxial strain is characterized by the following symmetric matrix:

$$\mathsf{S} = \begin{pmatrix} \epsilon_{xx} & \epsilon_{xy} \\ \epsilon_{xy} & \epsilon_{yy} \end{pmatrix} = \mathsf{R}(\varphi)^T \begin{pmatrix} \epsilon & \\ & -\nu_P \epsilon \end{pmatrix} \mathsf{R}(\varphi)\,, \tag{3.1}$$

where $\nu_P \approx 0.16$ is the Poisson ratio of graphene. The angle φ corresponds to the uniaxial strain direction, and $\mathsf{R}(\varphi)$ is a 2×2 rotation matrix. Throughout this chapter we take $\varphi = 0$, but we have verified that our conclusions do not depend on the choice of φ. The strain magnitude is determined by the dimensionless parameter ϵ, which in the devices prepared for STM study has values in the range $\epsilon = 0.1 - 0.7\%$ [18, 32, 35, 92]. Under the combined effect of rotation and strain, the coordinates of the carbon atoms in the two graphene layers $\ell = \pm$ of TBG transform as $\mathbf{R}_{\ell,i} \to \left[\mathsf{R}(\ell\theta/2) - \frac{\ell}{2}\mathsf{S}\right]\mathbf{R}_{\ell,i} =: \mathsf{M}_\ell^T \mathbf{R}_{\ell,i}$ where θ is the twist angle. The coordinate transformation matrix M_ℓ^T is correct to first order in both θ and ϵ. Note that we only consider heterostrain, as it affects the electronic structure much more strongly than homostrain [93].

The continuum Hamiltonian in the presence of uniaxial heterostrain for the $\tau = +$ valley is given by

$$H_{\tau+} = \begin{pmatrix} D_+ & T(\mathbf{r}) \\ T(\mathbf{r})^\dagger & D_- \end{pmatrix}\,, \tag{3.2}$$

with D_ℓ the monolayer Dirac Hamiltonians, and $T(\mathbf{r})$ the inter-layer tunneling ($H_{\tau-}$ is then fully specified by time-reversal). The Dirac Hamiltonians are given by

$$D_\ell = -\hbar v_F \left[\mathsf{M}_\ell(-i\boldsymbol{\nabla} + \mathbf{A}_\ell) - \mathbf{K}\right] \cdot \boldsymbol{\sigma}\,, \tag{3.3}$$

where $\boldsymbol{\sigma} = (\sigma_x, \sigma_y)$ are Pauli matrices acting in sublattice space, and $\mathbf{K} = (4\pi/3a, 0)$, with a the graphene lattice constant, corresponds to location of the $\tau = +$ valley. Strain shifts the locations of the Dirac points via a 'vector potential' $\mathbf{A}_\ell = -\frac{\ell}{2}\frac{\beta\sqrt{3}}{2a}\left(\epsilon_{xx} - \epsilon_{yy}, -2\epsilon_{xy}\right)$ [94, 95], where $\beta \sim 3.14$ characterizes the dependence of the tight-binding hopping strength on the bond length.

The tunneling term $T(\mathbf{r})$ in Eq. (3.2) has the same form as in the original BM model, but we update the microscopic parmaeters to follow recent density functional theory calculations [39, 40, 52]. Specifically, we take differing intra and inter-sublattice interlayer tunneling amplitudes $w_{AA} = 83\,\text{meV}$ and $w_{AB} = 110\,\text{meV}$. To account for non-zero strain ϵ, the moiré reciprocal lattice vectors are deformed to $\mathbf{g}_j = \left[\mathsf{M}_+^{-1} - \mathsf{M}_-^{-1}\right]\mathbf{G}_j$, where $\mathbf{G}_j$ are the reciprocal vectors of undeformed graphene.

As was shown in Ref. [91, 93], uniaxial heterostrain has three important effects on the BM band spectrum: (i) while strain preserves $C_2\mathcal{T}$ symmetry, and hence the stability of the two mini Dirac points, the three-fold rotation symmetry is broken and the two Dirac points move away from the $K^\pm$-points towards the Γ-point in the mBZ, (ii) the two Dirac points are no longer degenerate, but are separated in energy by a few meV (thus creating small electron and hole pockets at the CNP), and (iii) the bandwidth of the 'narrow' bands increases significantly – for ϵ as small as 0.6%, the bandwidth of the narrow bands is ~ 50 meV. Below, we investigate the effect of strain on the interacting phase diagram of TBG.

3.3 Hartree-Fock at neutrality

We model interacting TBG as the BM Hamiltonian plus Coulomb interactions:

$$H = \sum_{\mathbf{k}} f_{\mathbf{k}}^\dagger h(\mathbf{k}) f_{\mathbf{k}} + \frac{1}{2A}\sum_{\mathbf{q}} V_{\mathbf{q}} : \rho_{\mathbf{q}}\rho_{-\mathbf{q}} :\,, \tag{3.4}$$

where A is the area of the sample, and $f_{\mathbf{k},s,\tau,m}^\dagger$ creates an electron with momentum $\mathbf{k}$ and spin s in the BM band m in valley τ. The charge density operators are given by $\rho_{\mathbf{q}} = \sum_{\mathbf{k}} f_{\mathbf{k}}^\dagger \Lambda_{\mathbf{q}}(\mathbf{k}) f_{\mathbf{k}+\mathbf{q}}$, where the form factor matrices $[\Lambda_{\mathbf{q}}(\mathbf{k})]_{(\tau,m),(\tau',n)} = \delta_{\tau,\tau'}\langle u_{\tau,m,\mathbf{k}}|u_{\tau,n,\mathbf{k}+\mathbf{q}}\rangle$ are defined in terms of overlaps between the periodic part of the Bloch states of the BM Hamiltonian. The interaction is given by a gate screened Coulomb potential $V_{\mathbf{q}} = \int \mathrm{d}\mathbf{r}\, e^{i\mathbf{q}\cdot\mathbf{r}} V(\mathbf{r}) = \tanh(d_s q)[2\varepsilon_0\varepsilon_r q]^{-1}$. We work with a gate distance of $d_s = 25\,\text{nm}$, and we let the dielectric constant ε_r vary between 6 and 12. In Eq. (3.4) we also project into a subspace where most or all of the remote BM valence (conduction) bands are completely filled (empty), and m, n run over only those bands whose filling is not fixed. The single-particle Hamiltonian

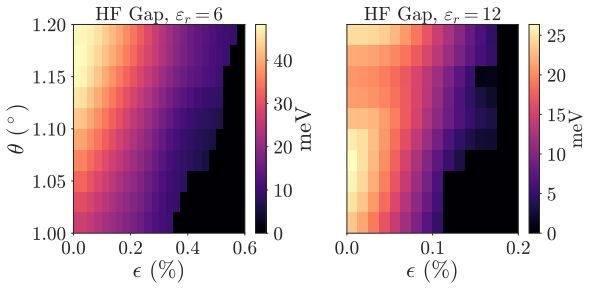

Figure 3.1: Particle-hole gap in the SCHF band spectrum at the CNP as a function of both twist angle θ and strain ϵ, for $\varepsilon_r = 6$ (left) and $\varepsilon_r = 12$ (right). The results were obtained on a 18×18 momentum grid, keeping six bands per spin and valley. The gapped regions have KIVC order, the gapless regions correspond to a symmetric SM.

$h(\mathbf{k})$ contains the BM band energies, a HF contribution from the remote filled bands, and a subtraction term [42, 62]. For more details on the definition of $h(\mathbf{k})$, see Ref. [15].

Without strain, Ref. [8] found that the ground state of H at $\nu = -2, 0, 2$ has a charge gap and spontaneously breaks both the valley charge symmetry $e^{i\alpha\tau_z}$, and the time-reversal symmetry $\mathcal{T} = \tau_x K$, where K denotes complex conjugation. However, the product $\mathcal{T}' = e^{i\pi\tau_z/2}\mathcal{T}$ is preserved. Because $\mathcal{T}' = \tau_y K$ is a (spinless) Kramers time-reversal, the insulating ground state was dubbed the Kramers inter-valley coherent (KIVC) state [8].

Fig. 3.1 shows the HF phase diagram[1] at the CNP as a function of twist angle and strain magnitude, for both $\varepsilon_r = 6$ and $\varepsilon_r = 12$. Two phases are clearly visible. The region in Fig. 3.1 with non-zero charge gap has KIVC order. The gapless region, on the other hand, corresponds to a semi-metal (SM) without spontaneous symmetry breaking. The HF band structure of the SM has two Dirac cones close to the Γ-point, and is therefore similar to the band structure of the strained BM Hamiltonian (for more details, see [96]). The transition from the KIVC state to the SM in Fig. 3.1 occurs at strain values $\epsilon \sim 0.4 - 0.6\%$ with $\varepsilon_r = 6$, and at $\epsilon \sim 0.1 - 0.2\%$ with $\varepsilon_r = 12$. These critical values lie exactly in the range of strain values observed in STM devices [18, 32, 35, 92], from which we conclude that strain plays an important role in TBG. From Fig. 3.1, we also see that the KIVC state is more robust at larger θ. Because at $\epsilon = 0$ the energy difference between the KIVC state and the SM depends only weakly on θ [8], we attribute this feature to the fact that the active bands are less affected by strain at larger θ (in particular, the Dirac points remain further away from Γ, and the change in bandwidth is smaller).

In Fig. 3.2(a) we plot the KIVC order parameter as a function of ϵ. The order parameter is defined as $|\Delta_{\text{KIVC}}| := \frac{1}{N}\sum_{\mathbf{k}} ||\mathsf{P}_{\text{IVC}}(\mathbf{k})||$, where N is the number of $\mathbf{k}$ values and P_{IVC} is the intervalley ($\tau \neq \tau'$) part of the KIVC correlation matrix $[\mathsf{P}(\mathbf{k})]_{(s,\tau,m),(s',\tau',n)} = \langle f^\dagger_{\mathbf{k},s',\tau',n} f_{\mathbf{k},s,\tau,m}\rangle$. We see that the transition occurs at $\epsilon_* \sim 0.19\%$ if we keep $N_b = 6$ BM bands per spin and valley. By increasing N_b, ϵ_* shifts to slightly smaller values, and converges for $N_b = 12$.

[1] Throughout this chapter, we allow HF to break all symmetries, except for translation symmetry.

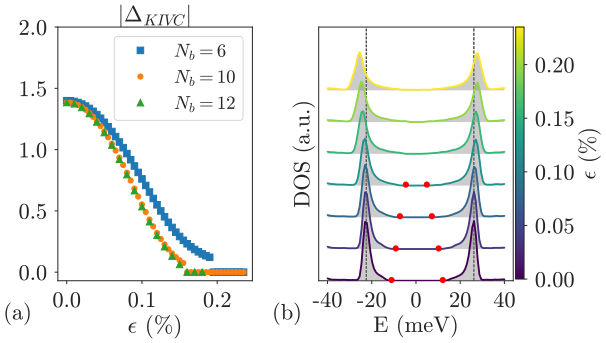

Figure 3.2: (a) KIVC order parameter $|\Delta_{\mathrm{KIVC}}| := \frac{1}{N}\sum_{\mathbf{k}} ||\mathsf{P}_{\mathrm{IVC}}(\mathbf{k})||$ at charge neutrality as a function of ϵ, obtained with SCHF using $\theta = 1.05°$, $\varepsilon_r = 10$ and $N_b = 6, 10$ or 12 bands per spin and valley. The calculations were done on a 24×24 momentum grid. (b) DOS of the SCHF band spectrum on a 36×36 momentum grid using $\theta = 1.05°$, $\varepsilon_r = 10$ and $N_b = 6$. The edges of the KIVC gap are indicated with red dots.

Fig. 3.2(a) shows a discontinuity in $|\Delta_{\mathrm{KIVC}}|$, implying that the transition is first order. However, we also find that close to the transition, $|\Delta_{\mathrm{KIVC}}|$ decreases by a factor of 20 (using $N_b = 12$) compared to its value at $\epsilon = 0$. We therefore cannot exclude that the weakly first-order behavior is an artifact of HF.

Fig. 3.2(b) shows the density of states (DOS) obtained in SCHF for different ϵ, interpolating between the KIVC insulator and the SM. The dominant feature for both the KIVC and SM DOS is a pair of broad peaks separated by $\sim 50\,\mathrm{meV}$. In the KIVC phase, there is a finite window around the Fermi energy where the DOS is zero, which decreases with ϵ and vanishes at the transition. This is a subtle feature, however, making it hard to sharply distinguish the SM from the KIVC. A finer probe for the properties of the SM is the (layer-resolved) local DOS (LDOS) [96]. In Fig. 3.3(a)-(b) we plot the LDOS of the SM at energies $E/W = -0.11$ and $E/W = 0.15$, where W is the HF bandwidth. The LDOS at the AA regions shows strong C_{3z} breaking. This strong C_{3z} breaking results from interactions, as it does not show up in the LDOS of the BM ground state at the same energy ratios $E/W_0 = -0.11$ and $E/W_0 = 0.15$, where W_0 is the BM bandwidth (see Fig. 3.3(c)-(d) and [96]). These properties of the HF LDOS agree with STM experiments [18, 32, 33]. In particular, Ref. [33] observed strong C_{3z} breaking at the CNP, but not at $\nu = 4$. We calculated the LDOS at this filling, where the active bands are fully filled, and indeed found almost no reconstruction of the BM LDOS by interactions, and as a result no strong C_{3z} breaking.

Finally, strain can be invoked to explain the degeneracies of the Landau fan near the CNP [90, 91] of the SM. At low densities quantum oscillations are governed by cyclotron orbits around the mini Dirac points, with two Dirac points for each of the four iso-spins. When mirror symmetry (C_{2x}) ensures that the two Dirac points are equivalent, the resulting Landau fan will have the 8-fold degeneracy $\nu_\phi = \pm 4, \pm 12, \pm 20, \cdots$, which is observed, for example, far from the magic angle. However, mirror symmetry is broken by strain: for example, at

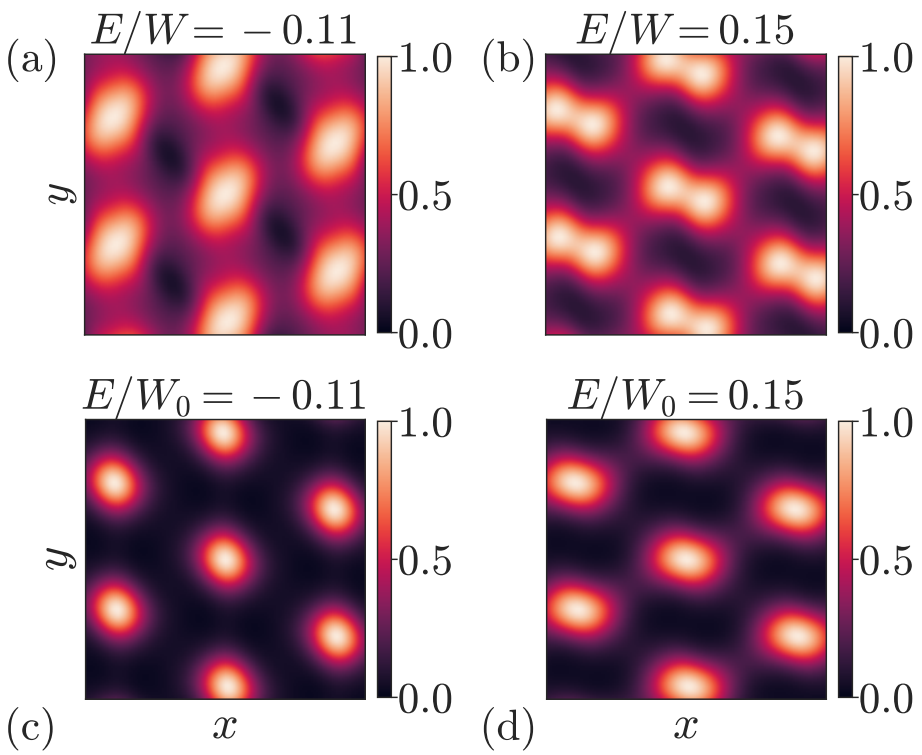

Figure 3.3: Normalized LDOS for $\theta = 1.05°$ and $\epsilon = 0.22\%$. (a)-(b) LDOS of the self-consistent SM (for $\varepsilon_r = 10$) at $E/W = -0.11$ and $E/W = 0.15$, where $W \sim 65$ meV is the HF bandwidth. (c)-(d) LDOS of the BM ground state at $E/W_0 = -0.11$ and $E/W_0 = 0.15$, where $W_0 \sim 17$ meV is the BM bandwidth.

$\epsilon = 0.22\%$ and $\varepsilon_r = 10$, we find that the two Dirac points in the same valley are separated in energy by $\Delta_D \sim 10$ meV. For generic B, this halves the degeneracy, $\nu_\phi = 0, \pm 4, \pm 8, \pm 12, \cdots$, as observed in most magic-angle experiments [2, 3]. When $|\nu| \gtrsim 0.25$, the cyclotron orbits of the two Dirac points merge and form one connected orbit with a 2π-Berry phase. Because the resulting Landau fan $\nu_\phi = \pm 4, \pm 8, \pm 12, \cdots$ has the same 4-fold degeneracy as the Δ_D-split Dirac points, the conclusion is the same. However we note that some devices show a crossover from a low-B 8-fold degeneracy to a high-B 4-fold degeneracy (for example, at $B \sim 1$T in Ref. [37]). It may be that in devices where the strain configuration happens to produce a small Δ_D, the mirror-breaking manifests in the terms which are linear in B.

3.4 DMRG at $\nu = -2$

While SCHF is a mean field approach, we may further confirm the existence of a strain-induced transition using unbiased DMRG calculations. In Ref. [8], it was argued that in the absence of strain, the ground state of the interacting Hamiltonian H at fillings $\nu = \pm 2$ is a spin polarized version of the KIVC state at neutrality. This claim was further substantiated

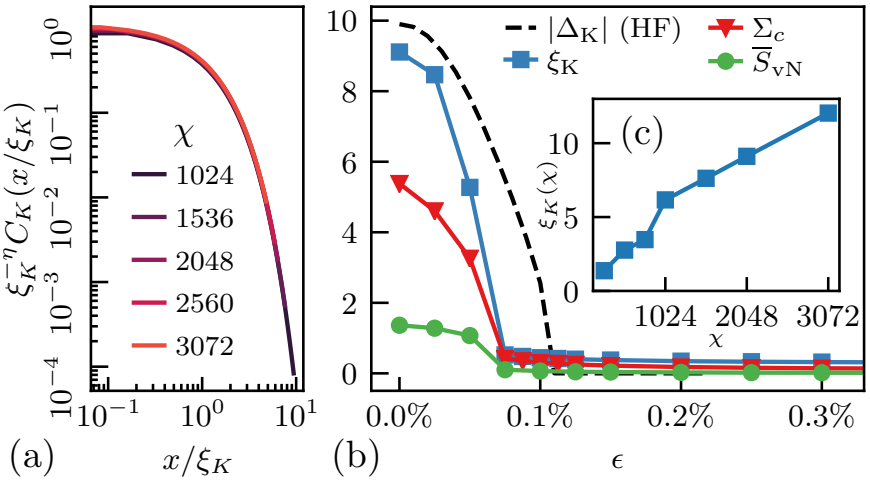

Figure 3.4: DMRG results at $\nu = -2$ (spin-polarized) at $\theta = 1.05°$ and $\varepsilon_r = 10$. (a) Scaling collapse of the KIVC correlator $C_K(x, \xi_K)$ at $\epsilon = 0$. (b) Transition from KIVC to SM with strain. KIVC correlation length ξ_K, average entropy $\bar{S}_{vN}$, the DMRG KIVC correlator $\Sigma_C = 10 \sum_x C_K(x)$ (scaled for visibility), and the HF KIVC correlator $|\Delta_{\text{KIVC}}|$ as a function of ϵ. (c) Scaling of ξ_K with bond dimension at $\epsilon = 0$. DMRG parameters: $L_y = 6$, $\Phi_y = 0$, $\chi \approx 2048$ for (b), and the Hamiltonian, Eq. (3.4), is represented to accuracy better than 0.1 meV. All quantities are defined in the text.

by Refs. [9, 53, 97]. Following the methods developed in Refs. [15, 38, 74], here we use infinite DMRG to study H compactified onto a infinitely long cylinder of circumference L_y moire cells. SCHF finds that the ground state is perfectly spin polarized for $\epsilon \lesssim 0.2\%$, so we accelerate our DMRG calculations by assuming full spin polarization of the narrow bands at $\nu = -2$, while keeping both valleys [96]. Projecting into the narrow bands, our computational basis for the four remaining active bands consists of hybrid Wannier orbitals that are localized in the x-direction, but have a well-defined momentum $k_y = 2\pi n/L_y$.

The ground state of the unstrained model at $\nu = -2$ is expected to have KIVC order, and thus to spontaneously break the $U(1)$ valley symmetry. The Hohenberg-Mermin-Wagner (HMW) theorem, however, forbids such continuous symmetry breaking on the quasi-1D cylinder geometry used by DMRG [98, 99]. Instead, the KIVC phase will manifest as algebraic long-range order [100] $C_K(x) := \langle \Delta_K^+(x) \Delta_K^-(0) \rangle \sim x^{-\eta(L_y)}$, where $\Delta_K^\pm(x)$ are operators at position x which have valley charge ± 2 and satisfy $\mathcal{T}'^{-1} O_K^\pm(x) \mathcal{T}' = O_K^\mp(x)$ [96]. The exponent $\eta(L_y)$ depends on the circumference, and satisfies $\eta(\infty) = 0$. An additional complication for identifying the KIVC phase using DMRG is that at any finite DMRG bond dimension χ (i.e., numerical accuracy), the ground state has exponentially decaying correlations. This complication can be overcome by using "finite entanglement scaling" [101–103] to characterize algebraic order via a scaling collapse as $\chi \to \infty$. Denoting the finite-χ induced correlation length as ξ_K [Fig. 4(c)], the KIVC correlator can be written as a general function $C_K(x, \xi_K)$. In the KIVC phase, we expect this function to satisfy the scaling relation $C_K(x, \xi_K) = \xi_K^{-\eta} C_K(x/\xi_K, 1)$, which allows us to perform a scaling collapse of the

data obtained at different χ. In Fig. 3.4(a), we find an excellent data collapse for χ ranging between 1024 and 3072, from which we conclude that DMRG indeed finds a KIVC ground state. Note that we find a very small exponent $\eta(6) \sim 0.06$ [96], so there is no regime of algebraic decay clearly visible in Fig. 3.4(a).

Fig. 3.4 (b) shows the effect of adding strain. Both the correlation length ξ_K and summed correlator $\Sigma_C := \sum_x C_K(x)$ measure the amount of KIVC correlations in the ground state. They are both order one for small strain, and decrease monotonically with ϵ. For $\epsilon \gtrsim 0.07\%$, however, ξ_K and Σ_C plateau at a small value, indicating that the algebraic KIVC order is destroyed. For strain values larger than $\sim 0.07\%$, we find no evidence for symmetry breaking in the DMRG ground state. In particular, we have verified that DMRG does not double the unit cell, which excludes the stripe phase discussed previously for single-valley models [15, 38]. The absence of symmetry breaking in DMRG is consistent with HF, where we find a symmetric SM at large ϵ [96]. Fig 4(b) plots the SCHF order parameter $|\Delta_{\mathrm{KIVC}}|$, which shows a transition from the KIVC state to the SM at a strain value $\epsilon \sim 0.1\%$, close to where the algebraic KIVC order disappears in DMRG. While the behaviour of the DMRG correlation length is consistent with a first-order transition, much larger bond dimensions — and cylinder circumferences — would be needed to decide this issue. To confirm that the large strain phase found with DMRG is the same SM obtained in SCHF, we compute the averaged single particle entropy $\bar{S}_{\mathrm{vN}} := -\frac{1}{N}\sum_{\mathbf{k}} \mathrm{tr}\,(\mathsf{P}(\mathbf{k}) \ln \mathsf{P}(\mathbf{k}))$. This quantity is zero iff the DMRG ground state is a Slater determinant. Fig 4(b) shows that $\bar{S}_{\mathrm{vN}}$ is negligibly small at $\epsilon \gtrsim 0.07\%$ (at smaller ϵ, HMW implies the KIVC state cannot be a symmetry breaking Slater determinant in DMRG, so $\bar{S}_{\mathrm{vN}}$ is order unity). It thus follows that (i) SCHF and DMRG agree closely for all strain, and are essentially identical at large ϵ and, (ii) the transition in DMRG is indeed from the KIVC state to the SM.

3.5 Discussion

The results presented in this chapter show that strain is likely responsible for the semimetallic behavior and strong C_{3z} breaking observed at the CNP of most TBG devices (for related discussions of the CNP physics, see Refs. [104, 105]). C_{3z} breaking has also been observed in TBG near $\nu = -2$ [31], and was discussed in various theoretical contexts in Refs. [106–109]. From our DMRG and SCHF results, we found that TBG couples strongly to strain both at $\nu = 0$ and $\nu = -2$. Two important questions that follow from this are (i) whether the strong coupling to strain persists to $\nu = -2-\delta$ with $\delta \sim 0.1-0.9$ (where nematicity was observed in experiment [31]), and (ii) whether strain is important for superconductivity. Our findings also invigorate the question about the origin of the insulating behavior consistently observed at $\nu = -2$, as we find that within the model studied here, strain drives the KIVC - SM transition at roughly the same ϵ for both $\nu = 0$ and $\nu = -2$. One possibility is that band structure effects we have neglected, such as lattice relaxation [39, 40] or non-local inter-layer tunneling [40, 110] stabilize the insulators at $\nu = \pm 2$ at larger strain values.

Chapter 4

Detecting symmetry breaking in magic angle graphene using scanning tunneling microscopy

4.1 Introduction

Since superconductivity and correlated insulators (CIs) were found in magic angle twisted bilayer graphene (MATBG) [1–3], there have been vigorous attempts to identify the nature of the ground states at integer fillings. While widely believed to arise from spontaneous symmetry-breaking in the space of spin and valley, theoretical works have identified a wealth of candidate states which are close in energy, including insulators in the $U(4) \times U(4)$ manifold [8, 9, 111], a nematic semi-metal (nSM) [18, 62], and the incommensurate Kekulé spiral (IKS) [12]. However, clear experimental identification of the ground state order has proven difficult.

Scanning tunneling microscopy (STM), which measures the local density of states (LDOS), is a promising tool for distinguishing between these phases. Thus far STM measurements in MATBG have largely focused on modulations in the LDOS at the Moiré-scale [18, 23, 32, 33, 35]. STM has found evidence for a "cascade" of putative symmetry breaking transitions [23, 112], but has not yet detected the relevant order parameters. Take, for example, the Kramers-intervalley coherent (K-IVC) state [8, 9, 12, 97] and the nSM [62], which are believed to compete at the charge neutrality point (CNP) [16, 113, 114]. While there are quantitative differences between the DOS of the two phases (they are gapped and semimetallic respectively), given finite energy resolution their DOS are in practice very similar (Fig. 4.1(c)), making discrimination difficult [16]. Furthermore, the Moiré-scale spatial modulation of the LDOS is largely dominated by the peaks at the triangular-lattice of AA-regions [18, 32, 33]. This is a feature of the flat bands common to all the phases, and it is thus inadequate for identifying the ground state. What is needed is a probe capable of directly measuring the order parameter of the symmetry breaking.

In this chapter we show that atomically-resolved STM measurements are an ideal method

for distinguishing between these competing states. By measuring sublattice polarization, bond nematicity, and Kekulé pattern, we can distinguish the following states based on their symmetry properties: 1) symmetric Dirac semimetal 2) nSM 3) K-IVC 4) Generic IVC state (e.g. IKS) 5) valley Hall (VH) and 6) valley polarized (VP) (Table. 4.1, Fig. 4.1).

The fact that the K-IVC can be distinguished from a generic IVC state may come as a surprise. This is because the "Kramer's time-reversal" symmetry $\mathcal{T}'$ extinguishes any Kekulé charge-density signal. Applying perpendicular magnetic field breaks this symmetry, which reveals the underlying IVC nature of the state.

The ability of atomically-resolved STM to detect symmetry breaking in low-density flat-bands was recently demonstrated experimentally by Liu et al. [115]. They were able to probe the symmetry breaking in the zeroth Landau-level of monolayer graphene by directly measuring sublattice polarization and Kekulé order. As the Landau-levels and MATBG bands have comparable electron densities and energy scales, their findings are encouraging for the analogous measurements in MATBG.

4.2 Active bands of twisted bilayer graphene

We first review the flat band physics of MATBG and set the notation. We focus on a single spin-species case for simplicity. A convenient basis for the four flatbands (per spin) of MATBG is the "Chern" (or chiral) basis $|\mathbf{k}, \tau, C\rangle$, where $\mathbf{k}$ is crystal momentum in the mini-BZ, $\tau = \pm 1$ is the valley label, and $C = \pm 1$ is the Chern number [7, 8]. We can obtain the Chern basis by demanding $\mathcal{C}_2\mathcal{T}$ symmetry to act as $\mathcal{C}_2\mathcal{T}\,|k, \tau, C\rangle = |k, \tau, -C\rangle$. To a good approximation, the Chern basis is sublattice-polarized according to $A/B = \sigma = C\tau$. We further gauge-fix by demanding two-fold rotation $\mathcal{C}_2$ to act as $\mathcal{C}_2\,|k, \tau, C\rangle = |-\mathbf{k}, -\tau, C\rangle$.

Neglecting small Umklapp terms, the Hamiltonian is invariant under valley-dependent phase rotation $U_V(1)$. Using the Pauli matrix notation for τ, the action of $U_V(1)$ is written as $e^{i\tau_z\theta}\,|\mathbf{k}, \tau, C\rangle = e^{i\tau\theta}\,|\mathbf{k}, \tau, C\rangle$.

4.3 STM-spectroscopy from self-consistent Hartree-Fock calculation

Let us now review our numerical method. While many of our predictions presented below are based on symmetry considerations, we also numerically computed the LDOS of various competing phases using self-consistent Hartree-Fock (HF) method. We consider an interacting Hamiltonian in which the Coulomb interaction is projected into the flatbands of the Bistritzer-MacDonald (BM) continuum model [4]. Several studies have shown that HF is accurate at even-integer fillings [8, 9, 42, 64, 97, 116], in some cases producing ground states

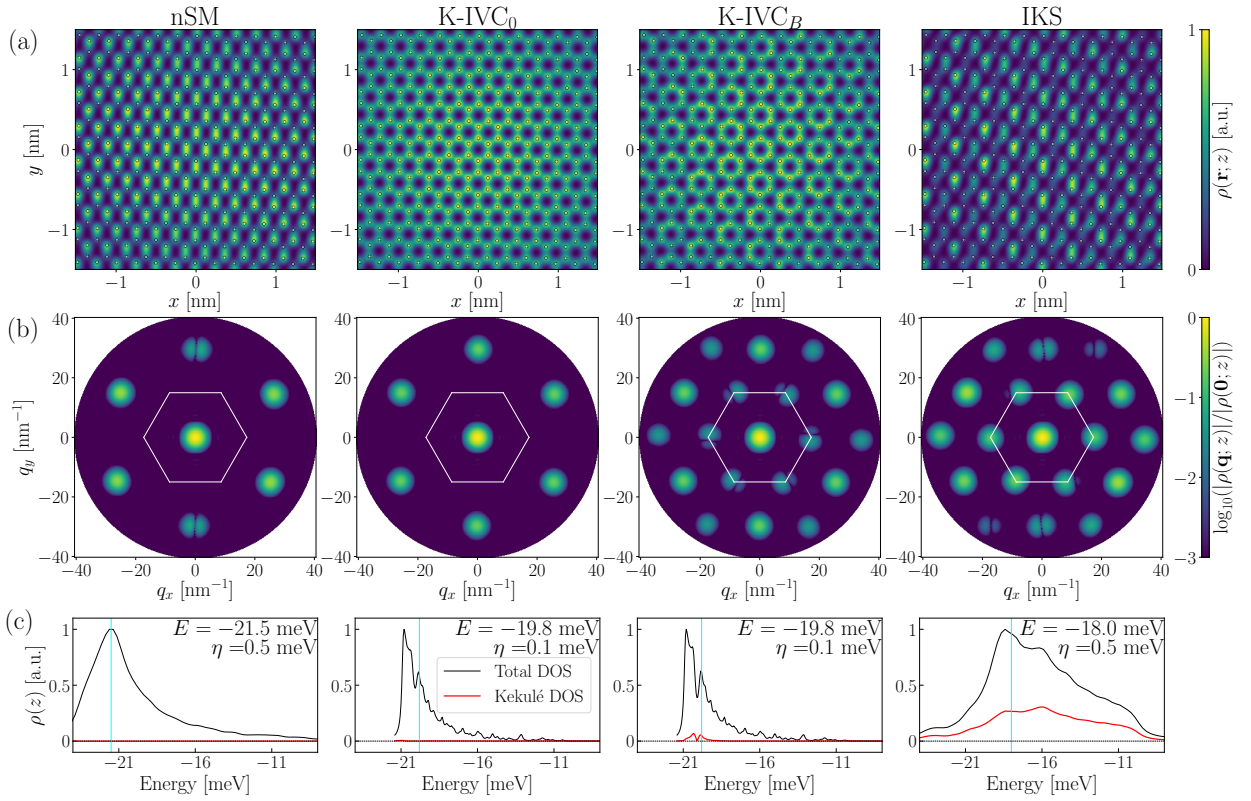

Figure 4.1: Spectroscopy calculation results for the self-consistent HF solutions of spinless nSM, K-IVC$_0$, K-IVC$_B$ states at CNP ($\nu = 0$) and IKS states at $\nu = -1$. We present (a) total LDOS $\rho(\mathbf{r}; z)$ (b) total FTLDOS $\rho(\mathbf{q}; z)$ (c) total and Kekulé -DOS $\rho(z = E+i\eta)$ signals for the bottom layer AA-region of MATBG. The signals are normalized by their maximum. For FTLDOS, logarithm is taken on the normalized signals. Cyan lines in (c) indicate the scanning-energy, and the energy range was chosen to show the occupied states. White dots in (a) denote carbon lattice sites.

nearly identical to the semi-exact solutions obtained from DMRG and exact diagonalization [15, 16, 38, 117].

We also incorporate the effect of a perpendicular magnetic field via the phenomenological Hamiltonian $H_{\text{pert}} = E_B C$, where $E_B = 0.1\,\text{meV}$. This choice will be justified in a later section. States under magnetic field are denoted by a subscript B.

We use the single-particle eigenstates $|E_i\rangle$ of the HF effective Hamiltonian H_{eff} to obtain the LDOS:

$$\text{LDOS}(E, \mathbf{r}) = -\frac{1}{\pi}\Im \sum_i \frac{|\langle \mathbf{r}|E_i\rangle|^2}{E_i - E + i\eta}, \tag{4.1}$$

where E is the scanning-energy of the electron and η is a Lorentzian-broadening parameter [1]. We may similarly obtain the Fourier-transformed LDOS (FTLDOS) $\rho(\mathbf{q}; E)$, and the total

[1]Note that $V_b = E/e$ is the bias voltage (not measured from the Fermi level, but rather from $E = 0$

Phase	$U_V(1)$	$\mathcal{T}'$	$\mathcal{C}_3$	Kekulé		S.L. Pol.	
				$B=0$	$B\neq 0$	$B=0$	$B\neq 0$
DSM	✓	✓	✓	✗	✗	✗	✗
nSM	✓	✓	✗	✗	✗	✗	✗
VH	✓	✓	✓	✗	✗	✓	✓
VP	✓	✗	✓	✗	✗	✗	✓
K-IVC	✗	✓	✓	✗	✓	✗	✗
IKS	✗	✗	✗	✓	✓	✗	✗

Table 4.1: Symmetry properties of various ground state candidate states. DSM stands for symmetric Dirac semimetal. The column for Kekulé denotes absence (✗) or presence (✓) of Kekulé pattern in LDOS. The column for S.L. Pol. indicates whether the LDOS is A/B sublattice polarized at the very center of the AA-stacking region, when averaging over 3 unit cells to remove contributions from the Kekulé signal.

DOS $\rho(E)$. We refer to App. C for the full specification of the model, HF calculations, and LDOS/FTLDOS/total DOS calculations.

4.4 STM-spectroscopy of competing phases

Different ground state candidates have different symmetry properties (Table. 4.1), which allow us to distinguish them using STM. The main features are 1) Breaking of $\mathcal{C}_2$ symmetry via sublattice polarization, 2) breaking of $\mathcal{C}_3$ symmetry via bond nematicity, and 3) breaking of graphene-scale translation symmetry via a Kekulé pattern. In order to observe rotational symmetry breaking, we measure the LDOS around $\mathcal{C}_2$ and $\mathcal{C}_3$ symmetry invariant AA-region (AB/BA-region can also show interesting features[App. C]).

To illustrate this point, here we will focus on the following three states that were shown by prior works to be most competitive at even integer fillings of the spinful model: the nSM [15, 38, 62], K-IVC [8, 9, 16, 97], and IKS [12]. These states are predicted to undergo a quantum phase transition to each other under change of heterostrain [12, 16], so it is of great interest to distinguish them using a local probe.

In Fig. 4.1, we present the total LDOS/FTLDOS/DOS of the bottom layer in the region of AA-stacking for these phases. Let us now walk through the features which are characteristic of each phase.

(i) nSM: Reflecting the nematic nature of the state, the LDOS strongly breaks $\mathcal{C}_3$ but preserves $\mathcal{C}_2$. The order manifests in two forms: first, in the orientation of the strong bonds, and second, while the very center of the AA-region has equal weight on the two sublattices, to the right(left) the dominant weight shifts to the $A(B)$ sublattice. This polarization is not observed along the axis rotated by $2\pi/3$ (Fig. 4.1 (a)). FTLDOS also show nematicity, where *two* of the six Bragg peaks (at the reciprocal vectors of the graphene lattice) have a

determined by our numerical conventions)

nodal line across which the phase changes over the mini-BZ (Fig. 4.1 (b)). Similar nematic behavior was observed in earlier STM experiments [33].

(ii-a) K-IVC$_0$: The LDOS respects all the symmetries (Fig. 4.1 (a)). The absence of a Kekulé pattern despite the inter-valley coherence is enforced by the $\mathcal{T}'$-selection rule to be derived later. The FTLDOS is peaked only at the graphene reciprocal vectors (Fig. 4.1 (b)).

(ii-b) K-IVC$_B$: For *a small range of tunneling bias* (Fig. 4.1 (c)) the LDOS shows a $\sqrt{3}\times\sqrt{3}$ Kekulé pattern respecting $\mathcal{C}_3$. The FTLDOS exhibits dominant peaks at the Bragg points and subdominant peaks at intervalley-scattering momenta $K-K'$ (Fig. 4.1 (b)). The Kekulé signal only shows up for a range of bias close to the van-Hove peak (see Kekulé -DOS, Fig. 4.1(c)), and in fact the signal changes sign as the peak is crossed. The origin of this energy dependence will become clear shortly.

(iii) IKS: The LDOS exhibits a $\sqrt{3}\times\sqrt{3}$ bond nematic pattern(Fig. 4.1 (a)). [2]. The graphene Bragg peaks show similar nodal line as in the nSM (Fig. 4.1 (b)), reflecting the similarity of IKS to nSM [12]. The Kekulé -DOS is on the same order as the total DOS over the entire range of occupied band energies (Fig. 4.1 (c)) [3].

The other three phases (DSM, VP, and VH) are discussed in detail in the SM [App. C].

4.5 Vanishing Kekulé signal of the K-IVC state

We now explain why the K-IVC Kekulé signal emerges only in a magnetic field. We focus on the spinless case for simplicity, and leave the spinful case to the SM [App. C]. In Ref. [8] it was shown that the K-IVC state produces a Kekulé -like pattern of circulating *currents* not charge, as shown in Fig. 4.2(a). This is a consequence of a modified "Kramer's" time-reversal symmetry of K-IVC $\mathcal{T}'=\tau_z\mathcal{T}$ which applies a π-phase rotation between the valleys [8]. We may formalize this extinction as a selection rule on the FTLDOS

$$\rho(\mathbf{q};z=E+i\eta)=\frac{-1}{2\pi i}\left(\mathrm{Tr}[\hat{\rho}_{\mathbf{q}}\hat{G}(z)]-\overline{\mathrm{Tr}[\hat{\rho}_{-\mathbf{q}}\hat{G}(z)]}\right), \tag{4.2}$$

where $\hat{G}(z)$ is the electron Green's function and $\hat{\rho}_{\mathbf{q}}=e^{-i\mathbf{q}\cdot\hat{\mathbf{r}}}$ is the density operator [App. C]. The "Kekulé -LDOS" is the portion of the FTLDOS at inter-valley momentum transfer $\mathbf{q}=\pm(K-K')+\Delta\mathbf{q}$, where $\Delta\mathbf{q}$ is small.

We consider either a unitary symmetry with $\mathcal{U}^{-1}\hat{G}(z)\mathcal{U}=\hat{G}(z)$ or an anti-unitary symmetry with $\mathcal{K}^{-1}\hat{G}(z)\mathcal{K}=\hat{G}^{\dagger}(z)$. Suppose further that for some $\mathbf{q}$ of interest the density transforms either as $\mathcal{U}^{-1}\hat{\rho}_{\mathbf{q}}\mathcal{U}=\pm\hat{\rho}_{\mathbf{q}}$, or $\mathcal{K}^{-1}\hat{\rho}_{\mathbf{q}}\mathcal{K}=\pm\hat{\rho}_{-\mathbf{q}}$, where the sign $\pm$ will depend on the symmetry. By inserting these transformations into Eq.(4.2) [App. C], we obtain $\rho(\mathbf{q};z)=\pm\rho(\mathbf{q};z)$. The odd case then enforces an extinction.

[2] IKS (and likewise K-IVC) state enjoys $\mathcal{C}_2\mathcal{T}$ symmetry only when θ_{IVC} takes particular values

[3] As demonstrated in [App. C], the Kekulé -DOS signals however vanish for some of the conduction bands due to loss of inter-valley coherence.

For the case at hand, we expand the inter-valley part of $\hat{\rho}_{\mathbf{q}}$ in a plane-wave basis $\langle \mathbf{r}|\mathbf{k},\tau\rangle \propto e^{i(\mathbf{k}+K_\tau)\cdot\mathbf{r}}$

$$\hat{\rho}_{(\mathbf{q}=K-K'+\Delta\mathbf{q})} = \sum_{\mathbf{k}} |\mathbf{k}+\Delta\mathbf{q},\tau=1\rangle\langle\mathbf{k},\tau=-1|\,, \tag{4.3}$$

where $\mathbf{k}$ is restricted to the vicinity of the graphene Dirac points. In the absence of IVC order, the symmetry $\mathcal{U}=\tau_z \in U_V(1)$ gives $\mathcal{U}^{-1}\hat{\rho}_{\mathbf{q}}\mathcal{U} = -\hat{\rho}_{\mathbf{q}}$, enforcing an extinction, while for a generic IVC the Kekulé -LDOS will be present. For the K-IVC we instead leverage $\mathcal{T}'|\mathbf{k},\tau\rangle = \tau|-\mathbf{k},-\tau\rangle$, giving $\mathcal{T}'^{-1}\hat{\rho}_{\mathbf{q}}\mathcal{T}' = -\hat{\rho}_{-\mathbf{q}}$, and conclude the K-IVC has vanishing Kekulé -LDOS.

4.6 Effect of a $\mathcal{T}'$-breaking perturbation

In the presence of a $\mathcal{T}'$-breaking perturbation H_{pert} - e.g., an applied perpendicular magnetic field B - the selection rule is inoperative and the K-IVC$_B$ phase will generically manifest a Kekulé pattern. In order to understand its magnitude and the sensitive E-dependence found in Fig. 4.1(c), we now analyze an approximate form of H_{pert} in detail.

An out-of plane B-field will have two effects. First, it will reconstruct the flat bands into a Hofstadter butterfly; however this effect is small for weak ($B < 1\,\text{T}$) fields [4]. Second, B will couple to the orbital magnetic moment $m(\mathbf{k},\tau,C) = \mu_B g(\mathbf{k},\tau,C)$ of the flat bands, where $g \sim 2-10$ [28, 55, 118]. For simplicity we neglect the $\mathbf{k}$-dependence, in which case symmetry enforces the simpler form $m(\mathbf{k},\tau,C) = \mu_B g\, C$, so that $H_{\text{pert}} = E_B C, E_B = \mu_B g B$. For a $B = 1\,\text{T}$ field, $E_B \sim 0.1\,\text{meV}$ is thus a conservative estimate of its magnitude.

To compute the change in the LDOS, we diagonalize $H_{\text{eff}} + H_{\text{pert}}$, as shown schematically in Fig. 4.2(b). Since H_{pert} is small compared to the gap $\Delta_{\text{KIVC}} \sim 20\,\text{meV}$ of H_{eff} (Fig. 4.3(a)), we project H_{pert} into the space spanned by the two occupied eigenstates $|\mathbf{k}, n=0/1\rangle$ of H_{eff}. To constrain the form of H_{pert}, we combine $\mathcal{C}_2$, $\mathcal{T}$, and a relative valley phase to obtain a second symmetry of the K-IVC, $\mathcal{C}_2\mathcal{T}'' = \mathcal{C}_2\mathcal{T}e^{i\tau_z(\theta_{\text{IVC}}-\pi/2)/2}$, which acts locally in $\mathbf{k}$. Because $E_B C$ anti-commutes with $\mathcal{C}_2\mathcal{T}''$, the projection is constrained to take the general form

$$[H_{\text{eff}} + H_{\text{pert}}](\mathbf{k}) = \begin{pmatrix} E_0(\mathbf{k}) & 0 \\ 0 & E_1(\mathbf{k}) \end{pmatrix} + \begin{pmatrix} 0 & \Delta_B(\mathbf{k}) \\ \overline{\Delta}_B(\mathbf{k}) & 0 \end{pmatrix}. \tag{4.4}$$

The effect of the perturbation is controlled by the ratio of $\Delta E(\mathbf{k}) = E_1(\mathbf{k}) - E_0(\mathbf{k})$ and the perturbation $\Delta_B(\mathbf{k})$. In Fig. 4.3(a,c) we see that $\Delta E(\mathbf{k})$ is much smaller than the band-gap Δ_{KIVC} across most of the mini-BZ. A small Δ_B could thus result in a significant change in the LDOS even while the ground-state itself changes by a negligible amount of order $H_{\text{pert}}/\Delta_{\text{KIVC}} \ll 1$.

It is instructive to construct eigenstates of H_{pert} in terms of the valley/Chern basis $|\mathbf{k},\tau,C\rangle$. In the strong-coupling limit, it is given by the following Chern polarized states

[4] At 1 T, the magnetic flux that goes through a Moiré unit cell is about 3% of the flux quantum

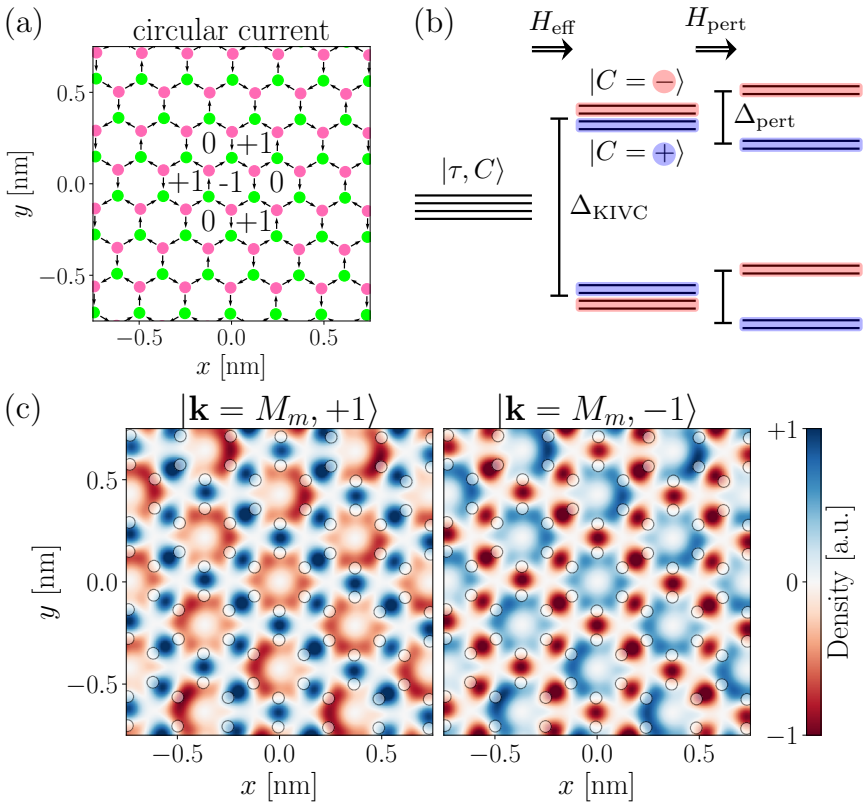

Figure 4.2: (a) Total current-density of K-IVC eigenstates (Eq.(4.5)) $|\mathbf{k} = M_m, n = \pm 1\rangle$. M_m is the M-point of the mini-BZ. Lime/pink dots are the A/B sublattice sites. (b) Schematic representation of the energy levels of K-IVC. From left to right: the basis states; K-IVC eigenstates; perturbation eigenstates (Eq.(4.4)). Red(blue) corresponds to superposed states with predominantly Chern $+1$ (-1) character. (c) Kekulé charge-density of $|\mathbf{k} = M_m, \text{occ}, n = \pm 1\rangle$.

that span the occupied K-IVC bands[8]:

$$|\mathbf{k}, \text{occ}, +\rangle \approx (|\mathbf{k}, +, +\rangle + e^{i\theta_{\text{IVC}}} |\mathbf{k}, -, +\rangle)/\sqrt{2}, \tag{4.5}$$

$$|\mathbf{k}, \text{occ}, -\rangle \approx (|\mathbf{k}, +, -\rangle - e^{i\theta_{\text{IVC}}} |\mathbf{k}, -, -\rangle)/\sqrt{2}. \tag{4.6}$$

Individually, each Chern sector $|\mathbf{k}, \text{occ}, \pm\rangle$ contributes to Kekulé -LDOS, as in Fig. 4.2(c). However, $\mathcal{T}'$ ensures that the Kekulé contribution from $|\mathbf{k}, \text{occ}, +\rangle$ and $|-\mathbf{k}, \text{occ}, -\rangle$ cancel [App. C]. The perturbation, however, shifts their contributions to the LDOS in energy, and a net signal appears.

4.7 K-IVC band-structure

As an explicit illustration of the $\mathcal{T}'$-breaking mechanism we compute the band-structures of K-IVC$_0$ and K-IVC$_B$. The occupied DOS of KIVC$_0$ (Fig. 4.3(d)) has a dominant peak

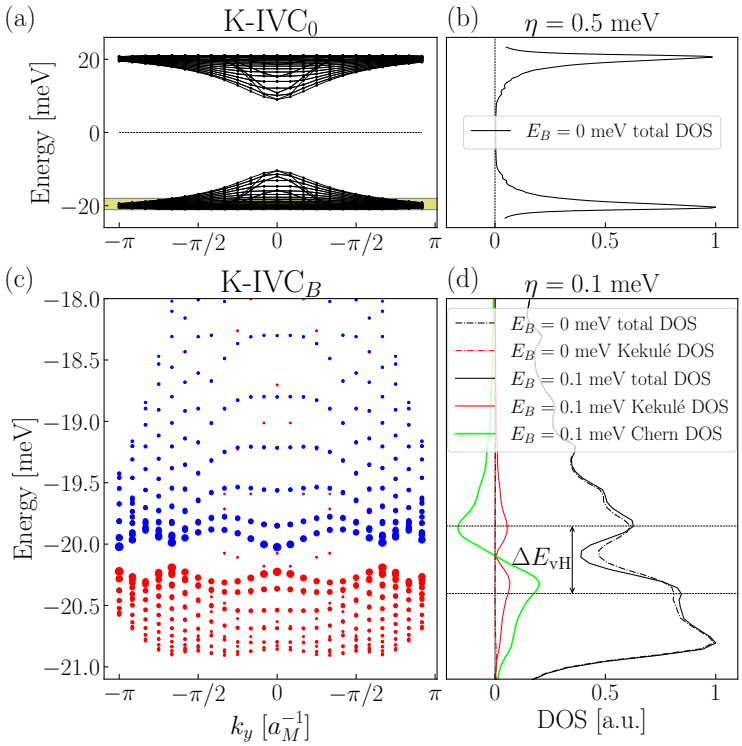

Figure 4.3: (a-b) Self-consistent HF band-structure and DOS of K-IVC$_0$ at CNP and $\eta = 0.5\,\mathrm{meV}$. Yellow patch denotes the spectrum within valence bands probed at $\eta = 0.1\,\mathrm{meV}$ in (c-d). (c) Band-structure of K-IVC$_B$ at $E_B = 0.1$ meV. Area of the blue (red) dots corresponds to the degree of positive (negative) Chern polarization of the wavefunction. (d) Total/Kekulé -DOS of K-IVC$_0$ and K-IVC$_B$ along with Chern polarization-weighted total DOS.

at $E_{\mathrm{vH}} \sim -20\,\mathrm{meV}$ which is in fact composed of *two* van-Hove singularities separated by $\Delta E_{\mathrm{vH}} \sim 0.5\,\mathrm{meV}$. These two peaks originate from two different bands $|\mathbf{k}, n = 0/1\rangle$, so we may estimate $|\Delta E(\mathbf{k})| \sim \Delta E_{\mathrm{vH}}$. Indeed, the eigenstates of K-IVC$_B$ shows substantial Chern-polarization (Fig. 4.3(c)) for $E_B = 0.1\,\mathrm{meV}$. When probing the LDOS at energies near the higher (lower) vH peak, we couple predominantly to the $C = 1(-1)$ sector, and hence their Kekulé signals (Fig. 4.2(c)) no longer cancel. The two peaks have opposite Kekulé signal; for the experiment to work, it is thus crucial that the broadening η remains smaller than the peak separation $\sim \Delta E_{\mathrm{vH}}$.

4.8 Discussion

There has already been some work on atomically-resolved STM measurement of MATBG. In particular, Ref. [33] found a nematic state at the CNP, and observed a stripe-like signal in the atomically-resolved LDOS of the AB/BA-regions. This feature is consistent with our

LDOS calculations for the nSM (see [App. C] for AB/BA-regions), suggesting they have identified the nSM as the ground state of this sample.

We note that while we have analyzed insulators of MATBG, the symmetry analysis applies more generally. It should thus be possible to map out the symmetry-breaking order as a function of electron density, and correlate it with the observed "cascade". Furthermore, since magic angle twisted trilayer graphene (MATTG) features the same symmetries and band topology [119–121], our conclusions apply to STM measurements [122, 123] of MATTG *mutatis mutandis*.

Bibliography

[1] Yuan Cao et al. "Correlated Insulator Behaviour at Half-Filling in Magic-Angle Graphene Superlattices". en. In: *Nature* 556.7699 (Apr. 2018), pp. 80–84. ISSN: 1476-4687. DOI: 10.1038/nature26154.

[2] Yuan Cao et al. "Unconventional Superconductivity in Magic-Angle Graphene Superlattices". In: *Nature* 556.7699 (Apr. 2018), pp. 43–50. ISSN: 1476-4687. DOI: 10.1038/nature26160.

[3] Matthew Yankowitz et al. "Tuning superconductivity in twisted bilayer graphene". In: *Science* (2019), p. 1910.

[4] Rafi Bistritzer and Allan H. MacDonald. "Moiré Bands in Twisted Double-Layer Graphene". en. In: *Proceedings of the National Academy of Sciences* 108.30 (July 2011), pp. 12233–12237. ISSN: 0027-8424, 1091-6490. DOI: 10.1073/pnas.1108174108.

[5] Jeil Jung and Allan H. MacDonald. "Accurate tight-binding models for the π bands of bilayer graphene". In: *Phys. Rev. B* 89 (3 Jan. 2014), p. 035405. DOI: 10.1103/PhysRevB.89.035405. URL: https://link.aps.org/doi/10.1103/PhysRevB.89.035405.

[6] J. M. B. Lopes dos Santos, N. M. R. Peres, and A. H. Castro Neto. "Graphene Bilayer with a Twist: Electronic Structure". In: *Phys. Rev. Lett.* 99 (25 Dec. 2007), p. 256802. DOI: 10.1103/PhysRevLett.99.256802. URL: https://link.aps.org/doi/10.1103/PhysRevLett.99.256802.

[7] Grigory Tarnopolsky, Alex J. Kruchkov, and Ashvin Vishwanath. "Origin of Magic Angles in Twisted Bilayer Graphene". In: *Physical Review Letters* 122.10 (Mar. 2019), p. 106405. ISSN: 0031-9007, 1079-7114. DOI: 10.1103/PhysRevLett.122.106405. arXiv: 1808.05250.

[8] Nick Bultinck et al. "Ground State and Hidden Symmetry of Magic-Angle Graphene at Even Integer Filling". In: *Phys. Rev. X* 10 (3 Aug. 2020), p. 031034. DOI: 10.1103/PhysRevX.10.031034. URL: https://link.aps.org/doi/10.1103/PhysRevX.10.031034.

[9] Biao Lian et al. "Twisted bilayer graphene. IV. Exact insulator ground states and phase diagram". In: *Phys. Rev. B* 103 (20 May 2021), p. 205414. DOI: 10.1103/PhysRevB.103.205414. URL: https://link.aps.org/doi/10.1103/PhysRevB.103.205414.

[10] Eslam Khalaf et al. "Charged skyrmions and topological origin of superconductivity in magic-angle graphene". In: *Science Advances* 7.19 (2021), eabf5299. DOI: 10.1126/sciadv.abf5299. URL: https://www.science.org/doi/abs/10.1126/sciadv.abf5299.

[11] Steven R White. "Density matrix formulation for quantum renormalization groups". In: *Physical review letters* 69.19 (1992), p. 2863.

[12] Y. H. Kwan et al. "Kekulé Spiral Order at All Nonzero Integer Fillings in Twisted Bilayer Graphene". In: *Phys. Rev. X* 11 (4 Dec. 2021), p. 041063. DOI: 10.1103/PhysRevX.11.041063. URL: https://link.aps.org/doi/10.1103/PhysRevX.11.041063.

[13] Tianle Wang et al. *Kekulé spiral order in magic-angle graphene: a density matrix renormalization group study*. 2022. arXiv: 2211.02693 [cond-mat.str-el].

[14] Kevin P. Nuckolls et al. *Quantum textures of the many-body wavefunctions in magic-angle graphene*. 2023. arXiv: 2303.00024 [cond-mat.mes-hall].

[15] Tomohiro Soejima et al. "Efficient simulation of moiré materials using the density matrix renormalization group". In: *Phys. Rev. B* 102 (20 Nov. 2020), p. 205111. DOI: 10.1103/PhysRevB.102.205111. URL: https://link.aps.org/doi/10.1103/PhysRevB.102.205111.

[16] Daniel E. Parker et al. "Strain-Induced Quantum Phase Transitions in Magic-Angle Graphene". In: *Physical Review Letters* 127.2 (July 2021), p. 027601. DOI: 10.1103/PhysRevLett.127.027601.

[17] Jung Pyo Hong, Tomohiro Soejima, and Michael P. Zaletel. "Detecting Symmetry Breaking in Magic Angle Graphene Using Scanning Tunneling Microscopy". In: *Phys. Rev. Lett.* 129 (14 Sept. 2022), p. 147001. DOI: 10.1103/PhysRevLett.129.147001. URL: https://link.aps.org/doi/10.1103/PhysRevLett.129.147001.

[18] Youngjoon Choi et al. "Electronic Correlations in Twisted Bilayer Graphene near the Magic Angle". In: *Nature Physics* 15.11 (Nov. 2019), pp. 1174–1180. ISSN: 1745-2481. DOI: 10.1038/s41567-019-0606-5.

[19] Hyobin Yoo et al. "Atomic and Electronic Reconstruction at the van Der Waals Interface in Twisted Bilayer Graphene". en. In: *Nature Materials* 18.5 (May 2019), pp. 448–453. ISSN: 1476-4660. DOI: 10.1038/s41563-019-0346-z.

[20] Aaron L. Sharpe et al. "Emergent ferromagnetism near three-quarters filling in twisted bilayer graphene". In: *Science* 365.6453 (Aug. 2019), pp. 605–608. DOI: 10.1126/science.aaw3780. arXiv: 1901.03520 [cond-mat.mes-hall].

[21] M. Serlin et al. "Intrinsic quantized anomalous Hall effect in a moiré heterostructure". In: *Science* 367.6480 (2020), pp. 900–903. ISSN: 0036-8075. DOI: 10.1126/science.aay5533. URL: https://science.sciencemag.org/content/367/6480/900.

[22] S. L. Tomarken et al. "Electronic Compressibility of Magic-Angle Graphene Superlattices". In: *Phys. Rev. Lett.* 123 (4 July 2019), p. 046601. DOI: 10.1103/PhysRevLett.123.046601. URL: https://link.aps.org/doi/10.1103/PhysRevLett.123.046601.

[23] Dillon Wong et al. "Cascade of Electronic Transitions in Magic-Angle Twisted Bilayer Graphene". In: *Nature* 582.7811 (June 2020), pp. 198–202. ISSN: 1476-4687. DOI: 10.1038/s41586-020-2339-0.

[24] U. Zondiner et al. "Cascade of Phase Transitions and Dirac Revivals in Magic-Angle Graphene". en. In: *Nature* 582.7811 (June 2020), pp. 203–208. ISSN: 1476-4687. DOI: 10.1038/s41586-020-2373-y.

[25] Harpreet Singh Arora et al. "Superconductivity in Metallic Twisted Bilayer Graphene Stabilized by WSe 2". en. In: *Nature* 583.7816 (July 2020), pp. 379–384. ISSN: 1476-4687. DOI: 10.1038/s41586-020-2473-8.

[26] Kevin P. Nuckolls et al. "Strongly Correlated Chern Insulators in Magic-Angle Twisted Bilayer Graphene". In: *Nature* 588.7839 (Dec. 2020), pp. 610–615. ISSN: 1476-4687. DOI: 10.1038/s41586-020-3028-8. (Visited on 03/15/2022).

[27] Shuang Wu et al. "Chern Insulators, van Hove Singularities and Topological Flat Bands in Magic-Angle Twisted Bilayer Graphene". In: *Nature Materials* 20.4 (Apr. 2021), pp. 488–494. ISSN: 1476-4660. DOI: 10.1038/s41563-020-00911-2.

[28] C. L. Tschirhart et al. "Imaging orbital ferromagnetism in a moiré Chern insulator". In: *Science* 372.6548 (2021), pp. 1323–1327. DOI: 10.1126/science.abd3190. eprint: https://www.science.org/doi/pdf/10.1126/science.abd3190. URL: https://www.science.org/doi/abs/10.1126/science.abd3190.

[29] Xiaobo Lu et al. "Multiple flat bands and topological Hofstadter butterfly in twisted bilayer graphene close to the second magic angle". In: *Proceedings of the National Academy of Sciences* 118.30 (2021), e2100006118. DOI: 10.1073/pnas.2100006118. eprint: https://www.pnas.org/doi/pdf/10.1073/pnas.2100006118. URL: https://www.pnas.org/doi/abs/10.1073/pnas.2100006118.

[30] Xiaoxue Liu et al. "Tuning electron correlation in magic-angle twisted bilayer graphene using Coulomb screening". In: *Science* 371.6535 (2021), pp. 1261–1265. DOI: 10.1126/science.abb8754. eprint: https://www.science.org/doi/pdf/10.1126/science.abb8754. URL: https://www.science.org/doi/abs/10.1126/science.abb8754.

[31] Yuan Cao et al. "Nematicity and competing orders in superconducting magic-angle graphene". In: *Science* 372.6539 (2021), pp. 264–271. DOI: 10.1126/science.abc2836. eprint: https://www.science.org/doi/pdf/10.1126/science.abc2836. URL: https://www.science.org/doi/abs/10.1126/science.abc2836.

[32] Alexander Kerelsky et al. "Maximized Electron Interactions at the Magic Angle in Twisted Bilayer Graphene". en. In: *Nature* 572.7767 (Aug. 2019), pp. 95–100. ISSN: 1476-4687. DOI: 10.1038/s41586-019-1431-9.

[33] Yuhang Jiang et al. "Charge Order and Broken Rotational Symmetry in Magic-Angle Twisted Bilayer Graphene". In: *Nature* 573.7772 (Sept. 2019), pp. 91–95. ISSN: 1476-4687. DOI: 10.1038/s41586-019-1460-4.

[34] Xiaobo Lu et al. "Superconductors, Orbital Magnets and Correlated States in Magic-Angle Bilayer Graphene". In: *Nature* 574.7780 (Oct. 2019), pp. 653–657. ISSN: 1476-4687. DOI: 10.1038/s41586-019-1695-0.

[35] Yonglong Xie et al. "Spectroscopic Signatures of Many-Body Correlations in Magic-Angle Twisted Bilayer Graphene". In: *Nature* 572.7767 (Aug. 2019), pp. 101–105. ISSN: 1476-4687. DOI: 10.1038/s41586-019-1422-x.

[36] Petr Stepanov et al. "Untying the Insulating and Superconducting Orders in Magic-Angle Graphene". In: *Nature* 583.7816 (July 2020), pp. 375–378. ISSN: 1476-4687. DOI: 10.1038/s41586-020-2459-6.

[37] Yu Saito et al. "Independent Superconductors and Correlated Insulators in Twisted Bilayer Graphene". en. In: *Nature Physics* (June 2020), pp. 1–5. ISSN: 1745-2481. DOI: 10.1038/s41567-020-0928-3.

[38] Jian Kang and Oskar Vafek. "Non-Abelian Dirac Node Braiding and near-Degeneracy of Correlated Phases at Odd Integer Filling in Magic-Angle Twisted Bilayer Graphene". In: *Physical Review B* 102.3 (July 2020), p. 035161. DOI: 10.1103/PhysRevB.102.035161.

[39] Nguyen N. T. Nam and Mikito Koshino. "Lattice relaxation and energy band modulation in twisted bilayer graphene". In: *Phys. Rev. B* 96 (7 Aug. 2017), p. 075311. DOI: 10.1103/PhysRevB.96.075311. URL: https://link.aps.org/doi/10.1103/PhysRevB.96.075311.

[40] Stephen Carr et al. "Exact continuum model for low-energy electronic states of twisted bilayer graphene". In: *Phys. Rev. Research* 1 (1 Aug. 2019), p. 013001. DOI: 10.1103/PhysRevResearch.1.013001. URL: https://link.aps.org/doi/10.1103/PhysRevResearch.1.013001.

[41] Zhida Song et al. "All Magic Angles in Twisted Bilayer Graphene are Topological". In: *Phys. Rev. Lett.* 123 (3 July 2019), p. 036401. DOI: 10.1103/PhysRevLett.123.036401. URL: https://link.aps.org/doi/10.1103/PhysRevLett.123.036401.

[42] Ming Xie and A. H. MacDonald. "Nature of the Correlated Insulator States in Twisted Bilayer Graphene". In: *Physical Review Letters* 124.9 (Mar. 2020), p. 097601. DOI: 10.1103/PhysRevLett.124.097601.

[43] Cécile Repellin et al. "Ferromagnetism in Narrow Bands of Moir\'e Superlattices". In: *Physical Review Letters* 124.18 (May 2020), p. 187601. ISSN: 0031-9007, 1079-7114. DOI: 10.1103/PhysRevLett.124.187601. arXiv: 1907.11723.

[44] Hoi Chun Po et al. "Origin of Mott Insulating Behavior and Superconductivity in Twisted Bilayer Graphene". In: *Phys. Rev. X* 8 (3 Sept. 2018), p. 031089. DOI: 10.1103/PhysRevX.8.031089. URL: https://link.aps.org/doi/10.1103/PhysRevX.8.031089.

[45] Hoi Chun Po et al. "Faithful tight-binding models and fragile topology of magic-angle bilayer graphene". In: *Physical Review B* 99.19 (May 2019). ISSN: 2469-9969. DOI: 10.1103/physrevb.99.195455. URL: http://dx.doi.org/10.1103/PhysRevB.99.195455.

[46] Liujun Zou et al. "Band structure of twisted bilayer graphene: Emergent symmetries, commensurate approximants, and Wannier obstructions". In: *Phys. Rev. B* 98 (8 Aug. 2018), p. 085435. DOI: 10.1103/PhysRevB.98.085435. URL: https://link.aps.org/doi/10.1103/PhysRevB.98.085435.

[47] Kasra Hejazi et al. "Multiple topological transitions in twisted bilayer graphene near the first magic angle". In: *Phys. Rev. B* 99 (3 Jan. 2019), p. 035111. DOI: 10.1103/PhysRevB.99.035111. URL: https://link.aps.org/doi/10.1103/PhysRevB.99.035111.

[48] Jianpeng Liu, Junwei Liu, and Xi Dai. "Pseudo Landau level representation of twisted bilayer graphene: Band topology and implications on the correlated insulating phase". In: *Phys. Rev. B* 99 (15 Apr. 2019), p. 155415. DOI: 10.1103/PhysRevB.99.155415. URL: https://link.aps.org/doi/10.1103/PhysRevB.99.155415.

[49] Junyeong Ahn, Sungjoon Park, and Bohm-Jung Yang. "Failure of Nielsen-Ninomiya Theorem and Fragile Topology in Two-Dimensional Systems with Space-Time Inversion Symmetry: Application to Twisted Bilayer Graphene at Magic Angle". In: *Physical Review X* 9.2 (Apr. 2019), p. 021013. DOI: 10.1103/PhysRevX.9.021013.

[50] Alexey A. Soluyanov and David Vanderbilt. "Wannier representation of $\mathbb{Z}_2$ topological insulators". In: *Phys. Rev. B* 83 (3 Jan. 2011), p. 035108. DOI: 10.1103/PhysRevB.83.035108. URL: https://link.aps.org/doi/10.1103/PhysRevB.83.035108.

[51] Jian Kang and Oskar Vafek. "Symmetry, Maximally Localized Wannier States, and a Low-Energy Model for Twisted Bilayer Graphene Narrow Bands". In: *Phys. Rev. X* 8 (3 Sept. 2018), p. 031088. DOI: 10.1103/PhysRevX.8.031088. URL: https://link.aps.org/doi/10.1103/PhysRevX.8.031088.

[52] Mikito Koshino et al. "Maximally Localized Wannier Orbitals and the Extended Hubbard Model for Twisted Bilayer Graphene". In: *Phys. Rev. X* 8 (3 Sept. 2018), p. 031087. DOI: 10.1103/PhysRevX.8.031087. URL: https://link.aps.org/doi/10.1103/PhysRevX.8.031087.

[53] Jian Kang and Oskar Vafek. "Strong Coupling Phases of Partially Filled Twisted Bilayer Graphene Narrow Bands". In: *Phys. Rev. Lett.* 122 (24 June 2019), p. 246401. DOI: 10.1103/PhysRevLett.122.246401. URL: https://link.aps.org/doi/10.1103/PhysRevLett.122.246401.

[54] Xiaoyu Wang and Oskar Vafek. "Diagnosis of explicit symmetry breaking in the tight-binding constructions for symmetry-protected topological systems". In: *Phys. Rev. B* 102 (7 Aug. 2020), p. 075142. DOI: 10.1103/PhysRevB.102.075142. URL: https://link.aps.org/doi/10.1103/PhysRevB.102.075142.

[55] Nick Bultinck, Shubhayu Chatterjee, and Michael P. Zaletel. "A Mechanism for Anomalous Hall Ferromagnetism in Twisted Bilayer Graphene". In: *Physical Review Letters* 124.16 (Apr. 2020), p. 166601. ISSN: 0031-9007, 1079-7114. DOI: 10.1103/PhysRevLett.124.166601. arXiv: 1901.08110.

[56] Kasra Hejazi, Xiao Chen, and Leon Balents. "Hybrid Wannier Chern bands in magic angle twisted bilayer graphene and the quantized anomalous Hall effect". In: *Phys. Rev. Res.* 3 (1 Mar. 2021), p. 013242. DOI: 10.1103/PhysRevResearch.3.013242. URL: https://link.aps.org/doi/10.1103/PhysRevResearch.3.013242.

[57] Yves H. Kwan et al. "Domain wall competition in the Chern insulating regime of twisted bilayer graphene". In: *Phys. Rev. B* 104 (11 Sept. 2021), p. 115404. DOI: 10.1103/PhysRevB.104.115404. URL: https://link.aps.org/doi/10.1103/PhysRevB.104.115404.

[58] Johannes Motruk et al. "Density Matrix Renormalization Group on a Cylinder in Mixed Real and Momentum Space". In: *Physical Review B* 93.15 (Apr. 2016), p. 155139. ISSN: 2469-9950, 2469-9969. DOI: 10.1103/PhysRevB.93.155139. arXiv: 1512.03318.

[59] Michael P. Zaletel et al. "Infinite density matrix renormalization group for multicomponent quantum Hall systems". In: *Phys. Rev. B* 91 (4 Jan. 2015), p. 045115. DOI: 10.1103/PhysRevB.91.045115. URL: https://link.aps.org/doi/10.1103/PhysRevB.91.045115.

[60] Garnet Kin-Lic Chan et al. "Matrix product operators, matrix product states, and ab initio density matrix renormalization group algorithms". In: *The Journal of Chemical Physics* 145.1 (2016), p. 014102. DOI: 10.1063/1.4955108. URL: https://doi.org/10.1063/1.4955108.

[61] Daniel E. Parker, Xiangyu Cao, and Michael P. Zaletel. "Local matrix product operators: Canonical form, compression, and control theory". In: *Phys. Rev. B* 102 (3 July 2020), p. 035147. DOI: 10.1103/PhysRevB.102.035147. URL: https://link.aps.org/doi/10.1103/PhysRevB.102.035147.

[62] Shang Liu et al. "Nematic topological semimetal and insulator in magic-angle bilayer graphene at charge neutrality". In: *Phys. Rev. Research* 3 (1 Jan. 2021), p. 013033. DOI: 10.1103/PhysRevResearch.3.013033. URL: https://link.aps.org/doi/10.1103/PhysRevResearch.3.013033.

[63] Yves H. Kwan et al. "Exciton Band Topology in Spontaneous Quantum Anomalous Hall Insulators: Applications to Twisted Bilayer Graphene". In: *Phys. Rev. Lett.* 126 (13 Mar. 2021), p. 137601. DOI: 10.1103/PhysRevLett.126.137601. URL: https://link.aps.org/doi/10.1103/PhysRevLett.126.137601.

[64] Tommaso Cea and Francisco Guinea. "Band Structure and Insulating States Driven by Coulomb Interaction in Twisted Bilayer Graphene". In: *Physical Review B* 102.4 (July 2020), p. 045107. DOI: 10.1103/PhysRevB.102.045107.

[65] Xiao-Liang Qi. "Generic Wave-Function Description of Fractional Quantum Anomalous Hall States and Fractional Topological Insulators". In: *Physical Review Letters* 107.12 (Sept. 2011), p. 126803. DOI: 10.1103/PhysRevLett.107.126803.

[66] G Ehlers, SR White, and RM Noack. "Hybrid-space density matrix renormalization group study of the doped two-dimensional Hubbard model". In: *Physical Review B* 95.12 (2017), p. 125125.

[67] Nicola Marzari and David Vanderbilt. "Maximally Localized Generalized Wannier Functions for Composite Energy Bands". In: *Physical Review B* 56.20 (Nov. 1997), pp. 12847–12865. DOI: 10.1103/PhysRevB.56.12847.

[68] R. D. King-Smith and David Vanderbilt. "Theory of Polarization of Crystalline Solids". In: *Physical Review B* 47.3 (Jan. 1993), pp. 1651–1654. DOI: 10.1103/PhysRevB.47.1651.

[69] R. Resta. "Macroscopic Electric Polarization as a Geometric Quantum Phase". en. In: *Europhysics Letters (EPL)* 22.2 (Apr. 1993), pp. 133–138. ISSN: 0295-5075. DOI: 10.1209/0295-5075/22/2/010.

[70] David Vanderbilt and R. D. King-Smith. "Electric Polarization as a Bulk Quantity and Its Relation to Surface Charge". In: *Physical Review B* 48.7 (Aug. 1993), pp. 4442–4455. DOI: 10.1103/PhysRevB.48.4442.

[71] Nicola Marzari et al. "Maximally Localized Wannier Functions: Theory and Applications". In: *Reviews of Modern Physics* 84.4 (Oct. 2012), pp. 1419–1475. ISSN: 0034-6861, 1539-0756. DOI: 10.1103/RevModPhys.84.1419. arXiv: 1112.5411.

[72] Bogdan Pirvu et al. "Matrix product operator representations". In: *New Journal of Physics* 12.2 (2010), p. 025012.

[73] Matthew Fishman, Steven R. White, and E. Miles Stoudenmire. "The ITensor Software Library for Tensor Network Calculations". In: *SciPost Phys. Codebases* (2022), p. 4. DOI: 10.21468/SciPostPhysCodeb.4. URL: https://scipost.org/10.21468/SciPostPhysCodeb.4.

[74] Johannes Hauschild and Frank Pollmann. "Efficient numerical simulations with Tensor Networks: Tensor Network Python (TeNPy)". In: *SciPost Phys. Lect. Notes* (2018), p. 5. DOI: 10.21468/SciPostPhysLectNotes.5. arXiv: 1805.00055. URL: https://scipost.org/10.21468/SciPostPhysLectNotes.5.

[75] Ya-Hui Zhang, Dan Mao, and T. Senthil. "Twisted bilayer graphene aligned with hexagonal boron nitride: Anomalous Hall effect and a lattice model". In: *Phys. Rev. Research* 1 (3 Nov. 2019), p. 033126. DOI: 10.1103/PhysRevResearch.1.033126. URL: https://link.aps.org/doi/10.1103/PhysRevResearch.1.033126.

[76] Youngkuk Kim et al. "Dirac Line Nodes in Inversion-Symmetric Crystals". In: *Physical Review Letters* 115.3 (July 2015), p. 036806. DOI: 10.1103/PhysRevLett.115.036806.

[77] Ganesh Sundaram and Qian Niu. "Wave-packet dynamics in slowly perturbed crystals: Gradient corrections and Berry-phase effects". In: *Phys. Rev. B* 59 (23 June 1999), pp. 14915–14925. DOI: 10.1103/PhysRevB.59.14915. URL: https://link.aps.org/doi/10.1103/PhysRevB.59.14915.

[78] Jeong Min Park et al. "Flavour Hund's Coupling, Chern Gaps and Charge Diffusivity in Moiré Graphene". In: *Nature* 592.7852 (Apr. 2021), pp. 43–48. ISSN: 1476-4687. DOI: 10.1038/s41586-021-03366-w. (Visited on 10/28/2022).

[79] B. Hunt et al. "Massive Dirac Fermions and Hofstadter Butterfly in a van der Waals Heterostructure". In: *Science* 340 (June 2013), pp. 1427–1430. DOI: 10.1126/science.1237240. arXiv: 1303.6942 [cond-mat.mes-hall].

[80] F. Amet et al. "Insulating Behavior at the Neutrality Point in Single-Layer Graphene". In: *Phys. Rev. Lett.* 110, 216601 (May 2013), p. 216601. DOI: 10.1103/PhysRevLett.110.216601. arXiv: 1209.6364 [cond-mat.mes-hall].

[81] A. A. Zibrov et al. "Even-denominator fractional quantum Hall states at an isospin transition in monolayer graphene". In: *Nature Physics* 14 (July 2018), pp. 930–935. DOI: 10.1038/s41567-018-0190-0. arXiv: 1712.01968 [cond-mat.str-el].

[82] Jeil Jung et al. "Origin of band gaps in graphene on hexagonal boron nitride". In: *Nature Communications* 6 (Feb. 2015), 6308 EP -. URL: https://doi.org/10.1038/ncomms7308.

[83] Matthew Yankowitz et al. "Dynamic band-structure tuning of graphene moiré superlattices with pressure". In: *Nature* 557 (May 2018), pp. 404–408. DOI: 10.1038/s41586-018-0107-1. arXiv: 1707.09054 [cond-mat.mes-hall].

[84] Hakseong Kim et al. "Accurate Gap Determination in Monolayer and Bilayer Graphene/h-BN Moiré Superlattices". In: *Nano Letters* 18 (Dec. 2018), pp. 7732–7741. DOI: 10.1021/acs.nanolett.8b03423. arXiv: 1808.06633 [cond-mat.mes-hall].

[85] E. Suárez Morell et al. "Flat bands in slightly twisted bilayer graphene: Tight-binding calculations". In: *Phys. Rev. B* 82 (12 Sept. 2010), p. 121407. DOI: 10.1103/PhysRevB.82.121407. URL: https://link.aps.org/doi/10.1103/PhysRevB.82.121407.

[86] J. M. B. Lopes dos Santos, N. M. R. Peres, and A. H. Castro Neto. "Continuum model of the twisted graphene bilayer". In: *Phys. Rev. B* 86 (15 Oct. 2012), p. 155449. DOI: 10.1103/PhysRevB.86.155449. URL: https://link.aps.org/doi/10.1103/PhysRevB.86.155449.

[87] A. Uri et al. "Mapping the twist-angle disorder and Landau levels in magic-angle graphene". In: *Nature* 581.7806 (2020), pp. 47–52. DOI: 10.1038/s41586-020-2255-3. URL: https://doi.org/10.1038/s41586-020-2255-3.

[88] Justin H. Wilson et al. "Disorder in twisted bilayer graphene". In: *Phys. Rev. Research* 2 (2 June 2020), p. 023325. DOI: 10.1103/PhysRevResearch.2.023325. URL: https://link.aps.org/doi/10.1103/PhysRevResearch.2.023325.

[89] Bikash Padhi et al. "Transport across twist angle domains in moiré graphene". In: *Phys. Rev. Research* 2 (3 Sept. 2020), p. 033458. DOI: 10.1103/PhysRevResearch.2.033458. URL: https://link.aps.org/doi/10.1103/PhysRevResearch.2.033458.

[90] Ya-Hui Zhang, Hoi Chun Po, and T. Senthil. "Landau level degeneracy in twisted bilayer graphene: Role of symmetry breaking". In: *Phys. Rev. B* 100 (12 Sept. 2019), p. 125104. DOI: 10.1103/PhysRevB.100.125104. URL: https://link.aps.org/doi/10.1103/PhysRevB.100.125104.

[91] Zhen Bi, Noah F. Q. Yuan, and Liang Fu. "Designing Flat Bands by Strain". In: *Physical Review B* 100.3 (July 2019), p. 035448. DOI: 10.1103/PhysRevB.100.035448.

[92] Youngjoon Choi et al. "Tracing out Correlated Chern Insulators in Magic Angle Twisted Bilayer Graphene". In: *arXiv e-prints* (Aug. 2020), p. 2008.11746.

[93] Loïc Huder et al. "Electronic Spectrum of Twisted Graphene Layers under Heterostrain". In: *Phys. Rev. Lett.* 120 (15 Apr. 2018), p. 156405. DOI: 10.1103/PhysRevLett.120.156405. URL: https://link.aps.org/doi/10.1103/PhysRevLett.120.156405.

[94] Hidekatsu Suzuura and Tsuneya Ando. "Phonons and electron-phonon scattering in carbon nanotubes". In: *Phys. Rev. B* 65 (23 May 2002), p. 235412. DOI: 10.1103/PhysRevB.65.235412. URL: https://link.aps.org/doi/10.1103/PhysRevB.65.235412.

[95] Ken-ichi Sasaki and Riichiro Saito. "Pseudospin and Deformation-Induced Gauge Field in Graphene". In: *Progress of Theoretical Physics Supplement* 176 (June 2008), pp. 253–278. ISSN: 0375-9687. DOI: 10.1143/PTPS.176.253. URL: https://doi.org/10.1143/PTPS.176.253.

[96] In: *See Supplemental Material at [URL to be inserted by publisher] for a discussion of the connection between the BM ground state and the self-consistent SM at charge neutrality, for HF results at $\nu = -2$, and for additional details of the DMRG simulations* ().

[97] Yi Zhang et al. "Correlated Insulating Phases of Twisted Bilayer Graphene at Commensurate Filling Fractions: A Hartree-Fock Study". In: *Physical Review B* 102.3 (July 2020), p. 035136. DOI: 10.1103/PhysRevB.102.035136.

[98] P. C. Hohenberg. "Existence of Long-Range Order in One and Two Dimensions". In: *Phys. Rev.* 158 (2 June 1967), pp. 383–386. DOI: 10.1103/PhysRev.158.383. URL: https://link.aps.org/doi/10.1103/PhysRev.158.383.

[99] N. D. Mermin and H. Wagner. "Absence of Ferromagnetism or Antiferromagnetism in One- or Two-Dimensional Isotropic Heisenberg Models". In: *Phys. Rev. Lett.* 17 (22 Nov. 1966), pp. 1133–1136. DOI: 10.1103/PhysRevLett.17.1133. URL: https://link.aps.org/doi/10.1103/PhysRevLett.17.1133.

[100] Shubhayu Chatterjee, Matteo Ippoliti, and Michael P. Zaletel. "Skyrmion superconductivity: DMRG evidence for a topological route to superconductivity". In: *Phys. Rev. B* 106 (3 July 2022), p. 035421. DOI: 10.1103/PhysRevB.106.035421. URL: https://link.aps.org/doi/10.1103/PhysRevB.106.035421.

[101] Frank Pollmann et al. "Theory of Finite-Entanglement Scaling at One-Dimensional Quantum Critical Points". In: *Phys. Rev. Lett.* 102 (25 June 2009), p. 255701. DOI: 10.1103/PhysRevLett.102.255701. URL: https://link.aps.org/doi/10.1103/PhysRevLett.102.255701.

[102] L. Tagliacozzo et al. "Scaling of entanglement support for matrix product states". In: *Phys. Rev. B* 78 (2 July 2008), p. 024410. DOI: 10.1103/PhysRevB.78.024410. URL: https://link.aps.org/doi/10.1103/PhysRevB.78.024410.

[103] Jonas A. Kjäll et al. "Phase diagram of the anisotropic spin-2 XXZ model: Infinite-system density matrix renormalization group study". In: *Phys. Rev. B* 87 (23 June 2013), p. 235106. DOI: 10.1103/PhysRevB.87.235106. URL: https://link.aps.org/doi/10.1103/PhysRevB.87.235106.

[104] Eric Brillaux et al. "Analytical renormalization group approach to competing orders at charge neutrality in twisted bilayer graphene". In: *Phys. Rev. Res.* 4 (3 Aug. 2022), p. 033168. DOI: 10.1103/PhysRevResearch.4.033168. URL: https://link.aps.org/doi/10.1103/PhysRevResearch.4.033168.

[105] Héctor Ochoa. "Strain-induced excitonic instability in twisted bilayer graphene". In: *Phys. Rev. B* 102 (20 Nov. 2020), p. 201107. DOI: 10.1103/PhysRevB.102.201107. URL: https://link.aps.org/doi/10.1103/PhysRevB.102.201107.

[106] Rafael M. Fernandes and Jörn W. F. Venderbos. "Nematicity with a twist: Rotational symmetry breaking in a moiré superlattice". In: *Science Advances* 6.32 (2020). DOI: 10.1126/sciadv.aba8834.

[107] Yuxuan Wang, Jian Kang, and Rafael M. Fernandes. "Topological and nematic superconductivity mediated by ferro-SU(4) fluctuations in twisted bilayer graphene". In: *Phys. Rev. B* 103 (2 Jan. 2021), p. 024506. DOI: 10.1103/PhysRevB.103.024506. URL: https://link.aps.org/doi/10.1103/PhysRevB.103.024506.

[108] Dmitry V. Chichinadze, Laura Classen, and Andrey V. Chubukov. "Nematic superconductivity in twisted bilayer graphene". In: *Phys. Rev. B* 101 (22 June 2020), p. 224513. DOI: 10.1103/PhysRevB.101.224513. URL: https://link.aps.org/doi/10.1103/PhysRevB.101.224513.

[109] Vladyslav Kozii et al. "Nematic superconductivity stabilized by density wave fluctuations: Possible application to twisted bilayer graphene". In: *Phys. Rev. B* 99 (14 Apr. 2019), p. 144507. DOI: 10.1103/PhysRevB.99.144507. URL: https://link.aps.org/doi/10.1103/PhysRevB.99.144507.

[110] Ming Xie and A. H. MacDonald. "Weak-Field Hall Resistivity and Spin-Valley Flavor Symmetry Breaking in Magic-Angle Twisted Bilayer Graphene". In: *Phys. Rev. Lett.* 127 (19 Nov. 2021), p. 196401. DOI: 10.1103/PhysRevLett.127.196401. URL: https://link.aps.org/doi/10.1103/PhysRevLett.127.196401.

[111] Oskar Vafek and Jian Kang. "Renormalization Group Study of Hidden Symmetry in Twisted Bilayer Graphene with Coulomb Interactions". In: *Phys. Rev. Lett.* 125 (25 Dec. 2020), p. 257602. DOI: 10.1103/PhysRevLett.125.257602. URL: https://link.aps.org/doi/10.1103/PhysRevLett.125.257602.

[112] Youngjoon Choi et al. "Correlation-Driven Topological Phases in Magic-Angle Twisted Bilayer Graphene". In: *Nature* 589.7843 (Jan. 2021), pp. 536–541. ISSN: 1476-4687. DOI: 10.1038/s41586-020-03159-7.

[113] Johannes S. Hofmann et al. "Fermionic Monte Carlo Study of a Realistic Model of Twisted Bilayer Graphene". In: *Phys. Rev. X* 12 (1 Mar. 2022), p. 011061. DOI: 10.1103/PhysRevX.12.011061. URL: https://link.aps.org/doi/10.1103/PhysRevX.12.011061.

[114] Gaopei Pan et al. "Dynamical properties of collective excitations in twisted bilayer graphene". In: *Phys. Rev. B* 105 (12 Mar. 2022), p. L121110. DOI: 10.1103/PhysRevB.105.L121110. URL: https://link.aps.org/doi/10.1103/PhysRevB.105.L121110.

[115] Xiaomeng Liu et al. "Visualizing broken symmetry and topological defects in a quantum Hall ferromagnet". In: *Science* 375.6578 (2022), pp. 321–326. DOI: 10.1126/science.abm3770. URL: https://www.science.org/doi/abs/10.1126/science.abm3770.

[116] Jianpeng Liu and Xi Dai. "Theories for the Correlated Insulating States and Quantum Anomalous Hall Effect Phenomena in Twisted Bilayer Graphene". In: *Physical Review B* 103.3 (Jan. 2021), p. 035427. DOI: 10.1103/PhysRevB.103.035427.

[117] Fang Xie et al. "Twisted Bilayer Graphene. VI. An Exact Diagonalization Study at Nonzero Integer Filling". In: *Physical Review B* 103.20 (May 2021), p. 205416. DOI: 10.1103/PhysRevB.103.205416.

[118] Jihang Zhu, Jung-Jung Su, and A. H. MacDonald. "Voltage-Controlled Magnetic Reversal in Orbital Chern Insulators". In: *Physical Review Letters* 125.22 (Nov. 2020), p. 227702. DOI: 10.1103/PhysRevLett.125.227702.

[119] Eslam Khalaf et al. "Magic Angle Hierarchy in Twisted Graphene Multilayers". In: *Physical Review B* 100.8 (Aug. 2019), p. 085109. ISSN: 2469-9950, 2469-9969. DOI: 10.1103/PhysRevB.100.085109. arXiv: 1901.10485.

[120] Yuan Cao et al. "Pauli-limit violation and re-entrant superconductivity in moiré graphene". In: *Nature* 595.7868 (2021), pp. 526–531. DOI: 10.1038/s41586-021-03685-y. URL: https://doi.org/10.1038/s41586-021-03685-y.

[121] Zeyu Hao et al. "Electric Field–Tunable Superconductivity in Alternating-Twist Magic-Angle Trilayer Graphene". In: *Science* 371.6534 (Mar. 2021), pp. 1133–1138. DOI: 10.1126/science.abg0399.

[122] Simon Turkel et al. "Orderly disorder in magic-angle twisted trilayer graphene". In: *Science* 376.6589 (2022), pp. 193–199. DOI: 10.1126/science.abk1895. URL: https://www.science.org/doi/abs/10.1126/science.abk1895.

[123] Hyunjin Kim et al. "Spectroscopic Signatures of Strong Correlations and Unconventional Superconductivity in Twisted Trilayer Graphene". In: *arXiv:2109.12127 [cond-mat]* (Sept. 2021). arXiv: 2109.12127 [cond-mat].

[124] E. H. Hwang and S. Das Sarma. "Dielectric function, screening, and plasmons in two-dimensional graphene". In: *Phys. Rev. B* 75 (20 May 2007), p. 205418. DOI: 10.1103/PhysRevB.75.205418. URL: https://link.aps.org/doi/10.1103/PhysRevB.75.205418.

[125] Shoudan Liang and Hanbin Pang. "Approximate diagonalization using the density matrix renormalization-group method: A two-dimensional-systems perspective". In: *Physical Review B* 49.13 (1994), p. 9214.

[126] Ulrich Schollwöck. "The density-matrix renormalization group in the age of matrix product states". In: *Annals of physics* 326.1 (2011), pp. 96–192.

[127] Gregory M. Crosswhite and Dave Bacon. "Finite automata for caching in matrix product algorithms". In: *Phys. Rev. A* 78.1 (July 2008), p. 012356. ISSN: 1050-2947. DOI: 10.1103/PhysRevA.78.012356. arXiv: 0708.1221. URL: http://arxiv.org/abs/0708.1221%20http://dx.doi.org/10.1103/PhysRevA.78.012356%20https://link.aps.org/doi/10.1103/PhysRevA.78.012356.

[128] G Rickayzen. *Green's Functions and Condensed Matter*. Materials Science Series. Academic Press, 1980. ISBN: 9780125879507. URL: https://books.google.com/books?id=cZnvAAAAMAAJ.

[129] A V Oppenheim et al. *Discrete-time Signal Processing*. Prentice Hall international editions. Prentice Hall, 1999. ISBN: 9780137549207. URL: https://books.google.com/books?id=Bv1SAAAAMAAJ.

[130] Alex Thomson et al. "Gate-defined wires in twisted bilayer graphene: From electrical detection of intervalley coherence to internally engineered Majorana modes". In: *Phys. Rev. B* 105 (8 Feb. 2022), p. L081405. DOI: 10.1103/PhysRevB.105.L081405. URL: https://link.aps.org/doi/10.1103/PhysRevB.105.L081405.

[131] Shubhayu Chatterjee, Nick Bultinck, and Michael P. Zaletel. "Symmetry Breaking and Skyrmionic Transport in Twisted Bilayer Graphene". In: *Physical Review B* 101.16 (Apr. 2020), p. 165141. DOI: 10.1103/PhysRevB.101.165141.

Appendix A

Appenix for chapter 2

A.1 Interacting Bistritzer-MacDonald Model

In this appendix, we review the interacting BM model projected into the flat bands. We use the conventions and definition of $\mathbf{h}(\mathbf{k})$ from Supp. Mat. I of [8].

Let us first consider the Coulomb interaction

$$\begin{aligned}\hat{H}_C &= \frac{1}{2}\int \mathrm{d}\mathbf{r}\int \mathrm{d}\mathbf{r}'\, V(\mathbf{r}-\mathbf{r}')\psi^\dagger_\alpha(\mathbf{r})\psi^\dagger_\beta(\mathbf{r}')\psi_\beta(\mathbf{r}')\psi_\alpha(\mathbf{r}) \\ &= \frac{1}{2A}\sum_{\mathbf{k},\mathbf{k}',\mathbf{q}} V_{\mathbf{q}}\,\psi^\dagger_{\alpha,\mathbf{k}+\mathbf{q}}\psi^\dagger_{\beta,\mathbf{k}'-\mathbf{q}}\psi_{\beta,\mathbf{k}'}\psi_{\alpha,\mathbf{k}}\,, \end{aligned} \tag{A.1}$$

where A is the sample area, $V_{\mathbf{q}} = \int \mathrm{d}\mathbf{r}\, V(\mathbf{r})e^{i\mathbf{q}\cdot\mathbf{r}}$ and α,β are combined layer-sublattice indices. Summation over repeated indices is implicit. The Fourier components of the Fermi operators are defined to satisfy the canonical anti-commutation relations:

$$\{\psi^\dagger_{\alpha,\mathbf{k}},\psi_{\beta,\mathbf{k}'}\} = \delta_{\alpha,\beta}\delta_{\mathbf{k},\mathbf{k}'} \tag{A.2}$$

Next, we relabel the sums over the momenta $\mathbf{k}$ and $\mathbf{k}'$ as

$$\sum_{\mathbf{k}} \to \sum_{\mathbf{k}\in\mathrm{mBZ}}\sum_{\tau}\sum_{\mathbf{G}}, \tag{A.3}$$

where $\tau = \pm$ is a valley label, and $\mathbf{G}$ are the moiré reciprocal lattice vectors. We can now approximate the Coulomb interaction as

$$\begin{aligned}\hat{H}_C &= \frac{1}{2A}\sum_{\tau,\tau'}\sum_{\mathbf{q}}\sum_{\mathbf{k},\mathbf{k}'\in\mathrm{mBZ}}\sum_{\mathbf{G},\mathbf{G}'} V_{\mathbf{q}}\times \\ &\quad \psi^\dagger_{\alpha,\tau,\mathbf{G}}(\mathbf{k}+\mathbf{q})\psi^\dagger_{\beta,\tau',\mathbf{G}'}(\mathbf{k}'-\mathbf{q})\psi_{\beta,\tau',\mathbf{G}'}(\mathbf{k}')\psi_{\alpha,\tau,\mathbf{G}}(\mathbf{k})\,, \end{aligned} \tag{A.4}$$

where $\psi^\dagger_{\alpha,\tau,\mathbf{G}}(\mathbf{k}) = \psi^\dagger_{\alpha,\mathbf{k}+\tau\mathbf{K}_\Gamma+\mathbf{G}}$ and $\mathbf{K}_\Gamma$ denotes the Γ point of the mBZ centered at the K points of the graphene layers. Note that by definition, $\psi^\dagger_{\alpha,\tau,\mathbf{G}}(\mathbf{k}+\mathbf{G}') = \psi^\dagger_{\alpha,\tau,\mathbf{G}+\mathbf{G}'}(\mathbf{k})$. Eq. (A.4) is only an approximation to the complete Coulomb interaction, as inter-valley scattering terms have been neglected. This can be justified because of the long-range nature of the interaction, which suppresses inter-valley scattering by a factor of order $V_{2\mathbf{K}_\Gamma}/V_0$.

Next, we perform a unitary transformation to the BM band basis and define

$$f^\dagger_{m,\tau,\mathbf{k}} = \sum_{\alpha,\mathbf{G}} u_{m,\tau;\alpha,\mathbf{G}}(\mathbf{k})\psi^\dagger_{\alpha,\tau,\mathbf{G}}(\mathbf{k})\,, \tag{A.5}$$

where m labels the bands of the single-valley BM model, and $u_{m,\tau;\alpha,\mathbf{G}}(\mathbf{k})$ are the periodic part of the Bloch states of the BM Hamiltonian. Note that $f^\dagger_{m,\tau,\mathbf{k}+\mathbf{G}'} = f^\dagger_{m,\tau,\mathbf{k}}$ because the BM Bloch states satisfy $u_{m,\tau;\alpha,\mathbf{G}}(\mathbf{k}+\mathbf{G}') = u_{m,\tau;\alpha,\mathbf{G}+\mathbf{G}'}(\mathbf{k})$. With this definition, Eq. (A.4) takes the following form in the BM band basis:

$$\begin{aligned}\hat{H}_C &= \frac{1}{2A}\sum_{\tau,\tau'}\sum_{\mathbf{q}}\sum_{\mathbf{k},\mathbf{k}'\in\mathrm{mBZ}} V_{\mathbf{q}}\left[\Lambda^\tau_{\mathbf{q}}(\mathbf{k})\right]_{mn}\left[\Lambda^{\tau'}_{-\mathbf{q}}(\mathbf{k}')\right]_{m'n'} \\ &\quad\times f^\dagger_{m,\tau,\mathbf{k}+\mathbf{q}} f^\dagger_{m',\tau',\mathbf{k}'-\mathbf{q}} f_{n',\tau',\mathbf{k}'} f_{n,\tau,\mathbf{k}}\,,\end{aligned} \tag{A.6}$$

where the sums over band indices are implicit, and the form factors are given by

$$\left[\Lambda^\tau_{\mathbf{q}}(\mathbf{k})\right]_{mn} = \sum_{\alpha,\mathbf{G}} u^*_{m,\tau;\alpha,\mathbf{G}}(\mathbf{k}+\mathbf{q})u_{n,\tau;\alpha,\mathbf{G}}(\mathbf{k})\,. \tag{A.7}$$

In this work, we consider the single-valley model, which means that we fix all valley labels, i.e. $\tau = +$ everywhere. The single-valley Coulomb interaction is then given by

$$\hat{H}_{C,sv} = \frac{1}{2A}\sum_{\mathbf{q},\mathbf{k},\mathbf{k}'} V_{\mathbf{q}} : \left[\mathbf{f}^\dagger_{\mathbf{k}+\mathbf{q}}\Lambda_{\mathbf{q}}(\mathbf{k})\mathbf{f}_{\mathbf{k}}\right]\left[\mathbf{f}^\dagger_{\mathbf{k}'-\mathbf{q}}\Lambda_{-\mathbf{q}}(\mathbf{k}')\mathbf{f}_{\mathbf{k}'}\right] : \tag{A.8}$$

where $\Lambda_{\mathbf{q}}(\mathbf{k}) = \Lambda^+_{\mathbf{q}}(\mathbf{k})$ and $\mathbf{f}^\dagger_{\mathbf{k}} = \mathbf{f}^\dagger_{+,\mathbf{k}}$ is a vector of creation operators running over the BM bands.

As a final step, we now project $\hat{H}_C$ into the subspace where all remote valence bands are occupied, and all remote conduction bands are empty. To do that, we first define following Hartree Hamiltonian functional:

$$\begin{aligned}\hat{H}_h[P(\mathbf{k})] = \frac{V_0}{A}\sum_{\mathbf{G}}&\left[\sum_{\mathbf{k}'}\mathrm{tr}\left(P(\mathbf{k}')\Lambda_{\mathbf{G}}(\mathbf{k}')\right)\right] \\ &\times\sum_{\mathbf{k}}\mathbf{f}^\dagger_{\mathbf{k}}\Lambda_{-\mathbf{G}}(\mathbf{k})\mathbf{f}_{\mathbf{k}}\,,\end{aligned} \tag{A.9}$$

where the fermion operators are restricted to the flat bands, and which depends on a general Slater determinant correlation matrix $\langle f^\dagger_{m,\mathbf{k}} f_{n,\mathbf{k}'}\rangle = \sum_{\mathbf{G}} \delta_{\mathbf{k}+\mathbf{G},\mathbf{k}'} \left[P(\mathbf{k})\right]_{nm}$. We also similarly define a Fock Hamiltonian functional:

$$\hat{H}_f[P(\mathbf{k})] = -\frac{1}{A}\sum_{\mathbf{q},\mathbf{k}} V_{\mathbf{q}}\ \mathbf{f}^\dagger_{\mathbf{k}} \Lambda_{\mathbf{q}}(\mathbf{k}-\mathbf{q}) P(\mathbf{k}-\mathbf{q}) \Lambda_{-\mathbf{q}}(\mathbf{k}) \mathbf{f}_{\mathbf{k}}\,, \tag{A.10}$$

where again the fermion operators are restricted to the flat bands. With these definitions, one can write the flat-band projected Coulomb interaction as

$$\hat{H}_{C,sv}\Big|_{FB} = \tilde{H}_{C,sv} + \hat{H}_h[P_r(\mathbf{k})] + \hat{H}_f[P_r(\mathbf{k})]\,, \tag{A.11}$$

where $\tilde{H}_{C,sv}$ is obtained from $\hat{H}_{C,sv}$ by simply restricting all band indices to the flat bands, and $P_r(\mathbf{k})$ is the correlation matrix of the Slater determinant where only the remote valence bands are filled.

Having obtained the flat-band projected single-valley Coulomb interaction, we now have to be careful not to double count certain interaction effects. In particular, the value of the hopping parameter in the tight-binding model of mono-layer graphene is chosen to best reproduce the experimentally observed Dirac velocity. Importantly, this Dirac velocity is already renormalized by the Coulomb interaction. So if we want to explicitly add back the complete Coulomb interaction, we must make sure not to forget to subtract off the renormalization of the dispersion. In practice, this means that we have to subtract off the following Hartree-Fock Hamiltonian:

$$\hat{H}_{sub} = \hat{H}_h[P_0(\mathbf{k})] + \hat{H}_f[P_0(\mathbf{k})]\,, \tag{A.12}$$

where $P_0(\mathbf{k})$ is the correlation matrix of the charge-neutrality Slater determinant of two *decoupled* graphene layers [42] restricted single spin and valley, expressed in the BM band basis. The complete projected single-valley BM model thus takes the form

$$\hat{H} = \hat{H}_{BM,sv} + \hat{H}_{C,sv}\Big|_{FB} - \hat{H}_{sub}\,. \tag{A.13}$$

Because the inter-layer tunneling is only a small perturbation compared to the intra-layer hopping, it does not significantly change the remote bands. It thus holds to a very good approximation that

$$\left[P_r(\mathbf{k})\right]_{mn} = \left[P_0(\mathbf{k})\right]_{mn} \text{ for } m,n \in \text{remote bands}\,. \tag{A.14}$$

Now combining all the single-particle terms in Eq. (A.13), one obtains the matrix $h(\mathbf{k})$ defined in Eq. (2.1). The remaining interaction Hamiltonian of Eq. (A.13) is then exactly the second term of Eq. (2.1).

Finally, let us also comment on the value of the dielectric constant ϵ_r that we use for the projected model. The dielectric constant of the unprojected model is determined by the

insulating hexagonal Boron-Nitride (hBN) substrate. In particular, it is given by the geometric mean of the dielectric constants of hBN parallel and orthogonal to the atomic plane: $\epsilon_{\text{hBN}} = \sqrt{\epsilon_\perp \epsilon_\parallel} \approx 4.4$. When we restrict to the flat bands we have to take into account that the filled remote bands which have been projected out act as another insulating background, whose polarization will also contribute to the dielectric constant. We phenomologically incorporate this effect by screening the Coulomb potential with the static RPA polarization of eight Dirac cones at neutrality. In doing so, we ignore the small inter-layer tunneling terms (whose effect on the remote bands is expected to be small), and we overcount a small contribution coming from the states in the flat bands themselves. The polarization bubble of Dirac fermions in mono-layer graphene was calculated in Ref. [124]. Using the results from that paper, we obtain a dielectric constant $\epsilon_r = \epsilon_{\text{hBN}} + N_D * 0.73 \approx 10.3$, where $N_D = 8$ is the number of Dirac cones. This gives an order-of-magnitude estimate for the dielectric constant of the projected model. Given the many approximations used in deriving this estimate, it is safest to assume that the true dielectric constant lies somewhere in the interval $\epsilon_r \sim 6 - 12$.

We also note that the effective gate distance d appearing in $V_{\mathbf{q}} = \frac{e^2}{4\pi\epsilon q}\tanh(qd)$ is modified by the anisostropy of the substrate dielectric constant. Specifically, if d_g is the physical distance to the gate, then $d = \sqrt{\frac{\epsilon_\perp}{\epsilon_\parallel}} d_g$, due to the bending of field lines in an anisotropic substrate.

A.2 Wannier Localization, Gauge fixing, and Symmetrization

In this section, we list several invariants enforced by the maximal localization of Wannier orbitals and gauge fixing. We also comment on the different between our gauge choice and the gauge choice in [38], and how we can map states from one gauge to another.

We denote the periodic part of momentum space orbitals $c^\dagger_{\pm,\mathbf{k}}$ by $|u_\pm(k_x, k_y)\rangle$. We define 2×2 overlap matrix as

$$O_{\alpha\beta}(\mathbf{k}, \mathbf{k}') = \langle u_\alpha(\mathbf{k}) | u_\beta(\mathbf{k}')\rangle \,. \tag{A.15}$$

For each overlap matrix O, we define unitary overlap matrix $\tilde{O}$ by the unitary part of the polar decomposition of O. Wannier localization [67] guarantees that the unitary overlap matrix in the k_x direction is always given by

$$\tilde{O}_{\alpha\beta}(\mathbf{k}, \mathbf{k} + \Delta k_x) = \delta_{\alpha\beta} e^{iP_x(\alpha, k_y)}, \tag{A.16}$$

where Δk_x is the unit of discretization in the x direction. Physically, this corresponds to choosing constant $A_x = P_x/G_x$.

Wannier localization fixes relative phases within each k_y mode. To fix relative phases between different k_y modes, we demand a continuity criterion in the k_y direction. One natural choice is to demand the unitary overlap matrix in the y direction be the identity

matrix:

$$\tilde{O}_{\alpha\beta}(\mathbf{k}, \mathbf{k} + \Delta k_y) = \delta_{\alpha\beta}, \tag{A.17}$$

where the x component of $\mathbf{k}$ is some fixed k_{x0}. The condition notably does *not* wraparound the mBZ: the mode near $k_y/G_y = 0.5$ and the mode near $k_y/G_y = -0.5$ are not subject to the continuity condition with each other.

This leaves us with a global $U(1) \times U(1)$ phase ambiguity. Fortunately, the Wannier localization and continuity conditions are compatible with the symmetry requirements

$$\begin{aligned} C_2\mathcal{T} \left|u_{\pm}(\mathbf{k})\right\rangle &= \left|u_{\mp}(\mathbf{k})\right\rangle, \\ C_{2x} \left|u_{\pm}(\mathbf{k})\right\rangle &= \mp i \left|u_{\mp}(-\mathbf{k})\right\rangle, \end{aligned} \tag{A.18}$$

which fixes the gauge up to an overall minus sign.

We note that the gauge fixing condition is different from [38] on two accounts: we use a different continuity criterion, and we fix C_{2x} to act as σ_y rather than σ_x. The latter is easy to account for by a $e^{i\pi\sigma_x/4}$ rotation, which maps σ_y to σ_x, but there is no guarantee that the gauge is the same even after such rotation.

Luckily, in the case of $L_y = 6, \Phi_y = \pi, w_0 = 0.185$, $e^{i\pi\sigma_x/4}$ rotation maps our ground state ansatz in Sec. 17 to their ground state ansatz, suggesting our gauge choice is the same up to the rotation. In particular, this means we can go from their parametrization to our parametrization simply by changing $\varphi \to \varphi + \pi/2$. We make use of this fact when we write down the Stripe ansatz in our gauge.

A.3 An Uncompressed MPO for BLG

This Appendix details the construction of the uncompressed infinite MPO for bilayer graphene. More concretely, we show how to construct an iMPO which encodes arbitrary 4-fermion interactions up to range R. [1] Schematically, what is the iMPO for the Hamiltonian

$$\widehat{H} = \sum_{ij} t_{ij} c_i^\dagger c_j + \sum V_{ijk\ell} c_i^\dagger c_j^\dagger c_k c_\ell, \tag{A.19}$$

for arbitrary interactions t and V?

We proceed in several stages. First we provide a straightforward construction of such an MPO of size $D = O(R^3)$. However, this gives an iMPO which is too large to even begin compressing ($D \approx 8,000,000$ for our standard Hamiltonian parameters). Second, therefore, we provide a more efficient MPO which represents the same operator at size $D = O(R^2)$, which will give $D \approx 100,000$ — small enough to be compressed.

[1] For the construction of *finite* MPO for interacting fermions, as is relevant to quantum chemistry applications, we refer the reader to [60].

A Straightforward MPO Construction

This section will give a relatively straightforward way to construct an MPO for a long-range 4-fermion Hamiltonian. For simplicity, we restrict ourselves to a 1D spin chain of spinless fermions and no internal degrees of freedom and construct a iMPO representation for a class of "toy" 4-body Hamiltonians

$$\widehat{H}_{\text{simple}} = \sum_{i<j<k<\ell} V_{ijk\ell} c_i^\dagger c_j^\dagger c_k c_\ell \tag{A.20}$$

with $|i-j|, |j-k|, |k-\ell| \leq R$. [2] In particular, we have imposed the artificial properties that H contains only terms of the form $c^\dagger c^\dagger cc$ (which makes this non-Hermitian), is completely translationally invariant, and has $i < j < k < \ell$ with strict inequalities. These restrictions will be lifted below.

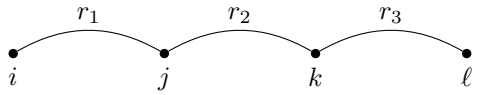

Let us work in the finite state machine picture for the iMPO. For convenience, define $r_1 = j - i$, $r_2 = k - j$, $r_3 = \ell - k$. As $0 < r_1, r_2, r_3 \leq R$, our operator can have up to R^3 terms. For each one, we must first place a $c^\dagger$, then place $r_1 - 1$ identity operators $\widehat{\mathbb{1}}$, then place another $c^\dagger$, and so on. To encode these into the finite state machine, we make a unique path for each term from the initial to final nodes, as shown in Fig. A.1. For each term in

[2] This is slightly different from how we implemented Δx cutoff for BLG, where we demanded $\ell - i < R$. This will only change the complexity by a constant factor, so we stick to the simpler cutoff

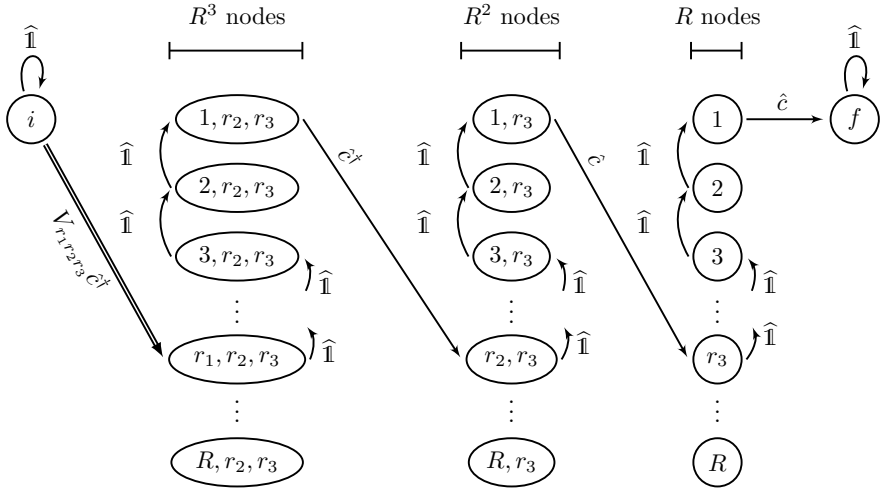

Figure A.1: A straightforward but rather inefficient MPO for $\widehat{H}_{\text{simple}}$.

the Hamiltonian, there is an edge $V_{r_1 r_2 r_3}$ from the initial node (i) to node (r_1, r_2, r_3). After that, there is a unique path from node (r_1, r_2, r_3) to node (f). The nodes are labeled by the distances to non-identity nodes that have yet to be placed. In each column, the path simply "counts down" in the first index, until it reaches 1. At that site a non-identity on-site operator is placed, and the path goes on to the next column. As a matrix, the operation of counting down is encoded by a "skipping matrix", with identities on the first superdiagonal:

$$\widehat{\mathbb{S}} = \begin{pmatrix} 0 & \widehat{\mathbb{1}} & & & \\ & 0 & \widehat{\mathbb{1}} & & \\ & & \ddots & \ddots & \\ & & & 0 & \widehat{\mathbb{1}} \\ & & & & 0 \end{pmatrix}.$$

We therefore adopt a concise diagrammatic notation where *rectangular* nodes represent nodes that count down, as shown in Fig. A.2. In this notation, $\widehat{\mathbb{S}}_i$ acts on a node as[3]

$$\widehat{\mathbb{S}}_i(\widehat{O}[r_i...]) = (\widehat{O}[r_i - 1...]). \tag{A.21}$$

We will use this notation below. We also note that some transitions are deterministic, in the sense that the next node is fully specified by the current node (e.g. $(2, r_2, r_3) \to (1, r_2, r_3)$). On the other hand, the transition from the initial node is highly branching, giving rise to the R^3 different terms in the Hamiltonian. We show such highly branching transitions in the figure by double arrows, while deterministic transitions are shown by single solid arrows.

Overall, this construction requires $C_1(R) := R^3 + R^2 + R + 2$ nodes. This is already somewhat efficient, as multiple terms will partially reuse the same paths. For instance, the paths through the state machine for V_{5,r_2,r_3} and V_{6,r_2,r_3} will be the same after the first few edges. To add other types of terms, such as $cc^\dagger cc^\dagger$ or $ccc^\dagger c^\dagger$, one must duplicate all these nodes, giving $4C_1(R)$ nodes. For bilayer graphene, we use a unit cell of size 12 and interaction cutoff of 10 unit cells, giving $D = 6,970,088$ just for the four-body terms. This makes the $O(D^3)$ compression algorithm impractical, so we must seek a more efficient way to encode the MPO.

An Efficient MPO Construction

We now describe a more efficient way to encode the uncompressed MPO, and give explicit state machines for 2-body, 3-body, and 4-body interaction terms. The key idea is to place the coefficient $V_{r_1 r_2 r_3}$ in the *middle* of the path rather than at the beginning.

Fig. A.2 (Bottom) shows the more efficient construction of the MPO for the same operator as before, Eq. (A.20). Let us unpack how it works. For each term $V_{r_1 r_2 r_3} c^\dagger c^\dagger cc$, we start at node (i), jump to the node $(\hat{c}^\dagger[1])$ by placing $c^\dagger$, then "count up" to r_1, at which point we

[3]This is slight abuse of notation, since it doesn't convey that $\widehat{\mathbb{S}}_i$ places an identity operator upon the transition.

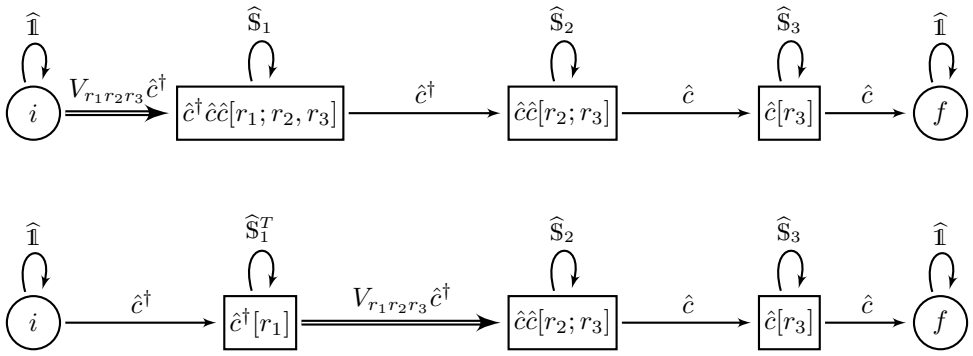

Figure A.2: (Top) Definition of the compact state machine notation. This is the same state machine as in Fig. A.1, but where columns have been replaced by rectangular nodes. Rectangular nodes label the on-site operators that are yet to be placed, as well as the distances to them. The first rectangle contains R^3 nodes, the second contains R^2 and the third contains R. The self-loop $\widehat{\mathbb{S}}$ means one should place an identity $\widehat{\mathbb{1}}$ and decrement the first index of the node. (Bottom) Another MPO which represents the same Hamiltonian with only $D = O(R^2)$ nodes instead of $O(R^3)$. Rectangular nodes to the right of the branching arrow are labeled similarly to the (Top), while the rectangular node to the left of the branching arrow is labeled by which operator it has already picked up, and the distance to it.

place the on-site operator $V_{r_1r_2r_3}c^\dagger$. The state machine then "counts down" for distance r_2, places a c operator, counts down for distance r_3, places a second c, and reaches the final node.

To distinguish "count up" skipping matrix and "count down" skipping matrix, we introduced "transposed skipping matrix" $\widehat{\mathbb{S}}_i^T$ such that

$$\widehat{\mathbb{S}}_i^T(\widehat{O}[r_i...]) = (\widehat{O}[r_i + 1...]). \tag{A.22}$$

The advantage over the previous method is that, instead of having a unique path for each term in the Hamiltonian, many of the paths are partially shared. For example the terms $V_{r_15r_3}$ and $V_{r_17r_3}$ will share the same first r_1 and last r_3 steps in their path through the state machine. This means that instead of requiring columns of sizes R^3, R^2, and R, we instead only need R, R^2, and R, which is vastly more efficient. Another way to see this is to observe when the highly-branching transitions occur. In this more efficient algorithm, branching occurs between $\hat{c}^\dagger$ to $\hat{c}^\dagger\hat{c}^\dagger$), thereby reducing the number of paths to keep track of to R^2. Of course, one could continue to further optimize the layout of the state machine, but we do not need a generic or completely optimal solution to this problem, only one that will render the BLG Hamiltonian small enough to fit in memory to be compressed.

Now that we have described the technique for writing down a sufficient efficient MPO construction, we will relax the artificial assumptions. Let us first relax the assumption that

only $c^\dagger c^\dagger cc$ terms appear. In general, we will have a Hamiltonian of the form

$$\begin{aligned} H &= H_{\text{hop}} + H_{\text{int}} = H_{\text{hop}} + H_2 + H_3 + H_4 \\ H_{\text{hop}} &= \sum_{i<j} \tilde{V}_{ij}^{\dot{c}c} c_i^\dagger c_j + \sum_{i<j} \tilde{V}_{ij}^{c\dot{c}} c_i c_j^\dagger \\ H_2 &= \sum_{i<j} \tilde{V}_{ij}^{nn} n_i n_j \\ H_3 &= \sum_{i<j<k} \tilde{V}_{ijk}^{\dot{c}nc} c_i^\dagger n_j c_k + \tilde{V}_{ijk}^{n\dot{c}c} n_i c_j^\dagger c_k + \tilde{V}_{ijk}^{\dot{c}cn} c_i^\dagger c_j n_k \\ &\quad + \tilde{V}_{ijk}^{nc\dot{c}} n_i c_j c_k^\dagger + \tilde{V}_{ijk}^{cn\dot{c}} c_i n_j c_k^\dagger + \tilde{V}_{ijk}^{c\dot{c}n} c_i c_j^\dagger n_k \\ H_4 &= \sum_{i<j<k<\ell} \tilde{V}_{ijk\ell}^{\dot{c}\dot{c}cc} c_i^\dagger c_j^\dagger c_k c_\ell + \tilde{V}_{ijk\ell}^{\dot{c}cc\dot{c}} c_i^\dagger c_j c_k^\dagger c_\ell \\ &\quad + \tilde{V}_{ijk\ell}^{\dot{c}cc\dot{c}} c_i^\dagger c_j c_k c_\ell^\dagger + \tilde{V}_{ijk\ell}^{cc\dot{c}\dot{c}} c_i c_j c_k^\dagger c_\ell^\dagger \\ &\quad + \tilde{V}_{ijk\ell}^{c\dot{c}c\dot{c}} c_i c_j^\dagger c_k c_\ell^\dagger + \tilde{V}_{ijk\ell}^{c\dot{c}\dot{c}c} c_i c_j^\dagger c_k^\dagger c_\ell, \end{aligned} \tag{A.23}$$

with all 2-body, 3-body, and 4-body interactions involving $c^\dagger, c$, and n operators, and $c^\dagger$ is represented by $\dot{c}$ for concision. We can make this representation more amenable to finite state machine description by mapping $\tilde{V}_{ijkl}$ to $V_{r_0 r_1 r_2 r_3}$ such that $V_{i(j-i)(k-j)(\ell-k)} = \tilde{V}_{ijkl}$(See Fig. A.3). By combining all of these, one can generate the full Hamiltonian Eq. (A.23) with $D(R) = 4R^2 + 6R + 2$ nodes. In practice, then, the spinless, single-valley BLG Hamiltonian on a cylinder with 6 momentum cuts (i.e. a unit cell of 12 sites) and interactions of range 10 unit cells is size $D \approx 58,000$ before compression.

A.4 Compression of infinite MPOs with general unit cells

This Appendix will present an algorithm for compressing infinite Matrix Product Operators (iMPOs) with non-trivial unit cells, a generalization of Ref. [61]. The main application for these algorithms to compress the Hamiltonian for bilayer graphene down to a sufficiently small bond dimension that DMRG may be performed easily, while retaining sufficient precision to determine its physical properties. However, as the technique may be of independent interest, we will keep our discussion sufficiently general that the results apply to any iMPO that shows up in 2D DMRG.

Let us briefly review the context in which this algorithm is useful. Suppose that you have a Hamiltonian $\widehat{H}$ for a 2D system, and wish to find the ground state with DMRG [11, 125]. A standard technique is to use a 'thin cylinder' geometry of circumference N_y sites and length $N_x \to \infty$. One then chooses a linear (1D) ordering for the sites on the cylinder by wrapping around in a helical pattern. This effectively reduces the problem to a 1D chain, but at a cost: interactions at distance r in 2D can be as far as $N_y \times r$ in

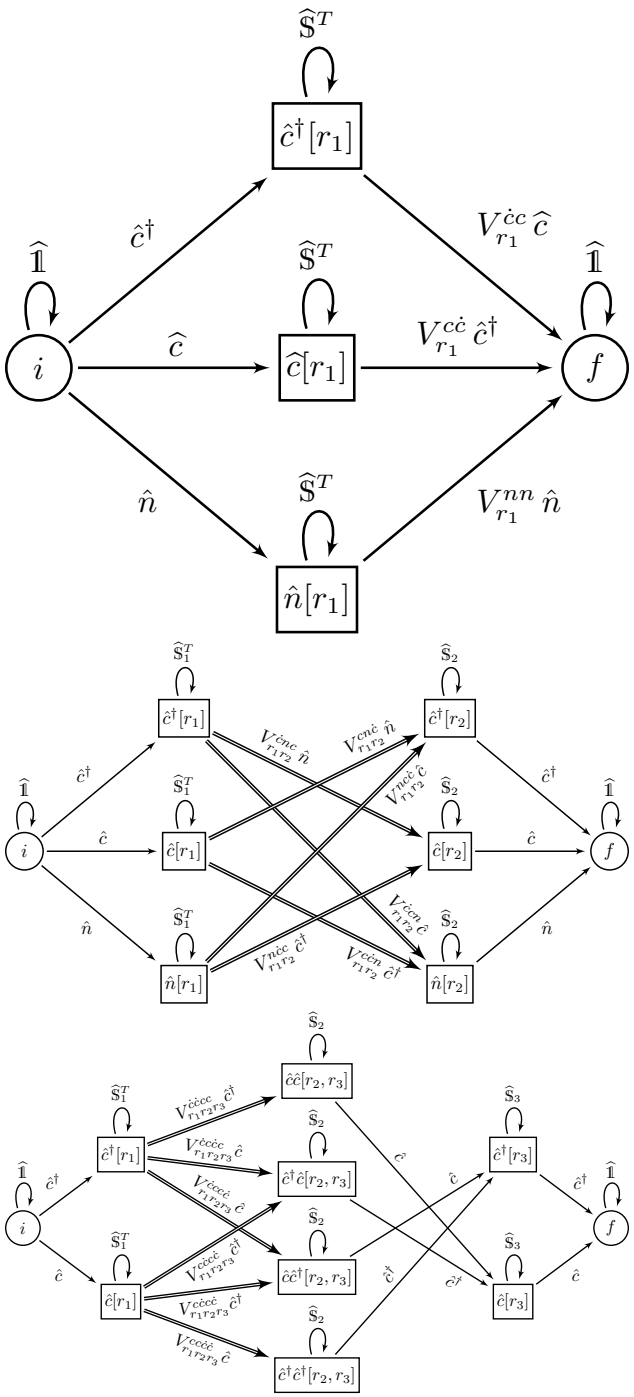

Figure A.3: Finite state machines for constructing the 2-body, 3-body, and 4-body interactions of Eq. (A.23). The notation is the same as in Fig. A.2: boxes stand for collections of many nodes with $1 \leq r_i \leq R$. For concision, the operator $c^\dagger$ is represented by $\dot{c}$ in superscripts. Note that some of the nodes can be reused among 2, 3, and 4-body paths. We have suppressed the r_0 index for clarity on the initial node and for the V coefficients; this shows the case of unit cell of size $N = 1$.

1D. Furthermore, the resource cost grows hugely, as the matrix product state (MPS) bond dimension needed to accurately capture a 2D area law state grows as $\chi \sim e^{N_y}$ [125]. In practice, therefore, 2D DMRG is often limited to around $N_y = 6 - 12$, even with bond dimensions of $\chi \sim 10,000$ or more. For sufficiently long-range interactions in 2D, however, the bottleneck is not the MPS bond dimension, but rather the MPO bond dimension needed to encode the Hamiltonian. For example, long-range 4-body interactions of range R result in iMPOs of bond dimension $D \sim R^2$ (see App. A.3), and hence DMRG scales as $D^2 \sim R^4$, which becomes quickly impractical. The algorithms given below allow one to proceed by finding the best approximation for the iMPO of bond dimension $D' < D$. For many physical Hamiltonians, this compression incurs only a minor penalty (say, 10^{-4}) in the precision of the eventual ground state. In the case of the single-valley IBM model we have used in this paper, the bond dimension may be reduced by a factor of 10^3, vastly improving the speed of DMRG.

The rest of this Appendix is organized as follows. We first give an overview of iMPO compression in the case without unit cells to set notation. We then discuss how an iMPO may be "topologically ordered", how this vastly speeds up compression, and present a practical compression algorithm. Afterwards we examine the properties of compressed Hamiltonians: under reasonable assumptions (1) Hermiticity is retained, (2) the fidelity of the compressed ground state versus the true ground state is high, and (3) their ground state energy and expectations values are accurate.

Lightning Review of iMPO Compression

We briefly review the notion of iMPO compression from [61]. It is well-known that the optimal way to compress a 1D matrix product *state* is to perform a Schmidt decomposition and drop the smallest singular values (see [126] or [74] for a review). For iMPOs, we employ the same basic technique with a few modifications to preserve the locality of the operator.

We first present the algorithm in terms of (non-matrix product) local operators. Consider a local operator $\widehat{H}$ on an infinite 1D chain. We can split $\widehat{H}$ into left and right halves at some bond:

$$\widehat{H} = \widehat{H}_L \widehat{\mathbb{1}}_R + \widehat{\mathbb{1}}_L \widehat{H}_R + \sum_{a,b=1}^{D} \widehat{h}_L^a \mathsf{M}_{ab} \widehat{h}_R^b \tag{A.24}$$

where a subscript L or R means the operator is supported entirely on the left or right half, respectively, and the matrix M keeps track of the terms which straddle the cut. This decomposition is not unique; we have the freedom to apply arbitary unitaries on the left and right. We can take advantage of this freedom to put $\widehat{H}$ into **almost-Schmidt form**

$$\widehat{H} = \widehat{H}_L \widehat{\mathbb{1}}_R + \widehat{\mathbb{1}}_L \widehat{H}_R + \sum_{a=1}^{D} \widehat{O}_L^a s_a \widehat{O}_R^a \tag{A.25}$$

where both $\{\widehat{O}_L^a\}$ and $\{\widehat{O}_R^a\}$ are orthonormal collections under the scaled Frobenius norm

$$\langle A, B\rangle := \mathrm{Tr}[\widehat{A}^\dagger \widehat{B}]/\,\mathrm{Tr}[I], \tag{A.26}$$

and where $s_1 \geq s_2 \geq \cdots \geq s_D \geq 0$ are referred to as the singular values.[4] We further require that the operators $\widehat{O}_{L,R}^a$ are **identity free**, i.e. $\langle \widehat{\mathbb{1}}_{L,R}, \widehat{O}_{L,R}^a\rangle = 0\ \forall a$. The **compressed operator** is then simply the truncation of the sum to the largest $D' < D$ singular values

$$\widehat{H}' := \widehat{H}_L \widehat{\mathbb{1}}_R + \widehat{\mathbb{1}}_L \widehat{H}_R + \sum_{a=1}^{D'} \widehat{O}_L^a s_a \widehat{O}_R^a. \tag{A.27}$$

One can show that $\widehat{H}'$ is the best approximation to $\widehat{H}$ with only D' 'terms' straddling the cut [61]. Furthermore, as we shall see below, the accuracy of the approximation is controlled by the **truncated singular value weight**

$$\epsilon^2(D') := \sum_{a=D'+1}^{D} s_a^2. \tag{A.28}$$

To *compute* almost-Schmidt forms and compress operators, we work in the framework of matrix-product operators. We now recall their definitions to set notation and a few essential properties. Suppose we have a space of on-site operators with an orthonormal basis $\{\widehat{\mathbb{1}}, \widehat{O}_2, \ldots, \widehat{O}_d\}$ where $\langle \widehat{O}_\alpha, \widehat{O}_\beta\rangle = \delta_{\alpha\beta}$ is an inner product.[5] Any translation-invariant operator, with unit cell of size N, can be written as[6]

$$\widehat{H} = \cdots \left[\widehat{W}^{(1)}\widehat{W}^{(2)}\cdots\widehat{W}^{(N)}\right]\left[\widehat{W}^{(1)}\cdots\widehat{W}^{(N)}\right]\cdots \tag{A.29}$$

where each $\widehat{W}^{(n)} = \sum_{\alpha=1}^{d} [W^{(n)}]^\alpha \widehat{O}_\alpha$ is an operator-valued matrix of size $D^{(n)} \times D^{(n+1)}$. We require each $\widehat{W}^{(n)}$ to have blocks of size $(1, D^{(n)}-2, 1) \times (1, D^{(n+1)}-2, 1)$

$$\widehat{W} = \left(\begin{array}{c|c|c} \widehat{\mathbb{1}} & \widehat{\mathbf{c}} & \widehat{d} \\ \hline & \widehat{A} & \widehat{\mathbf{b}} \\ \hline & & \widehat{\mathbb{1}} \end{array}\right) \tag{A.30}$$

This ensures that each operator is a sum of terms that are the identity far enough to the left or right — a physical and mathematical necessity for a local operator.

[4] We note that the singular values resulting from an almost-Schmidt decomposition and a true Schmidt decomposition are slightly different. Their relation is described in Section 8 of [61].

[5] For example, a spin-$\frac{1}{2}$ chain has an on-site basis of the Pauli matrices $\{\widehat{\mathbb{1}}, \widehat{X}, \widehat{Y}, \widehat{Z}\}$.

[6] This is notation for multiplication along the virtual indices: $[\widehat{W}^{(1)}\widehat{W}^{(2)}]_{ac} := \sum_{b=1}^{D^{(2)}} \left[W^{(1)}\right]_{ab}^{\alpha} \left[W^{(2)}\right]_{bc}^{\beta} \widehat{O}_\alpha \otimes \widehat{O}_\beta$.

An MPO is said to be in **left-canonical form** if all but the last column of each $\widehat{W}^{(n)}$ are mutually orthonormal:[7]

$$\sum_{a=1}^{D-1} \langle \widehat{W}^{(n)}_{ab}, \widehat{W}^{(n)}_{ac} \rangle = \delta_{bc}, \quad \forall n \in \mathbb{Z}/N\mathbb{Z}, 1 \leq b, c \leq D-1. \tag{A.31}$$

Similarly, an MPO is **right-canonical** if all the rows except the first are mutually orthonormal.

The representation (A.29) is not unique, which is a manifestation of gauge freedom. Two MPOs $\{\widehat{W}^{(n)}\}$ and $\{\widehat{W}^{(n)'}\}$ are **gauge equivalent** if there gauge exist matrices $\{G_n\}$ such that

$$G_{n-1}\widehat{W}^{(n)'} = \widehat{W}^{(n)}G_n, \quad n \in \mathbb{Z}/N\mathbb{Z}. \tag{A.32}$$

So long as $\widehat{H}$ is sufficiently local, one can show[61] there exist a gauge where the $\widehat{W}^{(n)}$'s are left-canonical (and another gauge for right canonical).

Now that we have set definitions, the next section describes the compression algorithm for unit cell MPOs.

The Unit Cell Compression Algorithm

The rough idea of the compression algorithm for unit cell MPOs $\{\widehat{W}^{(n)}\}$ is as follows.

1. Compute the right-canonical form $\{\widehat{W}^{(n)}_R\}$.
2. Find the gauge transform $\{G_n\}$ needed to transform to left-canonical form $\{\widehat{W}^{(n)}_L\}$.
3. Take the SVD decomposition of the gauge transformation matrix: $G_n = U_n S_n V_n^\dagger$ and absorb the unitaries into the $\widehat{W}$'s. This realizes the almost-Schmidt decomposition of Eq. (A.25).
4. Truncate the number of singular values in S_n from $D^{(n)}$ to $D^{(n)'}$ and correspondingly reduce the bond dimensions of the $\widehat{W}$'s, producing the compressed Hamiltonian.

The rest of this section is devoted to showing the correctness of this procedure and filling in the details. It turns out that the most subtle part by far is canonicalization — the algorithm for putting an MPO into left/right canonical form. We therefore delay the discussion of canonicalization to Appendix 31 below and for now simply assume it can be done.

We specialize to the case of $N = 2$ sites in the unit cell for concision, as larger unit cells are a direct generalization. Suppose that

$$R_{n-1}\widehat{W}^n_R = \widehat{W}^{(n)}R_n \tag{A.33}$$

[7] More explicitly, if $\sum_{\alpha=1}^{d}\sum_{a=1}^{D-1}[W^{(n)}]^{\alpha *}_{ab}[W^{(n)}]^{\alpha}_{ac} = \delta_{bc}$ for each $\widehat{W}^{(n)}$.

is a gauge transformation so that the $\widehat{W}_R^{(n)}$'s are right-canonical. Then

$$\widehat{H} = \cdots \widehat{W}^{(1)}\widehat{W}^{(2)}\widehat{W}^{(1)}\widehat{W}^{(2)}\cdots \tag{A.34}$$

$$= \cdots \widehat{W}_R^{(1)}\widehat{W}_R^{(2)}\widehat{W}_R^{(1)}\widehat{W}_R^{(2)}\cdots \tag{A.35}$$

$$\tag{A.36}$$

by introducing R_2 at ∞ and sweeping to the right. We can then impose a further gauge transformation to make the first row of each $\widehat{W}_R^{(n)}$ simultaneously identity-free. This is done by

$$R'_n := \begin{pmatrix} 1 & \mathbf{t}_n & 0 \\ 0 & I & 0 \\ 0 & 0 & 1 \end{pmatrix}, \tag{A.37}$$

where the $1 \times (D^{(n)} - 2)$-dimensional vectors $\mathbf{t}_n$ are chosen such that $0 = \mathbf{c}_0^{(n)} + \mathbf{t}_n - \mathbf{t}_{n+1}A_0^{(n)}$ where $A_0^{(n)}$ and $\mathbf{c}_0^{(n)}$ are the $\widehat{\mathbb{1}}$-components of $\mathbf{r}A^{(n)}$ and $\mathbf{c}^{(n)}$ respectively.

$$\begin{pmatrix} \mathbf{c}_0^{(1)} & \cdots & \mathbf{c}_0^{(N)} \end{pmatrix} = \\ \begin{pmatrix} \mathbf{t}_1 & \cdots & \mathbf{t}_N \end{pmatrix} \begin{pmatrix} I & & \cdots & -A_0^{(n)} \\ -A_0^{(1)} & I & & \\ & \ddots & \ddots & \\ & & -A_0^{(n-1)} & I \end{pmatrix}. \tag{A.38}$$

In practice, one should solve this by imposing the identity free condition column-by-column. For each new column, this requires solving a linear equation of size N. Using the same technique from Eq. (71) of [61], the total operation can be performed in $O(ND^2)$ operations.

Imposing this gauge we may assume $\widehat{W}_R^{(n)}$ has no identity components in its first row. This implies that the first column of $\widehat{W}_R^{(n)}$ is already orthogonal to all the other columns, such that the gauge transformation to the left-canonical form can be written as

$$C_{n-1}\widehat{W}_R^{(n)} = \widehat{W}_L^{(n)}C_n\,, \tag{A.39}$$

with block-diagonal gauge transformation matrices $C_n = \mathrm{diag}(1\ \mathsf{C}_n\ 1)$. Putting in a C_2 matrix at $-\infty$ and sweeping it to the center, we arrive at a mixed canonical form

$$\widehat{H} = \cdots \widehat{W}_L^{(1)}\widehat{W}_L^{(2)}C_2\widehat{W}_R^{(1)}\widehat{W}_R^{(2)}\cdots \tag{A.40}$$

$$= \cdots \widehat{W}_L^{(2)}\widehat{W}_L^{(1)}C_1\widehat{W}_R^{(2)}\widehat{W}_R^{(1)}\cdots \tag{A.41}$$

As C_n are block diagonal, we can compute their SVD's

$$C_n = U_n S_n V_n^\dagger \tag{A.42}$$

Algorithm 1 Unit Cell iMPO Compression

Require: $\{\widehat{W}^{(n)}\}$ is a first-order (see [61]) unit cell iMPO.

procedure UnitCellCompress($\widehat{W}^{(n)}, \eta$) ▷ Cutoff η
  $\widehat{W}_R^{(n)} \leftarrow \text{RightCan}[\widehat{W}^{(n)}]$
  $\widehat{W}_R^{(n)} \leftarrow R'_{n-1}\widehat{W}_R^{(n)}R_n'^{-1}$ so that $\widehat{\mathbf{c}}_0^{(n)} = 0$ ▷ Use $\mathbf{t_n}$ from Eq. (A.38).
  $\widehat{W}_L^{(n)}, C_n \leftarrow \text{LeftCan}[\widehat{W}_R^{(n)}]$
  $(U_n, S_n, V_n^\dagger) \leftarrow \text{SVD}[C_n]$
  $\widehat{Q}^{(n)}, \widehat{P}^{(n)} \leftarrow U_{n-1}^\dagger \widehat{W}_L^{(n)} U_n \,,\, V_{n-1}^\dagger \widehat{W}_R V$
  $D^{(n)} \leftarrow \max_a\{1 \le a \le D^{(n)}] : S_{aa}^{(n)} > \eta\}$ ▷ Defines the projector $\mathbb{P}_n$.
  $\widehat{Q}^{(n)} \leftarrow \mathbb{P}_{n-1}^\dagger \widehat{Q}_n \mathbb{P}_n$
  $S_n \leftarrow \mathbb{P}_n^\dagger S^{(n)} \mathbb{P}_n$
  $\widehat{P}^{(n)} \leftarrow \mathbb{P}_{n-1}^\dagger \widehat{P}^{(n)} \mathbb{P}_n$
  return $\widehat{Q}^{(n)}$

which will also be block-diagonal. Define

$$\widehat{Q}^{(n)} := U_{n-1}^\dagger \widehat{W}_L^{(n)} U_n \tag{A.43}$$

$$\widehat{P}^{(n)} := V_{n-1}^\dagger \widehat{W}_R^{(n)} V_n \tag{A.44}$$

for $n \in \mathbb{Z}/N\mathbb{Z}$. Then, since $U_n U_n^\dagger = I = V_n V_n^\dagger$, we have

$$\widehat{H} = \cdots \widehat{Q}^{(1)}\widehat{Q}^{(2)} S_2 \widehat{P}^{(1)}\widehat{P}^{(2)} \cdots \tag{A.45}$$

$$= \cdots \widehat{Q}^{(2)}\widehat{Q}^{(1)} S_1 \widehat{P}^{(2)}\widehat{P}^{(1)} \cdots \tag{A.46}$$

which is analogous to center-canonical form for MPS. The center bond can be swept back and forth via the gauge relation

$$S_{n-1}\widehat{P}^{(n)} = \widehat{Q}^{(n)} S_n, \quad n \in \mathbb{Z}/N\mathbb{Z}. \tag{A.47}$$

To see how compression works, we adopt the technique of assuming that the operator can be represented *exactly* by an MPO of lower bond-dimension, i.e. that a number of the singular values vanish exactly. Finding the lower bond dimension MPO uses the same algorithm as compression when the small singular values are truncated, so this shows the correctness of the algorithm.

Thus we assume, temporarily, that only $D^{(n)'}$ of the $D^{(n)}$ singular values of S_n are non-zero. Hence there are projection operators $\mathbb{P}_n$ from bond dimension $D^{(n)}$ to bond dimension $D^{(n)'}$ with $\mathbb{P}_n\mathbb{P}_n^\dagger$ a projector and $\mathbb{P}_n^\dagger\mathbb{P}_n = I_{1+\chi^{(n)'}+1}$ and

$$S_n = S_n \mathbb{P}_n \mathbb{P}_n^\dagger = \mathbb{P}_n S_n' \mathbb{P}_n^\dagger = \mathbb{P}_n \mathbb{P}_n^\dagger S_N \tag{A.48}$$

where S'_n is the projected diagonal matrix of non-zero singular values.

We can then introduce pairs of projectors on each bond:

$$\begin{aligned}\widehat{H} &= \cdots \widehat{Q}^{(1)}\widehat{Q}^{(2)}S_2\mathbb{P}_2\mathbb{P}_2^\dagger\widehat{P}^{(1)}\widehat{P}^{(2)}\cdots \\ &= \cdots \widehat{Q}^{(1)}S_1\widehat{P}^{(2)}\mathbb{P}_2\mathbb{P}_2^\dagger\widehat{P}^{(1)}\widehat{P}^{(2)}\cdots \\ &= \cdots \widehat{Q}^{(1)}S_1\mathbb{P}_1\mathbb{P}_1^\dagger\widehat{P}^{(2)}\mathbb{P}_2\mathbb{P}_2^\dagger\widehat{P}^{(1)}\widehat{P}^{(2)}\cdots \\ &= \cdots \mathbb{P}_2^\dagger\widehat{Q}^{(1)}\mathbb{P}_1\mathbb{P}_1^\dagger\widehat{P}^{(2)}\mathbb{P}_2S'_2\mathbb{P}_2^\dagger\widehat{P}^{(1)}\mathbb{P}_1\mathbb{P}_1^\dagger\widehat{P}^{(2)}\mathbb{P}_2\cdots \\ &= \cdots \mathbb{P}_1^\dagger\widehat{Q}^{(2)}\mathbb{P}_2\mathbb{P}_2^\dagger\widehat{P}^{(1)}\mathbb{P}_1S'_1\mathbb{P}_1^\dagger\widehat{P}^{(2)}\mathbb{P}_2\mathbb{P}_2^\dagger\widehat{P}^{(1)}\mathbb{P}_1\cdots\end{aligned} \tag{A.49}$$

It is now clear how to define a new representation for $\widehat{H}$ with a reduced bond dimension:

$$\widehat{P}^{(n)'} := \mathbb{P}_{n-1}^\dagger\widehat{P}^{(n)}\mathbb{P}_n \tag{A.50}$$

$$\widehat{Q}^{(n)'} := \mathbb{P}_{n-1}^\dagger\widehat{Q}^{(n)}\mathbb{P}_n \tag{A.51}$$

$$\tag{A.52}$$

whereupon

$$\widehat{H} = \cdots \widehat{Q}^{(1)'}\widehat{Q}^{(2)'}S_2\widehat{P}^{(1)'}\widehat{P}^{(2)'}\cdots \tag{A.53}$$

is a representation of $\widehat{H}$ with lower bond dimension. If we now relax the requirement that the truncated singular values were exactly zero, the strict equality of the new representation becomes approximate.

Canonicalization & Topological Sorting for Unit Cell MPOs

In this section we provide the "missing link" needed to complete the compression procedure: a canonicalization algorithm. Any unit cell MPO (UCMPO) can be put into left or right canonical form using QR iteration [61] with cost $O(ND^3)$. As many as 40 iterations can be necessary to reach high precision, making this quite slow in practice. However, the MPOs for Hamiltonians in DMRG have a special property, a "topological ordering", which enables canonicalization to be performed with cost $O(ND^3)$ but *without iteration*. For large MPOs such as the one for BLG with $D \sim 100,000$, this is a crucial speed-up. We first define a "topological ordering," then provide the canonicalization algorithm and a proof of its correctness and runtime. We conclude the section with a few remarks on practical implementation details.

An MPO can be thought of as a finite state machine (FSM) for placing on-site operators in a certain order [127]. For MPOs with N tensors in a unit cell, the FSM gains an additional structure: the FSM has N parts, with the nodes of part n corresponding to the bond between $\widehat{W}^{(n-1)}$ and $\widehat{W}^{(n)}$ and edges between parts $n-1$ and n corresponding to tensor elements $\widehat{W}^{(n)}_{ab}$. See Fig. A.4 for an example.

When one writes down an (non-unit cell) MPO $\widehat{W}$ for a Hamiltonian "by hand", then the MPO generally has a special structure: $\widehat{W}$ is upper-triangular as a matrix. In Ref. [61], the

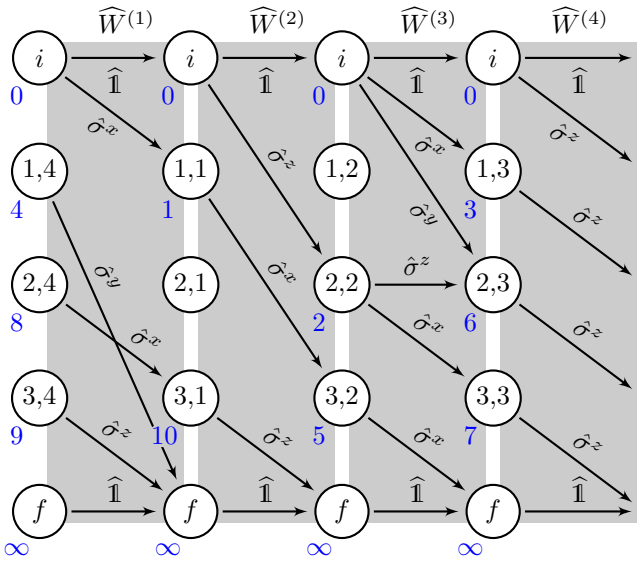

Figure A.4: An example of the finite state machine for an MPO with unit cell size 4. One on-site operator is placed for each arrow, and the arrows wrap around from right to left. Each gray box represents the data stored in one tensor. The UCMPO has bond dimension $(D_4, D_1, D_2, D_3) = (5, 4, 4, 5)$ and is loop free. The blue numbers are a (non-unique) topological ordering for the nodes.

upper triangular structure was shown to permit a fast canonicalization algorithm. However, this does not immediately generalize to a unit cell MPO, for a simple reason: if a unit cell MPO $\{\widehat{W}^{(n)}\}$ has bond dimensions $D^{(1)}, D^{(2)} \dots D^{(n)}$, not all equal, then the matrices are rectangular and cannot all be upper triangular. To find a good generalization of triangularity, we must look to the finite state machine.

A UCMPO $\{\widehat{W}^{(n)}\}_{n=1}^{N}$ is said to be **loop free** if its finite state machine contains no loops *after* the initial and final nodes are removed from the graph. For $N = 1$, then an upper-triangular MPO is always loops free, and a loop-free MPO is always upper-triangular (up to permutation). We stress that both the upper triangular and loop free conditions are gauge-*dependent*. Furthermore, for any N, if each $\widehat{W}^{(n)}$ is square and upper-triangular, then the UCMPO is loop free. The converse is almost true as well; any loop free UCMPO is an upper-triangular MPO "in disguise". To see this, we need a definition, which will be at the heart of this section.

Definition 1. A **topological ordering** for a UCMPO $\{\widehat{W}^{(n)}\}_{n=1}^{N}$ is an ordering of the nodes of the FSM (excluding the initial and final nodes)

$$O = \{(a_1, n_1) \prec (a_2, n_2) \prec \cdots \prec (a_D, n_D)\} \tag{A.54}$$

such that

$$\widehat{W}^{(n)}_{ab} = 0 \text{ whenever } (a, n) \succeq (b, n + 1), \tag{A.55}$$

where $n \in \mathbb{Z}/N\mathbb{Z}$ indexes the bonds (explicitly, bond $n+1$ connects $\widehat{W}^{(n)}$ to $\widehat{W}^{(n+1)}$), $a \in \mathbb{N}$ indexes the node within the bond, and $D = \sum_n D^{(n)}$ is the total number of nodes.

If an MPO is loop free, then its finite state machine (excluding the initial and final nodes) is a directed acyclic graph, and thus contains at least one topological ordering. This is easily computed by Kahn's algorithm (a standard result in graph theory) with cost linear in the number of nodes plus edges in the FSM. With this, we can show that loop free UCMPOs are upper triangular ones "in disguise" and then use this ordering as the basis for an efficient canonicalization algorithm.

Lemma 2. *Suppse $\{\widehat{W}^{(n)}\}_{n=1}^N$ is a loop free MPO. Then, by inserting rows and columns of zeros and permuting the rows and columns of the matrices (which is a gauge transform), $\{\widehat{W}^{(n)}\}$ can be made upper triangular.*

Proof. Suppose the bond dimension of $\widehat{W}^{(n)}$ is $D^{(n)}$ on the left and $D^{(n+1)}$ on the right, with $D = \sum_n D^{(n)}$. Let O be a topological ordering for $\{\widehat{W}^{(n)}\}$ of the form (A.54). Define a gauge matrix $\mathbb{P}_n$ of dimension $D^{(n)} \times D$ with matrix elements

$$[\mathbb{P}_n]_{b,i} = \begin{cases} 1 & \text{if } (b, n+1) = O_i \\ 0 & \text{otherwise.} \end{cases} \tag{A.56}$$

This "blows up" $\widehat{W}^{(n)}$ on the right to bond dimension $D > D^{(n+1)}$ by inserting zeros, and puts the indices into topological order. One can check that $\mathbb{P}_n^\dagger \mathbb{P}_n = I_{D^{(n+1)}}$, so we may define $\widehat{W}^{(n)\prime} := \mathbb{P}_{n-1}^\dagger \widehat{W}^{(n)} \mathbb{P}_n$ of size $D \times D$ (which obeys $\mathbb{P}_{n-1} \widehat{W}^{(n)\prime} = \widehat{W}^{(n)} \mathbb{P}_n$, making it a gauge transformation).

The new MPO $\widehat{W}^{(n)\prime}$ is upper-triangular. To see this, take $i \geq j$. Then either $\widehat{W}_{ij}^{(n)\prime} = W_{ab}^{(n)}$ for $O_i = (a, n)$ and $O_j = (b, n+1)$, or $\widehat{W}_{ij}^{(n)\prime} = 0$. But $O_i = (a, n) \succeq (b, n+1) = O_j$, so $W_{ab}^{(n)} = 0$ regardless. Therefore $\widehat{W}^{(n)\prime}$ is upper triangular. □

We present the algorithm for (left) canonicalization of loop free UCMPOs in Alg 2. We now prove its correctness, then analyze its cost.

Proposition 3. *Suppose $\{\widehat{W}^{(n)}\}_{n=1}^N$ is loop free. The output of Alg. 2 is a left canonical UCMPO.*

Proof. The main idea is to iterate over the columns of $\{\widehat{W}^{(n)}\}$ in topological order, orthogonalizing each column against all the previous ones as in Gram-Schmidt.

Let O be a topological order for the nodes as in (A.54). As each $\widehat{W}^{(n)}$ has the form (A.30), the first column of each is already orthonormal. We proceed by induction. Suppose that we have orthogonalized columns up to $(d, n+1) \in O$. Then for $(a, m), (b, m) \prec (d, n+1)$,

$$\sum_c \langle \widehat{W}_{ca}^{(m)}, \widehat{W}_{cb}^{(m)} \rangle = \delta_{ab}. \tag{A.57}$$

Algorithm 2 Unit Cell iMPO (Left) Canonicalization

Require: $\{\widehat{W}^{(n)}\}_{n=1}^{N}$ is a loop free UCMPO.

procedure UnitCellLeftCanonical($\widehat{W}^{(n)}, \eta$)
  $O =$ Kahn'sAlgorithm[FSM[$\{\widehat{W}^{(n)}\}$]]
  for $(b, n+1) \in O$ **do**
    $P \leftarrow \{a \ : \ O \ni (a, n+1) \prec (b, n+1)\}$
    $r_a \leftarrow \sum_c \langle \widehat{W}_{ca}, \widehat{W}_{cb} \rangle \,, \quad \forall a \in P$
    $R \leftarrow I_{D_n}$, $R_{ab} \leftarrow r_a, \quad \forall a \in P$
    $\widehat{W}^{(n)} \leftarrow \widehat{W}^{(n)} R$, $\widehat{W}^{(n+1)} \leftarrow R^{-1} \widehat{W}^{(n+1)}$
    $R \leftarrow I_{D_n}$, $R_{bb} \leftarrow \left(\sum_c \langle \widehat{W}^{(n)}_{cb}, \widehat{W}^{(n)}_{cb} \rangle \right)^{-1/2}$
    $\widehat{W}^{(n)} \leftarrow \widehat{W}^{(n)} R$, $\widehat{W}^{(n+1)} \leftarrow R^{-1} \widehat{W}^{(n+1)}$
  return $\{\widehat{W}^{(n)}\}$

Let the *predecessor* nodes be $P := \{(a, n+1) \ : \ (a, n+1) \prec (d, n+1)\}$ and for each $(a, n) \in P$, define the inner products with all previous columns as

$$r_a := \sum_c \langle \widehat{W}^{(n)}_{ca}, \widehat{W}^{(n)}_{cd} \rangle \,, \tag{A.58a}$$

$$R := I_{D^{(n+1}} - \sum_{a \in P} r_a \mathbf{e}_{ad} \tag{A.58b}$$

where $\mathbf{e}_{ad}$ is the elementary matrix where entry ad is 1 and the rest are zero: $(\mathbf{e}_{ad})_{ij} = \delta_{ai}\delta_{dj}$. Here R is only non-identity in column d, and it performs elementary column operations when acting to the left and elementary row operations acting to the right. In particular, we have chosen it to perform one Gram-Schmidt step, orthogonalizing column d against previous columns of $\widehat{W}^{(n)}$. It is easy to invert R, $R^{-1} = I_{D^{(n)}} + \sum_{a \in P} r_a \mathbf{e}_{ad}$, so we can cast this Gram-Schmidt step as a gauge transform with a single non-identity gauge matrix:

$$\widehat{W}^{(n)\prime} := \widehat{W}^{(n)} R, \tag{A.59a}$$

$$\widehat{W}^{(n+1)\prime} := R^{-1} \widehat{W}^{(n+1)}. \tag{A.59b}$$

We then have two things to show: (i) that this gauge transform really does orthogonalize column d of $\widehat{W}^{(n)}$ against previous columns and (ii) that the gauge transform does not ruin the orthogonality condition of Eq. (A.57). Both are easy computations.

For (i), the effect of R acting on $\widehat{W}^{(n)}$ on the right is to add column c to column d with coefficient r_c:

$$\widehat{W}^{(n)} R = \widehat{W}^{(n)} - \sum_{c \in P} r_c \widehat{W}^{(n)} \mathbf{e}_{cd}.$$

The matrix $\widehat{W}^{(n)}\mathbf{e}_{cd}$ is the matrix with only column d non-zero, and whose values are those from column c of $\widehat{W}^{(n)}$. Let $\widehat{W}_{:,a}$ denote the ath column vector of $\widehat{W}$, as usual. Then

$$\langle \widehat{W}^{(n)}_{:,a}, [\widehat{W}^{(n)}\mathbf{e}_{cd}]_{:,d}\rangle = \langle \widehat{W}^{(n)}_{:,a}, \widehat{W}^{(n)}_{:,c}\rangle = \delta_{ac}$$

by (A.57). Therefore, for any $(a,n) \prec (d,n)$,

$$\begin{aligned}
&\langle \widehat{W}^{(n)'}_{:,a}, \widehat{W}^{(n)'}_{:,d}\rangle \\
&\quad = \langle \widehat{W}^{(n)}_{:a}, \widehat{W}^{(n)}_{:d}\rangle - \sum_{c\in P} r_c \langle \widehat{W}^{(n)}_{:,a}, [\widehat{W}^{(n)}\mathbf{e}_{cd}]_{:,d}\rangle \\
&\quad = r_a - \sum_{c\in P} r_c\delta_{ca} = 0.
\end{aligned}$$

Therefore column d of $\widehat{W}^{(n)}$ is orthogonal to each previous column.

For (ii), the effect of R^{-1} acting to the left on $\widehat{W}^{(n+1)}$ is to add row d to row c with coefficient r_c:

$$\widehat{W}^{(n+1)'} = \widehat{W}^{(n+1)} + \sum_{c\in P} r_c \sum_e \left(\widehat{W}^{(n+1)}_{de}\right)\mathbf{e}_{ce} =: \widehat{W} + \delta\widehat{W}.$$

Take $(a,n+1),(b,n+1) \prec (d,n)$. Then

$$[\delta\widehat{W}]_{:,a} = \sum_{c\in P} r_c \left(\widehat{W}^{(n+1)}_{da}\right)\mathbf{e}_{ca} = 0$$

since $\widehat{W}^{(n+1)}_{da} = 0$ as $(d,n) \succeq (a,n+1)$ by (A.55), and similarly $[\delta\widehat{W}]_{:,b} = 0$. Therefore,

$$\begin{aligned}
\langle \widehat{W}^{(n+1)'}_{:,a}, \widehat{W}^{(n+1)'}_{:,b}\rangle &= \langle \widehat{W}_{:,a} + \delta\widehat{W}_{:,a}, \widehat{W}_{:,b} + \delta\widehat{W}_{:,b}\rangle \\
&= \langle \widehat{W}_{:,a}, \widehat{W}_{:,b}\rangle + 0 = \delta_{ab},
\end{aligned}$$

so the induction hypothesis (A.57) holds for $\{\widehat{W}^{(n)'}\}$.

As the gauge transform R adds previous columns to column d of $\widehat{W}^{(n)}$ and adds row d of $\widehat{W}^{(n+1)}$ to previous rows, the transformed UCMPO is also loop free. Thus after this gauge transform, column d of $\widehat{W}^{(n)'}$ is orthogonal to all previous columns and all of the structure of the UCMPO is preserved.

A similar, simpler gauge transform

$$R = I_{D^{(n+1)}} + \Big(\sum_c \langle \widehat{W}^{(n)'}_{cd}, \widehat{W}^{(n)'}_{cd}\rangle\Big)^{-1/2}\mathbf{e}_{dd}$$

can then be used to normalize column d of $\widehat{W}^{(n)'}$. Repeating the previous arguments, one can show that this similarly does not disrupt the orthogonality of $\widehat{W}^{(n+1)'}$ or the loop free condition. Therefore we have made one more column orthonormal to the previous ones, completing the proof. □

Algorithm 2 is quite efficient, with cost that scales as $O(\sum_n [D^{(n)}]^3)$. This is somewhat surprising, as it seems we are doing a total of $D = \sum_n D_n$ gauge transformations, each of which is a matrix multiplication. However, the R matrices are particularly simple: they only differ from the identity in a single column. The transformations $\widehat{W}^{(n)'} = \widehat{W}^{(n)} R$ and $\widehat{W}^{(n+1)'} = R\widehat{W}^{(n+1)}$ to orthogonalize a column may be performed with rank-1 matrix updates whose cost is only $O([D^{(n)}]^2)$. Similarly, the gauge transform to normalize a column, which simply scales a row or column, costs only $O(D^{(n)})$. As we must iterate over every column of every tensor, the total cost is then $O(\sum_n [D^{(n)}]^3)$. However, each iteration requires only elementary matrix operations, for which highly optimized libraries are available, and a low constant factor on the algorithm. One can also employ these algorithms with charge-conserving MPOs, which vastly decreases the runtime in practice.

Properties of Compressed Hamiltonians

We now show that compressed Hamiltonians are accurate approximations to the original Hamiltonian. This will give us guarantees that the (ground state) physics we are interested in is unchanged by compression. In fact, just as with matrix product *states*, the error is controlled by the weight of the truncated singular values. We demonstrate three properties of the compressed Hamiltonian H' *when we truncate a single bond*:

$$\widehat{H}_{\mathrm{BLG}} \to \widehat{H}'(\epsilon) \tag{A.60}$$

where $\widehat{H}'$ satisfies the following:

1. $\widehat{H}'$ is Hermitian
2. The ground state energy is accurate: $\delta E \leq 4^2\,\epsilon$
3. Observables are accurate: $\Delta\,\langle \widehat{O} \rangle \leq \frac{4^3}{\Delta E} ||\widehat{O}||\,\epsilon$
4. The ground state wavefunction is accurate: $|1 - \mathcal{F}| \leq \frac{4^4}{\Delta E^2}\,\epsilon^2$,

We reiterate that these are *local* bounds, corresponding to truncating a single bond. It is reasonable to expect that these results can be generalized to *global* bounds which apply when all bonds are truncated simulataneously, just as they can for matrix product states. However, such generalizations are often highly technical and therefore beyond the scope of this work. As a practical matter, Fig. 2.5 demonstrates that the global errors in the ground state energy, fidelity, and expectation values are small and decrease as $\epsilon(D) \to 0$.

Compressed Hamiltonians are Hermitian

All Hamiltonians in quantum mechanics are Hermitian. We now show that Hermiticity is preserved by dropping singular values of an Hamiltonian. There is just one caveat: if the spectrum contains a set of degenerate singular values, then one must drop either all of them or none of them:

Proposition 4. *Let $\widehat{H}$ be a Hermitian operator with the following almost-Schmidt form:*

$$\widehat{H} = \widehat{H}_L \widehat{\mathbb{1}}_R + \widehat{\mathbb{1}}_L \widehat{H}_R + \sum_{a=1}^{N_s} \sum_{i=1}^{D_a} \widehat{O}_L^{a,i} s_a \widehat{O}_R^{a,i} \tag{A.61}$$

where a labels degenerate singular values, N_s is the number of distinct singular values, and D_a is the degeneracy of the ath Schmidt value. Then, for any subset $\mathcal{A} \subset \{1, 2, ..., N_s\}$, the compressed operator

$$\widehat{H}' = \widehat{H}_L \widehat{\mathbb{1}}_R + \widehat{\mathbb{1}}_L \widehat{H}_R + \sum_{a\in\mathcal{A}} \sum_{i=1}^{D_a} \widehat{O}_L^{a,i} s_a \widehat{O}_R^{a,i} \tag{A.62}$$

is Hermitian.

For concision, we sketch the proof. Due to the orthonormality condition, $\widehat{H}_L\widehat{\mathbb{1}}_R$, $\widehat{\mathbb{1}}_L\widehat{H}_R$, and $\sum_{a=1}^{N_s}\sum_i^{D_a} \widehat{O}_L^{a,i} s_a \widehat{O}_R^{a,i}$ must be independently Hermitian. This implies they satisfy the relation $\sum_{a=1}^{N_s}\sum_i^{D_a} \widehat{O}_L^{a,i} s_a \widehat{O}_R^{a,i} = \sum_{a=1}^{N_s}\sum_i^{D_a} (\widehat{O}_L^{a,i})^\dagger s_a (\widehat{O}_R^{a,i})^\dagger$. Note that both the LHS and the RHS of this equation can be regarded as a singular value decomposition in operator space. It follows from the uniqueness of singular value decomposition that $\sum_i^{D_a} \widehat{O}_L^{a,i} s_a \widehat{O}_R^{a,i} = \sum_i^{D_a} (\widehat{O}_L^{a,i})^\dagger s_a (\widehat{O}_R^{a,i})^\dagger$ for any a. The proposition follows.

In practice, this means that one should always drop singular values by imposing a minimum value to retain rather than a maximum number.

We note that this result readily generalizes to a case when we truncate all bonds at the same time. To see this, we note that the proof above shows the action of Hermitian conjugation commutes with the singular value matrix. Then, just like in the case of symmetric MPS, singular values can be dropped without ruining Hermiticity.

Compressed Hamiltonians are Accurate

The accuracy of a compressed Hamiltonian is controlled by the weight of the truncated singular values in almost-Schmidt form, Eq. (A.28). Conceptually, one should think of truncation as introducing a small perturbation to the Hamiltonian. If the truncated weight is small, then the perturbation is small, and its effects to the ground state energy, the fidelity, and other observables are also small.

To quantify these effects, we employ the sup norm, an operator norm well-suited for ground state properties. If $\widehat{H}$ is an operator, then its **sup norm** $||\widehat{H}||$ is given by

$$||\widehat{H}||^2 := \sup_{|\psi\rangle} \frac{\langle\psi|\widehat{H}\widehat{H}|\psi\rangle}{\langle\psi|\psi\rangle}. \tag{A.63}$$

As the sup norm is extensive, we work with the sup norm per unit cell, so that it is finite.

We first quote a result from [61]: the change in the ground state energy is small under truncation.

Proposition 5 (Prop. 5 of [61]). *Suppose $\widehat{H}$ is a k-body Hamiltonian with on-site dimension d.*[8] *If $\widehat{H}$ is compressed from bond dimension D to $\widehat{H}'$ with D' with truncated weight*

$$\epsilon^2 := \sum_{a=D+1}^{D'} s_a^2, \tag{A.64}$$

Then the change in the ground state energy is bounded by

$$\delta E \leq ||\widehat{H} - \widehat{H}'|| \leq d^{\frac{k}{2}}\epsilon. \tag{A.65}$$

In practice, the singular values for an Hamiltonian fall off quite quickly — often exponentially, or as a power law at worse. So retaining only a small number of singular values can produce a highly accurate approximation for the ground state energy.

It is natural to assume that if the ground state energy is accurate, then the other ground state properties — such as expectation values of observables and even the entire ground state wavefunction — are accurate as well. Unfortunately, there is a rare but severe failure of this assumption. Near a first-order phase transition, a tiny perturbation to a Hamiltonian can push the system across the phase transition, changing the properties of the ground state in a discontinuous manner (except for the energy). However, as long as the competing states have large energy difference away from the transition, this will only cause infinitesimal shift of critical parameters. We can therefore understand the generic case by simply assuming we are far from a phase transition and the ground state changes continuously.

To do this, we work in first order perturbation theory. Suppose $\widehat{H}$ is a k-body Hamiltonian with a unique ground state with gap ΔE. Suppose we write $\widehat{H} = \widehat{H}' + \delta\widehat{H}$ with truncated weight ϵ^2 as in (A.64), and consider an observable of interest $\widehat{O}$. Then we can write the new ground state as

$$\begin{aligned} |E_0(\delta)'\rangle &= |E_0\rangle + |\delta E_0\rangle + O(\epsilon^2), \\ |\delta E_0\rangle &= \sum_{\lambda\neq 0} \frac{\langle E_\lambda|\delta\widehat{H}|E_0\rangle}{E_\lambda - E_0} |E_\lambda\rangle . \end{aligned}$$

Then

$$\begin{aligned} \Delta O &:= \left|\langle E_0(\delta)'|\widehat{O}|E_0(\delta)'\rangle - \langle E_0|\widehat{O}|E_0\rangle\right| \\ &= 2\left|\mathrm{Re}\,\langle E_0|\widehat{O}|\delta E_0\rangle\right| + O(\epsilon^2), \end{aligned}$$

[8] e.g. $d = 4$ for spin-$\frac{1}{2}$'s or spinless fermions.

so

$$\begin{aligned}
&\left|\langle E_0|\widehat{O}|\delta E_0\rangle\right| \\
&\leq \left|\sum_{\lambda\neq 0} \frac{\langle E_0|\delta\widehat{H}|E_\lambda\rangle \langle E_\lambda|\widehat{O}|E_0\rangle}{E_\lambda - E_0}\right| \\
&\leq \frac{1}{\Delta E}\left|\sum_{\lambda\neq 0} \langle E_0|\widehat{O}|E_\lambda\rangle \langle E_\lambda|\delta\widehat{H}|E_0\rangle\right| \\
&\leq \frac{1}{\Delta E}\left|\langle E_0|\widehat{O}\,\delta\widehat{H}|E_0\rangle - \langle E_0|\widehat{O}|E_0\rangle \langle E_0|\delta\widehat{H}|E_0\rangle\right| \\
&\leq \frac{2}{\Delta E}||\widehat{O}|| \cdot ||\delta\widehat{H}||
\end{aligned}$$

where we have used $\sum_{\lambda\neq 0} |E_\lambda\rangle \langle E_\lambda| = I - |E_0\rangle \langle E_0|$ and submultiplicativity of the norm. Using (A.65), the change in the expectation value is bounded by

$$\Delta O \leq \frac{4d^{\frac{k}{2}}}{\Delta E}||\widehat{O}||\ \epsilon. \tag{A.66}$$

We may therefore conclude that the error in expectation values should be small, provided that the uncompressed Hamiltonian is sufficiently far from a first-order phase transition. The condition of a gapped ground state may be relaxed, in which case the error will be controlled by the matrix elements of $\widehat{O}$ between the ground state and low-lying excited states.

Compressed Hamiltonians have High Fidelity

We have now seen that the ground state energy and expectation values of observables are accurately captured by the approximate, compressed Hamiltonian. In fact, the entire ground state wavefunction $|E_0'\rangle$ of $\widehat{H}'$ is very close to the original ground state wavefunction $|E_0\rangle$ of $\widehat{H}$. This allows us to use structural properties of $|\psi'\rangle$, such as its correlation length as a function of MPS bond dimension, as an accurate stand-in for the true ones and use them to e.g. diagnose the scaling properties of phase transitions.

To see this, we again work in perturbation theory, this time to second order. Let $\widehat{H} = \widehat{H}' + \delta\widehat{H}$ and take the same assumptions as above. Then we write

$$|E_0(\delta)'\rangle = |E_0\rangle + |\delta E_0\rangle + |\delta^2 E_0\rangle + O(\epsilon^3).$$

so

$$\langle E_0|E_0(\delta)'\rangle = 1 + 0 - \frac{1}{2}\sum_{\lambda\neq 0} \frac{\langle E_0|\delta\widehat{H}|E_\lambda\rangle \langle E_\lambda|\delta\widehat{H}|E_0\rangle}{(E_\lambda - E_0)^2}.$$

By the same argument as above the error in the ground state fidelity is bounded as

$$|1 - \langle\psi'|\psi\rangle| \leq \frac{d^k}{\Delta E^2}\ \epsilon^2. \tag{A.67}$$

	k space	xk space	MPO
E_{kin} (meV)	-69.099	-69.095	-69.095
E_{int} (meV)	32.263	32.257	32.257
ΔE_{kin} (meV)	-	4.2×10^{-3}	4.2×10^{-3}
ΔE_{int} (meV)	-	7.0×10^{-3}	6.4×10^{-3}

Table A.1: Energy of $|\psi_{\text{kin}}\rangle$ per momentum per band at $N_y = 2$, $w_0/w_1 = 0.825, d = 30$nm. MPO compression was performed with singular value truncation cutoff at 10^{-3}meV. The energy difference is calculated against the k space result.

In conclusion, we have now seen that the compressed MPOs should accurately reproduce the true ground state physics and provided error bounds on the precision. This justifies our use of compressed Hamiltonians to study twisted bilayer graphene.

A.5 Numerical cross checks

In addition to the analytic error bounds from the previous section, we also performed extensive numerical checks to verify that our computations were correct in practice as well as in principle. As mentioned above, we used the standard `TeNPy` library [74], written by one of us, for all DMRG calculations. The MPO compression code was carefully verified by unit testing, benchmarking, and a variety of cross-checks. The two primary cross-checks, which we now describe, verify the accuracy of the compression algorithm and the accuracy of the transformations between the various representations of the Hamiltonian.

Gauge Transform Verification

It is crucial that the compression algorithm is not only precise, as we have shown in previous sections, but also accurate. That is, the output of the implementation of the compression algorithm is indeed the compressed MPO described analytically. To verify this, we use the fact that Algorithm 1 is a gauge transformation, up until the truncation step. This gauge transformation obeys gauge relations given in Sec. 31, and reproduced here for convenience:

$$\begin{aligned} R_{n-1}\widehat{W}_R^n &= \widehat{W}^{(n)} R_n, \\ C_{n-1}\widehat{W}_R^{(n)} &= \widehat{W}_L^{(n)} C_n, \\ S_{n-1}\widehat{P}^{(n)} &= \widehat{Q}^{(n)} S_n. \end{aligned} \tag{A.68}$$

Due to the large number of small matrix elements, many indexing errors and other accuracy problems only manifest as small errors in the gauge relations. We therefore verified the gauge relations to precision 10^{-13}, nearly the floating point limit. Together with checks for

canonicality of $\widehat{W}_{R,L}$, this constitutes a sufficient check for the correctness of the algorithmic implementation.

Cross checks for tBLG Hamiltonian

In order to perform HF and DMRG calculations, one needs to represent the Hamiltonian in a variety of ways, as shown in Fig. 2.1, and it is imperative to make sure there is no error when we transform one representation to another. This section reviews a list of numerical checks we performed to guarantee correctness.

We first start from the momentum space representation, which is suitable for HF calculations. This interaction is specified by $V_{\mathbf{q}}$, together with the form factors $\Lambda_{\mathbf{q}}$. This representation can be Wannier localized (i.e. Fourier transformed) to obtain the mixed-xk space representation for iDMRG. Finally we use the mixed-xk space representation to construct an MPO, and compress it down to a smaller bond dimension. The first transformation is a unitary transformation, and is in principle exact up to numerical precision, whereas the precision of the compression is limited by MPO singular value cutoff.

In order to check if these transformations are accurate, we calculate a physical observable using each representation. The kinetic part H_{kin} of the BM Hamiltonian $h(k)$ is gapped for a wide range of parameters for small N_y, and the ground state $|\psi_{\text{kin}}\rangle$ is easy to calculate in each representation. Therefore, we can easily evaluate the following energies in momentum space, mixed-xk space, and DMRG.

$$\begin{aligned} E_{\text{kin}} &= \langle\psi_{\text{kin}}| H_{\text{kin}} |\psi_{\text{kin}}\rangle \\ E_{\text{int}} &= \langle\psi_{\text{kin}}| H_{\text{int}} |\psi_{\text{kin}}\rangle \end{aligned} \tag{A.69}$$

where H_{kin} and H_{int} are the kinetic and interaction part of the Hamiltonian, respectively. The comparison for $N_y = 2$ is shown in Table A.1. We see that the energy error is very small. We further check that these errors decrease as the accuracy of each calculation is increased (e.g. by increasing the cutoff range for MPO creation). We may conclude that the transformations between Hamiltonian representations are sufficiently accurate.

Appendix B

Appendix to chapter 3

B.1 Properties of the strained BM model and the self-consistent semi-metal at neutrality

In this appendix, we discuss additional properties of both the non-interacting BM model in the presence of non-zero strain, and the self-consistent semi-metal obtained in HF at the CNP for sufficiently large ϵ.

Fig. B.1 shows the single-valley BM band spectrum along a cut through the 2D mBZ, using $\theta = 1.05°$, and both $\epsilon = 0$ and $\epsilon = 0.3\%$. At finite strain, the bandwidth of the two active bands is much larger than the bandwidth at $\epsilon = 0$. Importantly, for $\epsilon = 0.3\%$ there is still a sizable gap between the active bands and the remote bands. This is especially important for our DMRG simulations, which work with an interacting Hamiltonian projected into the active bands only.

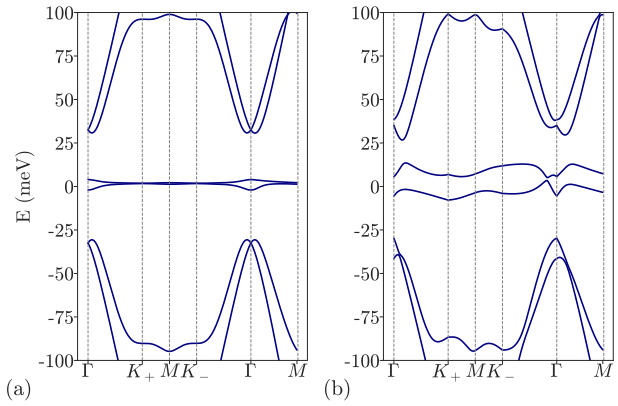

Figure B.1: Band spectrum of the single-valley BM model with twist angle $\theta = 1.05°$ along a cut through the mini-BZ. (a) Original BM model with $\epsilon = 0$. (b) Strained BM model with $\epsilon = 0.3\%$.

In Fig. B.2(a)-(b), we plot the difference and the average of the two active band energies

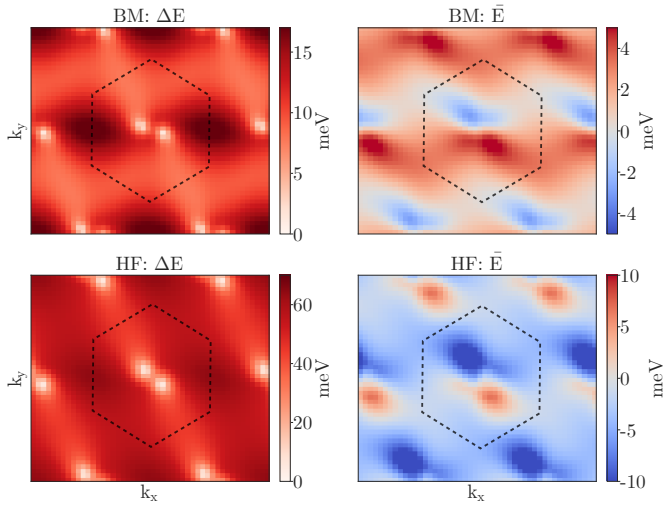

Figure B.2: BM and HF band energies in the $\tau = +$ valley using $\theta = 1.05°$ and $\epsilon = 0.22\%$. A coordinate transformation is performed in momentum space such that even with non-zero strain, the mBZ is a regular hexagon, indicated by the dashed lines. (a)-(b) Energy difference ΔE and average energy $\bar{E}$ of the two active bands of the BM Hamiltonian. (c)-(d) Energy difference ΔE and average energy $\bar{E}$ of the two active HF bands of the self-consistent SM. A dielectric constant $\varepsilon_r = 10$, a 24×24 momentum grid and $N_b = 6$ bands per spin and valley were used.

of the single-valley BM Hamiltonian in the entire mBZ, using a non-zero strain $\epsilon = 0.22\%$. Note that we have performed a coordinate transformation in momentum space such that the mBZ is a regular hexagon. From the difference in energies, one can clearly identify the position of the two Dirac cones, which as mentioned in the main text are in the vicinity of the Γ-point.

In Fig. B.2(c)-(d), we plot the energy difference and average of the two active bands in the mean-field band spectrum of the self-consistent SM in the $\tau = +$ valley at charge neutrality. The self-consistent SM was obtained using a strain value $\epsilon = 0.22\%$, at which the KIVC order is destroyed and the SM is the lowest-energy state. Similarly to the non-interacting BM Hamiltonian, the Dirac cones of the self-consistent SM are located near Γ. Away from these Dirac points, however, the two active bands in the $\tau = +$ valley are now separated by an energy difference of roughly 50 meV (using $\varepsilon_r = 10$), which is larger by a factor of 5 compared to the energy separation in the non-interacting BM model at the same value of ϵ.

To quantify how different the BM ground state is from the self-consistent SM at charge neutrality, we plot the Frobenius norm of $\mathsf{P}(\mathbf{k}) - \mathsf{P}_{\mathrm{BM}}(\mathbf{k})$ in Fig. B.3. As in the main text, $[\mathsf{P}(\mathbf{k})]_{(s',\tau',m),(s,\tau,n)} = \langle f^\dagger_{\mathbf{k},s,\tau,n} f_{\mathbf{k},s',\tau',m} \rangle$ is the correlation matrix of the self-consistent Slater determinant with the lowest energy, which is the SM for the strain value $\epsilon = 0.22\%$ used in Fig. B.3. $[\mathsf{P}_{\mathrm{BM}}(\mathbf{k})]_{(s',\tau',m),(s,\tau,n)} = \delta_{s,s'}\delta_{\tau,\tau'}\delta_{m,n}\Theta(\varepsilon_{\mathbf{k},\tau,n})$, with $\Theta(x)$ the Heaviside step function, is the correlation matrix of ground state of the non-interacting BM Hamiltonian at charge neutrality. From Fig. B.3, we see that $||\mathsf{P}(\mathbf{k}) - \mathsf{P}_{\mathrm{BM}}(\mathbf{k})||$ is equal to ~ 0.1 almost

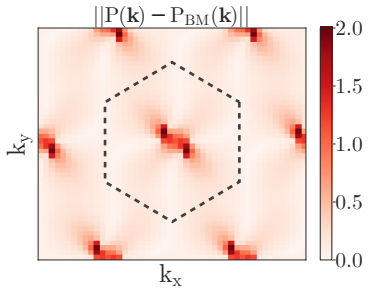

Figure B.3: Norm of the difference between the correlation matrix $\mathsf{P}(\mathbf{k})$ of the self-consistent SM and the correlation matrix $\mathsf{P}_{\mathrm{BM}}(\mathbf{k})$ of the ground state of the non-interacting BM Hamiltonian at charge neutrality, using twist angle $\theta = 1.05°$ and strain $\epsilon = 0.22\%$. A coordinate transformation is performed in momentum space such that the mBZ is a regular hexagon, indicated by the dashed lines. The self-consistent SM is obtained using $\varepsilon_r = 10$ and $N_b = 6$ bands per spin and valley.

everywhere in the mBZ, except close to the Γ point, where it becomes of order one. This shows that the self-consistent SM has significant overlap with the BM ground state in most of the mBZ already at small strain values.

The discrepancy between the BM ground state and the self-consistent SM in a small region near the Γ point is responsible for the differences in the LDOS discussed in the main text. Here, we further elaborate on this point. We define the energy and layer-resolved LDOS as

$$\rho_\ell(E,\mathbf{r}) = \frac{1}{A_{mBZ}} \sum_{s,\tau,n} \int \mathrm{d}^2\mathbf{k}\; \delta(E - \varepsilon_{\mathbf{k},s,\tau,n}) \sum_{\sigma=A,B} |\psi^{\ell,\sigma}_{\mathbf{k},s,\tau,n}(\mathbf{r})|^2 \,, \tag{B.1}$$

where $\ell = \pm$ denotes the graphene layers, A_{mBZ} is the area of the mBZ, $\varepsilon_{\mathbf{k},s,\tau,n}$ are the single-particle energies of the mean-field band spectrum, and $\psi^{\ell,\sigma}_{\mathbf{k},s,\tau,n}(\mathbf{r})$ are the corresponding single-particle wavefunctions. In practice, we calculate $\rho_\ell(E,\mathbf{r})$ by replacing the momentum integral by a discrete sum, and the delta-function by a Gaussian with a standard deviation of ~ 0.5 meV for the self-consistent SM, and ~ 0.2 meV for the BM ground state.

In Fig. B.4, we plot $\rho_+(\mathbf{r},E)$ for $E/W = -0.35, -0.11, 0.15$ and 0.35, where $W \sim 65$ meV is the HF bandwidth (an overall energy constant is fixed by imposing that $\sum_{\mathbf{k},n} \varepsilon_{\mathbf{k},n} = 0$). In Fig. B.4(a)-(b), we see a very clear C_{3z}-breaking in the LDOS at energies $E/W = -0.11$ and $E/W = 0.15$, which respectively correspond to $E \sim -7$ meV and $E \sim 10$ meV and thus lie outside the broad peaks in the DOS $\rho(E) = \int \mathrm{d}^2\mathbf{r} \sum_\ell \rho_\ell(E,\mathbf{r})$ (see Fig. 3.2 in the main text). At larger energies $E/W = \pm 0.35$, which correspond to values $E \sim \pm 20$ meV inside the broad peaks in the DOS, the C_{3z} breaking is also present, but is much less pronounced. At $E/W = -0.11$ and $E/W = 0.15$, the local charge distributions at the AA regions are clearly elongated in one direction. Contrary to what one might expect, these strongly C_{3z}-breaking charge distributions are not simply a consequence of strain, but instead rely on the Coulomb interaction. In particular, we find that for any value of E inside the active bands,

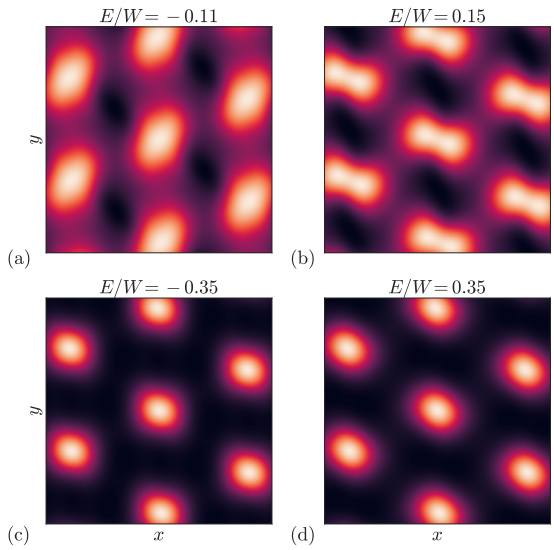

Figure B.4: (a)-(d) Local density of states $\rho_+(E, \mathbf{r})$ on the top layer (in arbitrary units) of the self-consistent SM obtained in HF. An overall energy constant is fixed by requiring that the HF single-particle energies $\varepsilon_{\mathbf{k},n}$ satisfy $\sum_{\mathbf{k}} \sum_n \varepsilon_{\mathbf{k},n} = 0$. The results were obtained on a 24×24 momentum grid using $\theta = 1.05°$, $\epsilon = 0.22\%$, $\varepsilon_r = 10$, and six bands per spin and valley.

$\rho_+(E, \mathbf{r})$ obtained from the non-interacting BM ground state does not show the same clear asymmetric charge distributions at the AA regions as does the self-consistent SM (for an example of the BM LDOS at two representative energies, see Fig. 3.2 in the main text). This implies that interactions are necessary to reconstruct the BM LDOS in order to obtain strong C_{3z} breaking.

B.2 Hartree-Fock at $\nu = -2$

In Fig. B.5 we show the SCHF results at filling $\nu = -2$. In particular, we plot the KIVC order parameter $|\Delta_{\text{KIVC}}|$ as a function of ϵ. We have performed four SCHF calculations, each with a different set-up. The first SCHF calculation was done using both spin flavors on a 24×24 momentum grid, keeping $N_b = 6$ bands per spin and valley. The second calculation was done on a rectangular 96×6 momentum gird, also with two spin flavors and six bands. The third SCHF calculation was again done on the same rectangular grid with two spin flavors, but now keeping only $N_b = 2$ bands per spin and valley. In the fourth and final SCHF calculation we reduced the number of spin components in the active bands from two to one (again working on the same rectangular grid and using $N_b = 2$). Importantly, even though we keep only one spin flavor for the active bands, the remote bands retain two spin flavors. This shows up in our Hamiltonian via the HF contribution of the remote bands to the free fermion part $h(\mathbf{k})$ of H [Eq. (4) main text].

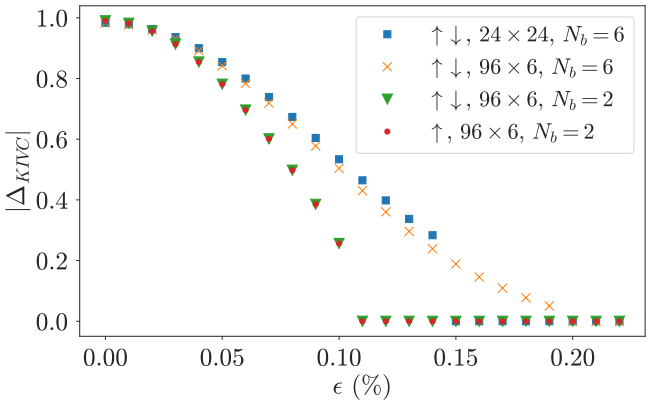

Figure B.5: Hartree-Fock KIVC order parameter as a function of strain ϵ at $\nu = -2$. $\uparrow\downarrow$ means that both spin flavors were used, while $\uparrow$ means that the active bands were taken to be spin polarized. The momentum grids used were of sizes 24×24 and 96×6 (with the smallest direction being the y-direction). N_b is the number of bands kept per spin and valley.

From Fig. B.5 we see that going from the square to the rectangular momentum grid stabilizes the KIVC state over larger strain values. On reducing the number of bands N_b from six to two, however, the strain interval over which we find KIVC order becomes significantly smaller. For all SCHF calculations where we keep both spin flavors, we find that the spin polarization $P_s := \frac{1}{N}\sum_{\mathbf{k}} \mathrm{tr}\,(\mathsf{P}(\mathbf{k})s_z)$, with s_z the Pauli-z matrix acting on spin indices, is independent of ϵ and retains its value $P_s = 2$. This is because the filled active bands are completely spin polarized by the exchange interaction. As a result, we see that the SCHF calculation on the rectangular grid with only one spin component for the active bands produces results that are indistinguishable from the results obtained for the complete model with both spin flavors. This justifies doing DMRG on the model with spin polarized active bands. We also see that the transition from the KIVC to the SM on the rectangular grid with $N_b = 2$ happens near $\epsilon \sim 0.1\%$, which is very close to the value where DMRG puts the phase transition (see main text).

B.3 Details of the DMRG Calcuations

Our DMRG calculations follow the method described in [15]. In brief, we start with a Bistrizer-MacDonald-like continuum model for TBG. We perform 1D hyrid Wannier localization which gives states that are localized in x and periodic along y. These states form the computational basis and have corresponding creation operators $c^\dagger_{x,k_y,\sigma,\tau}$ where $x \in \mathbb{N}$ indexes the x position, $k_y = 2\pi n/L_y$ runs over L_y momentum cuts through the mBZ, $\sigma = \pm 1$ labels sublattice, and $\tau = \pm$ labels the K and K' valleys. Each unit cell has $4L_y$ tensors, and respects $U(1)$ charge and valley symmetry. We then add Coulomb interactions as proscribed in Eq. (3.4), with a cutoff of 6 moiré unit cells. The matrix product operator (MPO) for

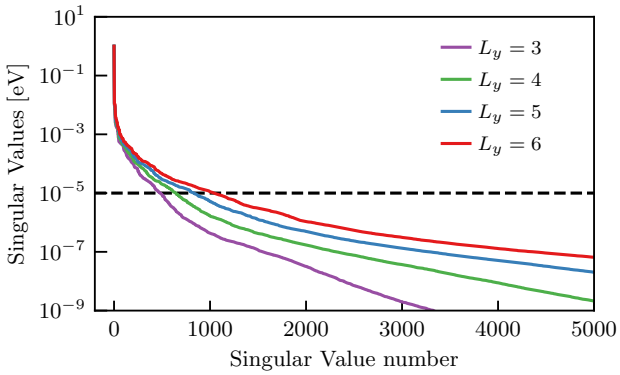

Figure B.6: The MPO singular values [61] for the Hamiltonian as a function of L_y. The dashed line represents our truncation level.

this Hamiltonian has bond dimension $D \approx 40,000$ at $L_y = 6$ — large, but unsurprising since this is a 2D model with a large unit cell, and long-range interactions. We use the MPO compression procedure of [61] to reduce this to $D \approx 1100$ while retaining a precision of 0.01 meV, as shown in Fig. B.6. Our DMRG is performed using the `TeNPy` library [74], written by one of us.

KIVC order parameter and correlation lengths with DMRG

This section details the KIVC order parameter used for DMRG. As mentioned in the main text, the KIVC phase breaks both valley charge conservation symmetry $e^{i\alpha\tau^z}$ as well as spinless time-reversal symmetry $\mathcal{T} = \tau^x K$ (K is complex conjugation), but preserves the product $\mathcal{T}' = e^{i\pi\tau^z/2}\mathcal{T} = \tau^y\mathcal{T}$. In 2D, the KIVC phase can be detected by the order parameters $\int d^2\mathbf{k}\, O_K^{\pm}(\mathbf{k})$, where $O_K^{\pm}(\mathbf{k}) = \sigma^y\tau^{\pm}(\mathbf{k})$. Here we have introduced the notation $\sigma^i\tau^j(\mathbf{k}) := c_{\mathbf{k}}^{\dagger}\sigma^i\tau^j c_{\mathbf{k}}$, and $\tau^{\pm} = \tau^x \pm i\tau^y$. The Pauli matrices σ^i act on the orbital indices of the two hybrid Wannier states in the same valley. The creation operators $c_{\mathbf{k},\sigma,\tau}^{\dagger}$ are in turn defined as $c_{k_x,k_y,\sigma,\tau}^{\dagger} := \sum_{x\in\mathbb{N}} e^{-ix(k_x+k_y/2)} c_{x,k_y,\sigma,\tau}^{\dagger}$ (in units where $k_x \in [0, 2\pi)$).

It is important to distinguish the KIVC phase from the time-reversal intervalley coherent (TIVC) phase, whose order parameters are $O_T^{\pm}(\mathbf{k}) = \sigma^x\tau^{\pm}(\mathbf{k})$. The following table shows how these operators behave under conjugation by symmetries: $O \to U^{-1}OU$.

Symmetry	$O_T^{\pm}(\mathbf{k})$	$O_K^{\pm}$
$\mathcal{T}$	$O_T^{\mp}(-\mathbf{k})$	$-O_K^{\mp}(-\mathbf{k})$
$\mathcal{T}'$	$-O_T^{\mp}(-\mathbf{k})$	$O_K^{\mp}(-\mathbf{k})$
$e^{i\alpha\tau_z}$	$e^{\pm i2\alpha}O_T^{\pm}(\mathbf{k})$	$e^{\pm i2\alpha}O_K^{\pm}(\mathbf{k})$

From this table it follows that $O_K^x(\mathbf{k}) := [O_K^+(\mathbf{k}) + O_K^-(\mathbf{k})]/2$, averaged over the whole BZ, vanishes for $\mathcal{T}$-symmetric phases but is generically non-zero for $\mathcal{T}'$-symmetric states — and

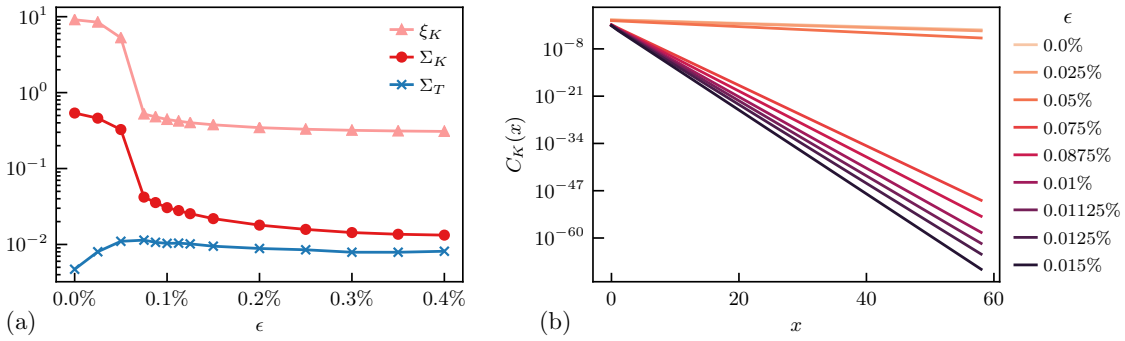

Figure B.7: (a) The correlation length in the KIVC sector ξ_K, as well as the summed KIVC and TIVC correlators $\Sigma_K = \sum_x C_K(x)$ and $\Sigma_T = \sum_x C_T(x)$ plotted as a function of strain ϵ. Note that ξ_K diverges with χ in the KIVC phase, as shown in Fig 4(c). One can see that Σ_K tracks ξ_K closely, but Σ_T does not, and that $\Sigma_T \ll \Sigma_K$. (b) The correlator $C_K(x)$ at a range of strain values. The transition is clearly visible. Parameters: $\nu = -2, L_y = 6, \Phi_y = 0, \chi = 2048$.

therefore distinguishes between the KIVC and TIVC states.

DMRG, as noted in the main text, uses a quasi-1D geometry which cannot support the spontaneously broken $U(1)$ valley symmetry that accompanies the KIVC phase. However, two-point functions of any order parameter with the correct symmetry quantum numbers will exhibit long-range order with a diverging correlation length. To that end, we consider

$$C_K(x) = \langle \Psi | \left(\sum_{k_y = \pm k_{y0}} O_K^+(x, k_y) \right) \left(\sum_{k'_y = \pm k_{y0}} O_K^-(0, k'_y) \right) | \Psi \rangle \,. \tag{B.2}$$

where

$$O_K^{\pm}(x, k_y) = [\sigma^y \tau^{\pm}](x, k_y) = i c^\dagger_{x,k_y,\sigma=1,\tau=\pm 1} c_{x,k_y,\sigma=-1,\tau=\mp 1} - i c^\dagger_{x,k_y,\sigma=-1,\tau=\pm 1} c_{x,k_y,\sigma=1,\tau=\mp 1}. \tag{B.3}$$

We have restricted the sum over k_y to a single pair of modes, symmetric across Γ to preserve $\mathcal{T}'$. At large x, $C_K(x) \sim e^{-x/\xi_K}$, where e^{-1/ξ_K} is the largest eigenvalue of the MPS transfer matrix in the relevant charge sector ΔQ_K. Explicitly, $\Delta Q_K = (\Delta q_{\text{electric}} = 0, \Delta q_{\text{valley}} = 2, \Delta k_y = 0)$. One way long-range order manifests is a divergence $\xi_K(\chi) \propto \chi$, which we show in Fig. 4 (main text). We caution that the divergence $\xi_K(\chi)$ alone is not enough to uniquely identify the KIVC phase; the TIVC order parameter $C_T(x)$ defined analogously to Eq. (B.2) with $O_T^{\pm} = [\sigma^x \tau^{\pm}](x, k_y)$, is also governed by the ΔQ_K sector of the transfer matrix, so a divergence in $\xi_K(\chi)$ could also be a sign of a TIVC phase. If this phase were TIVC, however, then $C_T(x)$ would exhibit long-range order, leading to a large value of $\Sigma_T = \sum_x C_T(x)$, and moreover that value would be governed by the correlation length ξ_K. Fig. B.7 shows this does not occur. Indeed, the TIVC correlator is suppressed by several orders of magnitude relative to the KIVC correlator. We may thus conclude the small strain phase in DMRG is indeed KIVC.

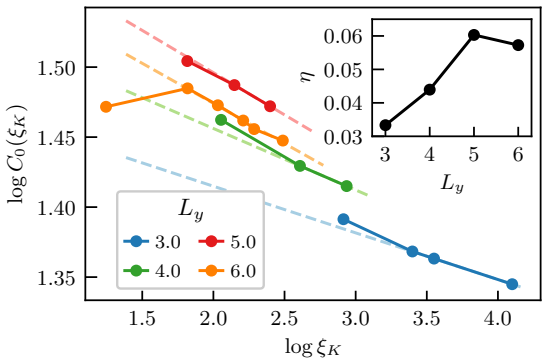

Figure B.8: Fitting coefficient $C_0(\xi_K)$ versus ξ_K at a range of cylinder radii L_y at $\nu = 0$ and $\epsilon = 0$. One can see that $C_0(\xi_K)$ decays as a power law for sufficiently large ξ_K. Inset: fits of $C_0(\xi_K) = \xi_K^{-\eta(L_y)}$.

Let us give a few details on how the scaling collapse in Fig. 4 (a) of the main text was performed. We expect the KIVC correlator to obey the scaling relation $C_K(x, \xi_K) = \xi_K^{-\eta(L_y)} C_K(x/\xi_K, 1)$ for some $\eta(L_y) \xrightarrow{L_y \to \infty} 0$. Our task is to determine η via a fitting procedure to perform the scaling collapse. At a finite bond dimension, all correlators must decay exponentially at sufficiently large x as e^{-x/ξ_K} (perhaps after a regime of algebraic decay). We therefore perform fits $C_K(x \gg 1, \xi_K) = C_0(\xi_K) e^{-x/\xi_K}$. By comparison with the scaling relation, one can see the prefactor to the exponential should scale as $C_0(\xi_K) \approx \xi^{-\eta}$. Fig. B.8 shows $C_0(\xi_K)$ does indeed decay as a power law for sufficiently large ξ_K, and fitting shows $\eta(L_y = 6) \approx 0.057$. A few comments are in order. First, the behavior of η is non-monotonic with L_y. We attribute this to finite size effects; one requires a cylinder radius of at least $L_y = 5$ for KIVC order to be clearly detectable. Second, the magnitude η is quite small. Typically, long-range order is visible at finite bond dimension as a range of intermediate x where $C_K(x) \sim x^{-\eta}$. However, as η is so small here, this intermediate range is extremely short, so the algebraic decay is not visible in the scaling collapse. Nevertheless, the fact that the data does obey the scaling collapse indicates it must have long-range order.

The Semimetal phase in DMRG

We now briefly describe how the semimetal phase found with SCHF can be detected within DMRG. Within DMRG, a phase with zero charge gap has an electronic correlation length which diverges with bond dimension. In this case, we expect a semimetal with two Dirac nodes, so the correlation length will diverge only for particular momenta. As our DMRG uses $L_y = 6$ evenly spaced cuts through the moiré Brillouin zone at $k_y = 2\pi n/L_y$, we will generically "miss" the Dirac nodes, and the correlation length will appear to be finite. However, we can insert (valley-dependent) flux Φ_y, which shifts the cuts to $k_y[n] = 2\pi(n + \tau\Phi_y)/L_y$ where $\tau = \pm 1$ is the valley label. Varying $0 \leq \Phi_y \leq 1$ will sweep the momentum cuts across the BZ, leading to a divergence in the electronic correlation length when the cut

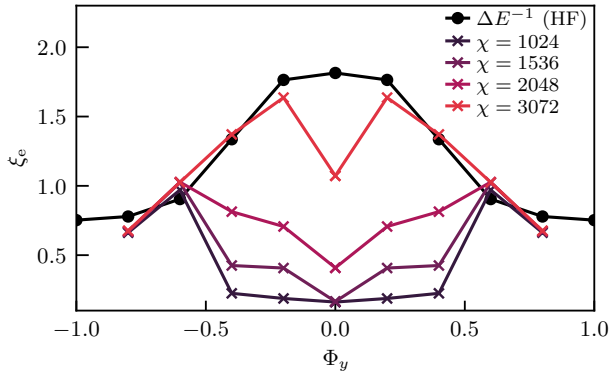

Figure B.9: Electronic correlation length ξ_e, defined in the text, as the momentum cuts are swept through the mBZ. The black circles are the inverse gap in SCHF at corresponding cuts through the mBZ in arbitary units: $\Delta E^{-1} = \min_{kx} \Delta E(k_x, k_y)$. One can see that the correlation lengths diverge with bond dimension for small Φ_y where the gap is minimal. Parameters: $\nu = 2$, $\epsilon = 0.4\%$, $L_y = 6$ for DMRG, $L_y = 30$ for SCHF.

is near to the Dirac node. As SCHF suggests that the Dirac nodes should be quite close to $k_y = 0$, we select the correlator $C_e(x) = \langle c^\dagger_{x,-k_y[n=0],\sigma=+1,\tau=+1} c^\dagger_{0,k_y[n=0],\sigma=+1,\tau=+1} \rangle \sim e^{-x/\xi_e}$. Figure B.9 shows that the correlation lengths do indeed begin to diverge with χ precisely where the gap in SCHF is minimal. Together with the fact that $\overline{S}_{vN} \approx 0$ for large ϵ — which signals that DMRG finds Slater determinant states — we may conclude that DMRG detects the same nematic semimetal phase as Hartree-Fock. Indeed, DMRG and SCHF even agree closely on the location of the phase transition from KIVC to semimetal which is around $\epsilon = 0.1$ %.

Appendix C

Appendix to chapter 4

C.1 Geometry of Moiré superlattice

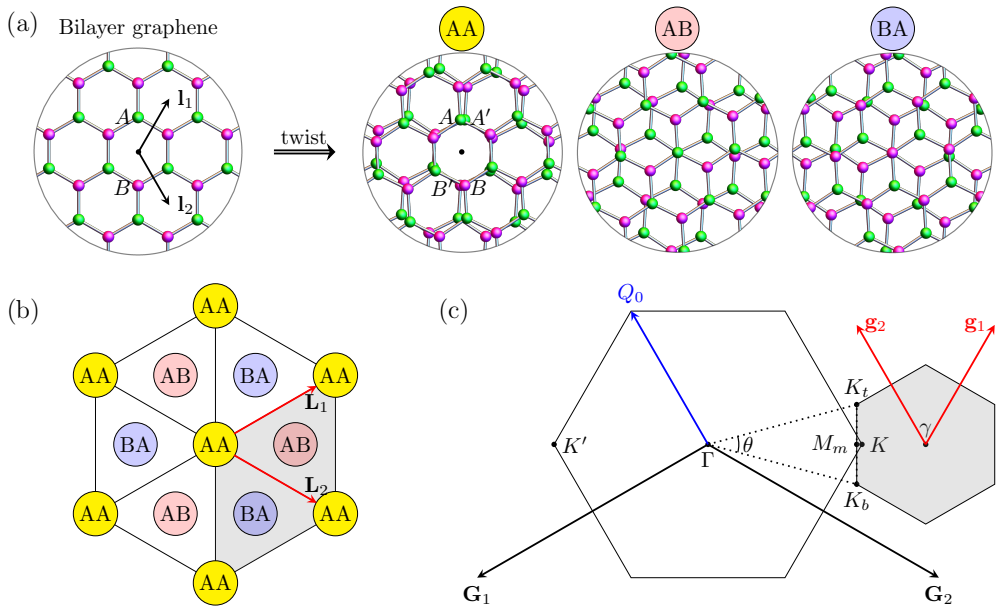

Figure C.1: Geometry of a twisted bilayer graphene (TBG) lattice in real- and reciprocal- space. (See Eq.(C.1)-(C.5) for notations.) (a) Zoomed-in top-view of a perfectly aligned bilayer graphene (BLG) and the AA,AB,BA-stacking regions of a TBG lattice obtained after rotating by a commensurate twist angle $\theta \sim 7.34°$. Here we demonstrate D_6-configuration where rotation center (also our origin) is at the center of a plaquette, so that the TBG respects $\mathcal{C}_2$-symmetry. (See Fig. C.4(a) for D_3, D_2-configurations). (A, B) and (A', B') denotes sublattice sites of the top and bottom layer, respectively. (b) Schematic illustration of the Moiré superlattice structure of TBG and its Moiré unit cell (gray region). (c) First Brillouin-Zone (BZ) of BLG and a mini-BZ (MBZ) of TBG (gray region) near the valley K. Intervalley scattering momenta Q_j $(j = 0, \cdots, 5)$ are related by sixfold-rotations. (See Eq. C.6, Fig. C.2(b), Fig. C.4(c).) One representative momentum Q_0 (blue arrow) is drawn here for brevity.

Geometry of a graphene lattice is defined by (Fig. C.1(a,c))

$$\mathbf{l}_1 = a_0\left(\frac{1}{2},\frac{\sqrt{3}}{2}\right),\ \mathbf{l}_2 = a_0\left(\frac{1}{2},-\frac{\sqrt{3}}{2}\right),\ a_0 = 0.246\,\mathrm{nm} \tag{C.1}$$

$$\mathbf{G}_1 = \frac{2\pi}{a_0}\left(-1,\frac{1}{\sqrt{3}}\right),\ \mathbf{G}_2 = \frac{2\pi}{a_0}\left(1,\frac{1}{\sqrt{3}}\right),\ K_+ = K = \frac{4\pi}{3a_0}(1,0),\ K_- = K' = \frac{4\pi}{3a_0}(-1,0). \tag{C.2}$$

Let $R(\theta)$ be a 2D rotation operator which rotates a vector by angle θ in the counter-clockwise direction. We adopt a convention where a twisted bilayer graphene (TBG) lattice is obtained by applying $R(\pm\theta/2)$ to the top and bottom graphene layer respectively. The resultant Moiré superlattice structure is defined by (Fig. C.1(b,c))

$$\mathbf{L}_1 = a_M\left(\frac{\sqrt{3}}{2},\frac{1}{2}\right),\quad \mathbf{L}_2 = a_M\left(\frac{\sqrt{3}}{2},-\frac{1}{2}\right),\quad A_M = \frac{\sqrt{3}a_M^2}{2},\quad a_M = \frac{a_0}{2\sin(\theta/2)} \tag{C.3}$$

$$K_{\tau,b} = R\left(\frac{\theta}{2}\right)K_\tau,\quad K_{\tau,t} = R\left(-\frac{\theta}{2}\right)K_\tau,\quad M_{m,\tau} = \frac{1}{2}(K_{\tau,b}+K_{\tau,t}) \tag{C.4}$$

$$\gamma_\tau = \frac{2\pi}{3a_M}\left(\tau\left(\sqrt{3}+\cot\left(\frac{\theta}{2}\right)\right),0\right),\quad \mathbf{g}_1 = \frac{2\pi}{a_M}\left(\frac{1}{\sqrt{3}},1\right),\quad \mathbf{g}_2 = \frac{2\pi}{a_M}\left(-\frac{1}{\sqrt{3}},1\right). \tag{C.5}$$

Here A_M denotes the area of a Moiré unit cell, $\tau = +,-$ labels the graphene valleys K, K', and γ-point refers to the origin of the mini-Brillouin Zone (MBZ) whose momentum-vector (γ_τ) is measured with respect to the Γ-point of the graphene BZ. Intervalley scattering momenta Q_j for $j = 0,\cdots,5$ are defined by

$$Q_j = R\left(\frac{\pi}{3}(j+2)\right)K. \tag{C.6}$$

We used a commensurate D_6 lattice configuration depicted in Fig. C.1(a) for our LDOS calculations unless otherwise specified. In the presence of strain, we followed Ref. [12, 16, 91] to take into account the effect of the lattice distortions.

C.2 Self-consistent Hartree-Fock calculations

We performed self-consistent Hartree-Fock (HF) calculations of the spinless interacting BM model. We used the double-gate screened Coulomb potential $V_q = \tanh|q|d_s/(2|q|\epsilon_0\epsilon_r)$ and peformed so-called subtraction procedure to avoid double counting of the Coulomb interaction. The details were reported elsewhere [8, 15]. We incorporated the effect of heterostrain according to Ref. [91]. The parameters used to perform HF calculation can be found in Table. C.1. We note that the DSM ground state is obtained from the BM model, so the interaction parameters do not matter for it.

By default, we use as our ansatz valley-diagonal and translation-independent Slater determinant. This means our basis states for the Slater determinant has coupling only within the same valley, and among states whose momenta are related by MBZ reciprocal lattice vectors.

In order to find the IVC phases, we allow wavefunctions in K-valley to couple to wavefunctions in K'-valley if their momentum difference is a MBZ reciprocal lattice vector. We emphasize that this choice does not break the Moiré-scale translation symmetry of the Hamiltonian.

The IKS state is found by further allowing breaking of the Moiré-scale translation symmetry. We allow a three-fold translation breaking in the $\mathbf{L}_1$-direction. While some incommensurate IKS states have lower energy, commensurate IKS is believed to capture most of important physics [12].

	DSM/VP/VH/K-IVC	nSM	IKS
gate distance d_s	250 nm		
Relative permitivity ϵ_r	12		
Twist angle	1.05 °		
w_1	110 meV		
w_0/w_1	0.8		
Number of active bands	2		
Filling factor ν	0		-1
lattice dimensions $n_x \times n_y$	24×24		
heterostrain ϵ	0 %	0.1 %	0.7 %

Table C.1: Parameters used for Hartree-Fock (HF) calculation. Filling factor ν is measured relative to the charge neutrality point (CNP) in the unit of number of electrons per Moiré unit cell, and the lattice dimensions $n_x \times n_y$ specify the number of k-points sampled in the mini-BZ of the Moiré superlattice.

C.3 Spectroscopy calculations

In this Section, we apply the Green's function formalism to self-consistent Hartree-Fock (HF) solutions of MATBG electronic system and define the spectroscopic observables (DOS, LDOS, FTLDOS) computed in this work. We further provide details on numerical evaluation procedure.

Green's function formalism

Let $|\mathbf{k}, \tau, C\rangle$ be the valley/Chern-polarized basis [7, 8] for the flat bands of Bistritzer-Macdonald (BM) Hamiltonian [4], where $\mathbf{k}$ is crystal momentum in the mini-BZ, $\tau = \pm 1$ labels the valleys $K_\pm = K, K'$, and $C = \pm 1$ labels the Chern number. A self-consistent

eigenstate solution $|\mathbf{k}, n\rangle$ of a HF Hamiltonian H_{eff} can be expressed as a linear combination of $|\mathbf{k}, \tau, C\rangle$, whose wavefunction is given by

$$\langle \mathbf{r}|\mathbf{k}, n\rangle = \sum_{\mathbf{g},\tau,C} F^{\mathbf{k},n}_{\tau,C} e^{i(\gamma_\tau+\mathbf{g}+\mathbf{k})\cdot\mathbf{r}}\, u^{\mathbf{k},\tau,C}_{\mathbf{g}}(\mathbf{r}). \tag{C.7}$$

$F^{\mathbf{k},n}_{\tau,C}$ are complex weights determined from the HF density matrix, $\mathbf{g}$ are the Moiré reciprocal lattice vectors, and $u^{\mathbf{k},\tau,C}_{\mathbf{g}}(\mathbf{r})$ is a cell-periodic function which satisfies $u^{\mathbf{k},\tau,C}_{\mathbf{g}}(\mathbf{r}) = u^{\mathbf{k},\tau,C}_{\mathbf{g}}(\mathbf{r}+\mathbf{L})$ for a commensurate Moiré superlattice.

We can recover $u^{\mathbf{k}}_{\mathbf{g},\tau,C}(\mathbf{r})$ by expanding it in terms of the Wannier-orbital basis $\varphi_\alpha(\mathbf{r}-\mathbf{r}_\alpha)$ localized at the carbon lattice sites $\mathbf{r}_\alpha = \mathbf{R}_\alpha + \mathbf{t}_\alpha$. Here $\alpha \in (A, B, A', B')$ labels the sublattices in top layer (A, B) and bottom layer (A', B'), while $\mathbf{R}_\alpha/\mathbf{t}_\alpha$ denotes the graphene unit cell/sublattice position vectors. Assuming $\varphi_\alpha(\mathbf{r}-\mathbf{r}_\alpha)$ has no spatial extent in the z-direction for simplicity, they form an orthonormal basis set and satisfy normalization condition $\int_{\mathbb{R}^2} d^2\mathbf{r}\, \overline{\varphi}(\mathbf{r}-\mathbf{r}_\alpha)\varphi(\mathbf{r}-\mathbf{r}_\beta) = \delta_{\alpha,\beta}\delta_{\mathbf{r}_\alpha,\mathbf{r}_\beta}$. In terms of $\varphi_\alpha(\mathbf{r}-\mathbf{r}_\alpha)$, we can write

$$u^{\mathbf{k},\tau,C}_{\mathbf{g}}(\mathbf{r}) = \frac{1}{\sqrt{N_k N_{uc}}} \sum_{\mathbf{R}_\alpha,\alpha} e^{-i(\gamma_\tau+\mathbf{k}+\mathbf{g})\cdot(\mathbf{r}-\mathbf{R}_\alpha-\mathbf{t}_\alpha)} B^{\mathbf{k},\tau,C}_{\mathbf{g},\alpha} \varphi_\alpha(\mathbf{r}-\mathbf{R}_\alpha-\mathbf{t}_\alpha). \tag{C.8}$$

N_k is the number of $\mathbf{k}$-points in the mini-BZ, N_{uc} is the number of graphene unit cells in a Moiré unit cell, and $B^{\mathbf{k},\tau,C}_{\mathbf{g},\alpha}$ are the complex coefficients obtained by diagonalizing the BM Hamiltonian.

Let $z = E + i\eta$ where E is energy and $\eta > 0$ is a Lorentzian broadening parameter in $\mathbb{R}$. Using Eq.(C.7), Eq.(C.8) and spectral representation of the retarded Green's function $\hat{G}(z) = (z - H_{\text{eff}})^{-1}$ [128], total LDOS $\rho(\mathbf{r}; z) = -\Im\left(\operatorname{Tr}\hat{G}(z)\right)/\pi$ can be expressed as

$$\rho(\mathbf{r}; z) = \frac{-1}{\pi}\Im\left(\sum_{\mathbf{k},n} \frac{|\langle \mathbf{r}|\mathbf{k}, n\rangle|^2}{z - E_{\mathbf{k},n}}\right) \tag{C.9}$$

$$= \frac{-1}{\pi}\Im\left(\sum_{\mathbf{k},n,\tau,\tau',\alpha,\beta,\mathbf{r}_\alpha,\mathbf{r}_\beta} \overline{\varphi}(\mathbf{r}-\mathbf{r}_\alpha)\frac{\Lambda^{\mathbf{k},n}_{\tau,\tau';\alpha,\beta}(\mathbf{r}_\alpha, \Delta\mathbf{r}_{\alpha\beta})}{z - E_{\mathbf{k},n}}\varphi(\mathbf{r}-\mathbf{r}_\alpha-\Delta\mathbf{r}_{\alpha\beta})\right), \tag{C.10}$$

where

$$\Lambda^{\mathbf{k},n}_{\tau,\tau';\alpha,\beta}(\mathbf{r}_\alpha, \Delta\mathbf{r}_{\alpha\beta}) = \frac{1}{N_k N_{uc}} \sum_{\mathbf{g},d\mathbf{g}} e^{i(\mathbf{k}+\mathbf{g}+d\mathbf{g}+\gamma_{\tau'})\Delta\mathbf{r}_{\alpha\beta}} e^{i(d\mathbf{g}+\gamma_{\tau'}-\gamma_\tau)\mathbf{r}_\alpha} \overline{\phi}^{\mathbf{k},n}_{\mathbf{g},\tau,\alpha} \phi^{\mathbf{k},n}_{\mathbf{g}+d\mathbf{g},\tau',\beta}. \tag{C.11}$$

$$\phi^{\mathbf{k},n}_{\mathbf{g},\tau,\alpha} = \sum_C F^{\mathbf{k},n}_{\tau,C} B^{\mathbf{k},\tau,C}_{\mathbf{g},\alpha}, \qquad \Delta\mathbf{r}_{\alpha\beta} = \mathbf{r}_\beta - \mathbf{r}_\alpha. \tag{C.12}$$

$E_{\mathbf{k},n} = \langle \mathbf{k}, n|H_{\text{eff}}|\mathbf{k}, n\rangle$ is the HF-energy and $d\mathbf{g}$ denotes a set of Moiré reciprocal lattice vectors chosen independently from $\mathbf{g}$. In numerical evaluation, we truncate the sum over $\mathbf{g}$ and $d\mathbf{g}$ after ensuring convergence, which required $|\mathbf{g}| < 0.3/a_0$ and $|d\mathbf{g}| < 0.8/a_0$. $\Delta\mathbf{r}_{\alpha\beta}$ is

limited up to third nearest neighbors. For all LDOS calculations, we chose an $\mathbf{r}$-meshgrid of resolution $0.01\,\mathrm{nm} \times 0.01\,\mathrm{nm}$.

Total DOS of the system is then obtained by integrating $\rho(\mathbf{r}; z)$ over a Moiré unit cell Ω_M of area A_M,

$$\rho(z) = \int_{\Omega_M} \frac{\mathrm{d}^2\mathbf{r}}{A_M}\, \rho(\mathbf{r}; z). \tag{C.13}$$

It is useful to decompose the total DOS/LDOS expressions in Eq.(C.9),(C.13),(C.16) into specific $(\tau, \tau'; \alpha, \beta)$ components by using Eq.(C.11). In particular, we define 'Kekulé -LDOS' $\rho^{\text{Kekulé}}(\mathbf{r}; z)$ and 'Kekulé -DOS' $\rho^{\text{Kekulé}}(z)$ for $\tau \neq \tau'$ as what follows:

$$\rho^{\text{Kekulé}}(\mathbf{r}; z) = \frac{-1}{\pi} \Im \left(\sum_{\mathbf{k}, n, \tau \neq \tau', \alpha, \beta, \mathbf{r}_\alpha, \mathbf{r}_\beta} \overline{\varphi}(\mathbf{r} - \mathbf{r}_\alpha) \frac{\Lambda^{\mathbf{k},n}_{\tau,\tau';\alpha,\beta}(\mathbf{r}_\alpha, \Delta\mathbf{r}_{\alpha\beta})}{z - E_{\mathbf{k},n}} \varphi(\mathbf{r} - \mathbf{r}_\alpha - \Delta\mathbf{r}_{\alpha\beta}) \right) \tag{C.14}$$

$$\rho^{\text{Kekulé}}(z) = \int_{\Omega_M} \frac{\mathrm{d}^2\mathbf{r}}{A_M} \left| \rho^{\text{Kekulé}}(\mathbf{r}; z) \right|. \tag{C.15}$$

We take the absolute value in Eq.(C.15) since Kekulé -LDOS can take negative value, unlike total LDOS. The Kekulé -DOS serves as our proxy for the graphene-scale modulation (Kekulé signal) due to intervalley scattering.

Let us now work out the analytic form of the total FTLDOS $\rho(\mathbf{q}; z) = \int_{\mathbb{R}^2} \mathrm{d}^2\mathbf{r}\, e^{-i\mathbf{q}\cdot\mathbf{r}} \rho(\mathbf{r}; z)$. By applying continuum Fourier-transformation to Eq.(C.9), we obtain

$$\rho(\mathbf{q}; z) = \frac{-1}{2\pi i} \left(\left(\sum_{\mathbf{k},n} \frac{\langle \mathbf{k}, n | \hat{\rho}_{\mathbf{q}} | \mathbf{k}, n \rangle}{z - E_{\mathbf{k},n}} \right) - \overline{\left(\sum_{\mathbf{k},n} \frac{\langle \mathbf{k}, n | \hat{\rho}_{-\mathbf{q}} | \mathbf{k}, n \rangle}{z - E_{\mathbf{k},n}} \right)} \right) \tag{C.16}$$

$$= \frac{-1}{2\pi i} \left(\mathrm{Tr}[\hat{\rho}_{\mathbf{q}} \hat{G}(z)] - \overline{\mathrm{Tr}[\hat{\rho}_{-\mathbf{q}} \hat{G}(z)]} \right) \tag{C.17}$$

where $\hat{\rho}_{\mathbf{q}} = e^{-i\mathbf{q}\cdot\hat{\mathbf{r}}}$ is density operator. Its matrix elements are given by

$$\langle \mathbf{k}, n | \hat{\rho}_{\mathbf{q}} | \mathbf{k}, n \rangle = \int_{\mathbb{R}^2} \mathrm{d}^2\mathbf{r}\, e^{-i\mathbf{q}\cdot\mathbf{r}} \left(\sum_{\tau,\tau',\alpha,\beta,\mathbf{r}_\alpha,\mathbf{r}_\beta} \overline{\varphi}(\mathbf{r} - \mathbf{r}_\alpha) \Lambda^{\mathbf{k},n}_{\tau,\tau';\alpha,\beta}(\mathbf{r}_\alpha, \Delta\mathbf{r}_{\alpha\beta}) \varphi(\mathbf{r} - \mathbf{r}_\alpha - \Delta\mathbf{r}_{\alpha\beta}) \right). \tag{C.18}$$

In practice, FTLDOS data is extracted by performing a Fourier transform of experimentally measured LDOS. To best mimic this procedure, FTLDOS data presented in this work is also computed via discrete Fourier transform of numerically computed LDOS. Given LDOS signals on a meshgrid of size $[-L, L] \times [-L, L]$, we computed discrete Fourier-transform after applying a Gaussian window function $W(x, y) = \exp(-(x^2 + y^2)/(2\sigma^2 L^2))$ with $\sigma = 0.35$. As long as the meshgrid region is sufficiently large enough to capture Moiré-scale modulations in $\rho(\mathbf{r}; z)$ (*i.e.* to resolve 'internal' splitting of the FTLDOS peaks in $\mathcal{O}(\mathbf{g})$-scale), we explicitly checked that the discrete Fourier-transformed LDOS data matches well with

the exact FTLDOS obtained from the evaluation of Eq.(C.16),(C.18) in momentum-space. Small spectral leakage and broadening of the Fourier modes were induced by the finite-sized window [129], but they did not affect qualitative features near the peaks of FTLDOS and hence were negligible.

Choice of orbitals

Let us briefly comment on our choice of φ. We construct our phenomenological Wannier orbitals from 2D Gaussian functions localized at $\mathbf{r}_\alpha$:

$$\phi_\alpha(\mathbf{r}-\mathbf{r}_\alpha) = \sqrt{\frac{2}{\pi l_{orb}^2}} e^{-|\mathbf{r}-\mathbf{r}_\alpha|^2/l_{orb}^2}, \tag{C.19}$$

whose density $|\phi_\alpha(\mathbf{r}-\mathbf{r}_\alpha)|^2$ is normalized to unity in $\mathbb{R}^2$. We imposed an approximate orthonormality of the orbitals by taking a superposition

$$\varphi_\alpha(\mathbf{r}-\mathbf{r}_\alpha) = \phi_\alpha(\mathbf{r}-\mathbf{r}_\alpha) - \sum_{\beta\in\langle\alpha\beta\rangle} \frac{\langle\phi_\alpha,\phi_\beta\rangle}{2}\phi_\beta(\mathbf{r}-\mathbf{r}_\beta) \tag{C.20}$$

where the sum is over the nearest neighbor sites of α, and $\langle,\rangle$ is an overlap integral between the orbitals. This ensures orthonormality up to $O(\langle\phi_\alpha,\phi_\beta\rangle^2)$ corrections.

We chose $l_{orb} \approx 0.263a_0$ to roughly reproduce the observed STM pattern of graphene [115] in the expectation that the orbital has substantial amplitude at the nearest-neighbor bond centers. This gives a bond-centered weight of $|\phi_\alpha(|\mathbf{r}-\mathbf{r}_\alpha| = a_0/2\sqrt{3})|^2/|\phi_\alpha(0)|^2 \approx 0.3$. In practice, l_{orb} can be a fitting parameter for reproducing experiment.

C.4 Derivation of Kekulé -LDOS signal extinction

We first show the case of antiunitary operator satisfying $\mathcal{K}^{-1}\hat{\rho}_\mathbf{q}\mathcal{K} = \pm\hat{\rho}_{-\mathbf{q}}$. Starting from Eq.(C.16), we check the total FTLDOS transforms under $\mathcal{K}$ via

$$\rho(\mathbf{q};z) = \frac{-1}{2\pi i}\left(\mathrm{Tr}[\hat{\rho}_\mathbf{q}\hat{G}(z)] - \overline{\mathrm{Tr}[\hat{\rho}_{-\mathbf{q}}\hat{G}(z)]}\right) \tag{C.21}$$

$$= \frac{-1}{2\pi i}\left(\mathrm{Tr}[\mathcal{K}\mathcal{K}^{-1}\hat{\rho}_\mathbf{q}\mathcal{K}\mathcal{K}^{-1}\hat{G}(z)] - \overline{\mathrm{Tr}[\mathcal{K}\mathcal{K}^{-1}\hat{\rho}_{-\mathbf{q}}\mathcal{K}\mathcal{K}^{-1}\hat{G}(z)]}\right) \tag{C.22}$$

$$= \frac{-1}{2\pi i}\left(\overline{\mathrm{Tr}[\mathcal{K}^{-1}\hat{\rho}_\mathbf{q}\mathcal{K}\mathcal{K}^{-1}\hat{G}(z)\mathcal{K}]} - \mathrm{Tr}[\mathcal{K}\mathcal{K}^{-1}\hat{\rho}_{-\mathbf{q}}\mathcal{K}\mathcal{K}^{-1}\hat{G}(z)\mathcal{K}]\right) \tag{C.23}$$

$$= \frac{-1}{2\pi i}\left(\pm\,\overline{\mathrm{Tr}[\hat{\rho}_{-\mathbf{q}}\hat{G}^\dagger(z)]} \mp \mathrm{Tr}[\hat{\rho}_\mathbf{q}\hat{G}^\dagger(z)]\right) = \pm\rho(\mathbf{q};z), \tag{C.24}$$

where in going from second to third line we used skew-cyclicity of trace of antiunitary operators: $\mathrm{Tr}[AB] = \overline{\mathrm{Tr}[BA]}$ for A, B antiunitary.

Similarly, for unitary operators satisfying $U^\dagger \hat{\rho}_{\mathbf{q}} U = \pm \hat{\rho}_{\mathbf{q}}$ we have

$$\rho(\mathbf{q}; z) = \frac{-1}{2\pi i}\left(\mathrm{Tr}[\hat{\rho}_{\mathbf{q}} \hat{G}(z)] - \overline{\mathrm{Tr}[\hat{\rho}_{-\mathbf{q}} \hat{G}(z)]} \right) \tag{C.25}$$

$$= \frac{-1}{2\pi i}\left(\mathrm{Tr}[U^\dagger \hat{\rho}_{\mathbf{q}} U U^\dagger \hat{G}(z) U] - \overline{\mathrm{Tr}[U^\dagger \hat{\rho}_{-\mathbf{q}} U U^\dagger \hat{G}(z) U]} \right) \tag{C.26}$$

$$= \frac{-1}{2\pi i}\left(\pm \mathrm{Tr}[\hat{\rho}_{\mathbf{q}} \hat{G}(z)] \mp \overline{\mathrm{Tr}[\hat{\rho}_{-\mathbf{q}} \hat{G}(z)]} \right) = \pm \rho(\mathbf{q}; z). \tag{C.27}$$

In either case, we see that the minus sign enforces $\rho(\mathbf{q}; z) = 0$.

C.5 Extraction of θ_{IVC}

In this Section, we explicitly demonstrate that the θ_{IVC} of K-IVC states can be extracted from LDOS measurement of K-IVC$_B$. As explained by Liu et al. [115], the intervalley coherent phase θ_{IVC} can be extracted from the phase structure of the FTLDOS up to a $\pi/3$ ambiguity. In that work the FTLDOS was used to detect Kekulé -symmetry breaking in the zeroth Landau-level of monolayer graphene in a magnetic field, and even the presence of skyrmions in the symmetry-breaking order parameter. The key ingredient was to identify particular combinations of FTLDOS signals that correspond to sublattice polarization and valley coherence. An essentially identical procedure can be applied to MATBG, since Moiré scale modulation should not change the analysis. We review this procedure, making suitable adjustments to account for the unique symmetry properties of K-IVC$_B$. This suggests that K-IVC skyrmions, which is a prerequisite for the proposed skyrmionic superconductivity of MATBG [10], might be observable from STM measurements.

For simplicity we start by assuming a MATBG in D_6-configuration (Fig. C.1(a)), such that the lattice has an exact $\mathcal{C}_2$-symmetry at the origin, a honeycomb plaquette center of the AA-region. Recall that a generic K-IVC state respects $\mathcal{T}'$ and $\mathcal{C}_2\mathcal{T}''$, where $\mathcal{T}' = \tau_z \mathcal{T}$ and $\mathcal{T}'' = \mathcal{T} e^{i\tau_z(\theta_{\mathrm{IVC}} - \pi/2)/2}$ [8]. Let us first look at 'special' states, e.g. $\mathcal{C}_2\mathcal{T}'$-invariant state which must have $\theta_{\mathrm{IVC}} = 0, \pi$. In the presence of a perpendicular magnetic field which breaks $\mathcal{T}$, the system still retains $\mathcal{C}_2$. Following an argument similar to Eq.(C.25)-(C.27), this implies that the Kekulé -FTLDOS of K-IVC$_B$ is purely real. In other words, Kekulé -LDOS is symmetric under $\mathcal{C}_2$ and results in a $\mathcal{C}_2$-symmetric total LDOS, see Fig. C.2(a). Similarly, $\mathcal{C}_2\mathcal{T}$-invariant states, necessarily at $\theta_{\mathrm{IVC}} = \pm\pi/2$, preserve $\mathcal{C}_2\tau_z$ and its Kekulé -FTLDOS becomes purely imaginary (i.e. Kekulé -LDOS is anti-symmetric under $\mathcal{C}_2$ and total LDOS loses $\mathcal{C}_2$-invariance, see Fig. C.2(b)). Because Kekulé -FTLDOS, directly sensitive to θ_{IVC}, is by definition peaked at the intervalley scattering-momenta Q_j, we henceforth focus on the intervalley peaks $\rho(Q_j)$ while assuming that the bias voltage of STM is chosen appropriately to maximize the Kekulé signals.

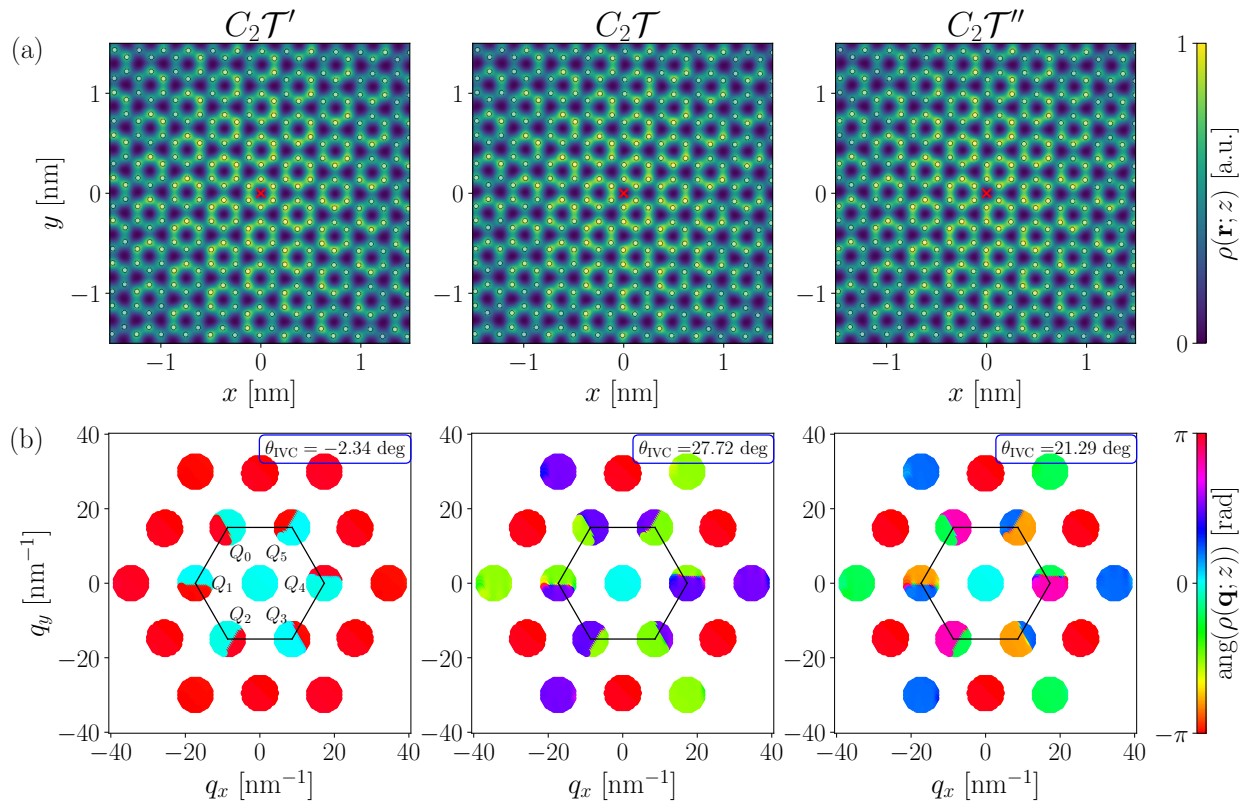

Figure C.2: (a) Total LDOS $\rho(\mathbf{r}; z = E+i\eta)$ and (b) phases of total FTLDOS $\rho(\mathbf{q}; z)$ for the $\mathcal{C}_2\mathcal{T}'$, $\mathcal{C}_2\mathcal{T}$, $\mathcal{C}_2\mathcal{T}''$-invariant spinless K-IVC states at CNP under magnetic field $E_B = 0.1\,$meV, characterized by $\theta_{\rm IVC} = 0°$, 30°, 23.61° mod 60°, respectively. Using Eq.(C.29), we extract $\theta_{\rm IVC} = -2.34°$, 27.72°, 21.29° mod 60°. The data shown is for the AA-region of bottom layer, at $E = -19.8\,$meV and $\eta = 0.1\,$meV.

Generic $\mathcal{C}_2\mathcal{T}''$-invariant states with $\theta_{\rm IVC} = \Delta\theta$ are related to the $\mathcal{C}_2\mathcal{T}'$-invariant states via valley rotation $e^{i\tau_z\Delta\theta/2}$. This induces a phase shift $\rho(Q_j) \to e^{i\Delta\theta}\rho(Q_{0/2/4}), e^{-i\Delta\theta}\rho(Q_{1/3/5})$. Because the peaks are purely real for the $\mathcal{C}_2\mathcal{T}'$-invariant states, we get

$$\text{ang}[\rho(Q_j)] = \theta_{\rm IVC} \mod \pi. \tag{C.28}$$

In practice, we do not know the position (r_c) of the $\mathcal{C}_2$-rotation center precisely with respect to an origin of the lattice, which induces an arbitrary phase shift $\rho(Q_j) \to e^{iQ_j\cdot r_c}\rho(Q_j)$. To eliminate this origin-dependence, we can take a product of the peaks whose total momentum is zero. $\{Q_0, Q_2, Q_4\}$ is one such combination, so we obtain

$$\text{ang}[\rho(Q_0)\rho(Q_2)\rho(Q_4)] = 3\theta_{\rm IVC} \mod \pi. \tag{C.29}$$

Thus, $\theta_{\rm IVC}$ can be determined up to $\pi/3$ ambiguity. In Fig. C.2, we show the total LDOS and total FTLDOS of three different K-IVC$_B$ states obtained via invoking valley rotations to the Hartree-Fock density matrix: (i) (approximately) $\mathcal{C}_2\mathcal{T}'$-invariant state, (ii) $\mathcal{C}_2\mathcal{T}$-invariant

state, and (iii) $\mathcal{C}_2\mathcal{T}''$-invariant state at $\Delta\theta = 23.61°$. By using Eq.(C.29), we extract $\theta_{\rm IVC} = -2.34°$, $27.72°$, $21.29°$ mod $60°$ respectively, which matches with the expectations up to a small error $\sim \mathcal{O}(1°)$.

Let us comment a few noteworthy aspects about the extraction procedure. First, the FTLDOS peaks are typically broadened from the existence of Moiré-scale modulations in LDOS (e.g. due to smooth change of sublattice polarization textures), and may exhibit phase variations across nodal lines in vicinity of the peaks. In such cases, even if we choose $\rho(\mathbf{q} = Q_j + \epsilon_j)$ with small deviations $\epsilon_j \sim \mathcal{O}(\mathbf{g})$, the extraction procedure will still be robust as long as $\epsilon_0 + \epsilon_2 + \epsilon_4 = 0$. Second, even when the system lacks an exact $\mathcal{C}_2$-symmetry (e.g. D_3-configuration, see Fig. C.4), the above procedure can still be used to extract $\theta_{\rm IVC}$ because slowly varying part of the DOS retains an approximate $\mathcal{C}_2$-symmetry about some honeycomb plaquette near the very center of the AA-region. This allows us to leverage the origin-independence. Nevertheless for the AB/BA-regions, there exists no such $\mathcal{C}_2$-invariant center, so the extraction procedure above will be inapplicable. This is in contrast to the case of monolayer graphene which always has a local $\mathcal{C}_2$-invariant center.

We note that the local extraction of $\theta_{\rm IVC}$ in different AA-regions can in principle be used to detect translation-breaking order of the IKS states. The IKS breaks translation-symmetry of the Moiré lattice but instead enjoys a "screw"-like symmetry along the translation-broken direction (e.g. $\propto \mathbf{L}_1$), which combines the translation $\mathbf{L}_1$ followed by a valley rotation [12]. This manifests as different Kekulé patterns at different Moiré unit cells, as valley rotation takes $\theta_{\rm IVC} \to \theta_{\rm IVC} + 2\pi/M$, where $M \sim 3$ depends on model detail [12]. However, we expect this extraction to be difficult in practice because (i) M is expected to be close to 3, which suffers from $\pi/3$ ambiguity and (ii) the Moiré lattice is not commensurate at generic strain and twist angle.

C.6 Spin structure at $|\nu| = 0, 2$

In this section, we discuss the behavior of K-IVC in the presence of the spin degree of freedom s^μ. Most theoretical models discussed in the literature have an enhanced $SU(2)_+ \times SU(2)_-$ symmetry in which spins can be rotated independently within each valley. The sign of the small "Hund's" coupling which breaks this symmetry down to the global spin-rotation $SU(2)$ is unknown, but regardless we may expect one of two scenarios [8, 130]. The most natural case is a "ferromagnetic" Hund's coupling, which prefers a singlet state ($\nu = 0$) or a spin polarized state ($|\nu| = 2$). Because the STM signal is additive across spin-species, the discussion in the main text is unchanged.

On the other hand, "anti-ferromagnetic" (AF) states are obtained by starting from the ferromagnetic case and applying a π-spin rotation about some axis $\hat{n}$ in only *one* of the two valleys. For non-IVC states this rotation leaves the order (and hence the LDOS) unchanged, but for the IVC states the inter-valley coherence transforms from $\tau_{x/y} \to \tau_{x/y}(\hat{n}\cdot\mathbf{s})$ where $\hat{n}$ is 1) arbitrary for $\nu = 0$, and 2) perpendicular to the spin direction for $|\nu| = 2$. This effectively shifts the IVC phase $\theta_{\rm IVC}$ by π between the two spin-species, changing our conclusions. At

both $|\nu| = 0, 2$, the AF K-IVC state is symmetric under the unitary $U_{\hat{n}} \equiv \tau_z R^{\pi}_{\perp}$, where $R^{\pi}_{\perp}$ is a π spin-rotation about 1) any axis perpendicular to $\hat{n}$ for $\nu = 0$, or 2) the original spin axis for $|\nu| = 2$. The Kekulé -signal is odd under $U_{\hat{n}}$, enforcing an extinction. Unlike $\mathcal{T}'$, the perturbation $H_{\text{pert}} = E_B C$ is *even* under $U_{\hat{n}}$, so within this approximation the Kekulé -signal remains absent even for $B > 0$.

Fortunately, a magnetic field will also couple through a spin-Zeeman field, $H_{\text{pert}} = E_B C + E_Z s^z$. The spin-orientation of the AF K-IVC will in general lock and cant with E_Z, breaking $U_{\hat{n}}$ and allowing the Kekulé pattern to appear. Assessing the magnitude in this case requires a detailed knowledge of the Hund's coupling [131], which we thus leave to future work.

C.7 Supplementary numerical data

DSM/VP$_0$/VP$_B$/VH: LDOS and DOS spectrum

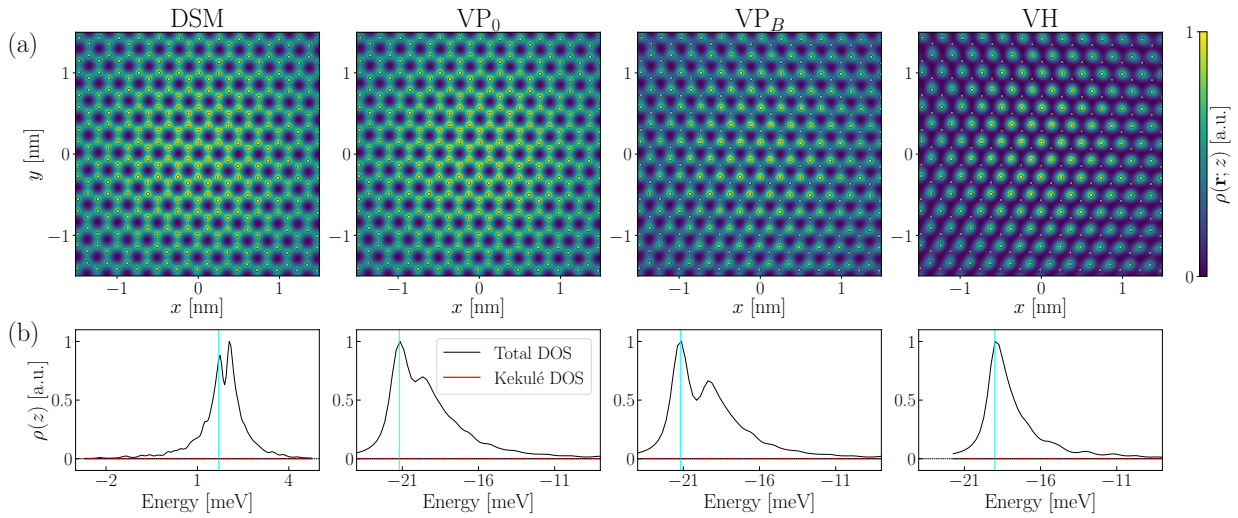

Figure C.3: Spectroscopy calculation results for the spinless DSM states and self-consistent HF solutions of the spinless VP$_0$, VP$_B$, VH states at charge-neutrality ($\nu = 0$). We present (a) total LDOS $\rho(\mathbf{r}; z)$, (b) total and Kekulé -DOS $\rho(z = E + i\eta)$ signals for the bottom layer AA-region of MATBG. The signals are normalized by their maximum. For DSM we set the Lorentzian broadening parameter $\eta = 0.1\,\text{meV}$, while for VP$_0$, VP$_B$, and VH we set $\eta = 0.5\,\text{meV}$. The scanning-energies $E = 1.7, -21.2, -21.2, -19.0\,\text{meV}$ (cyan lines in (b)) are chosen respectively for each phase to compute LDOS. For DSM, DOS signals for an energy window encompassing both the filled/empty bands are shown in (b), so that the two van-Hove singularity peaks originate from the occupied/empty states respectively. For VP$_0$, VP$_B$, and VH, energies below $-8\,\text{meV}$ are presented to show DOS signals for the occupied states. White dots in (a) denote carbon lattice sites.

In Fig. C.3, we present numerical LDOS/DOS data for several candidate ground states at charge-neutrality ($\nu = 0$) in the spinless model which preserve valley-dependent phase

rotation symmetry $U_V(1)$: symmetric Dirac semimetal (DSM); valley-polarized without perturbation (VP_0); valley-polarized with small perpendicular magnetic field (VP_B); valley-Hall (VH). The DSM band-structure is obtained from the non-interacting Bistritzer-Macdonald (BM) model. $\mathrm{VP}_0/\mathrm{VP}_B/\mathrm{VH}$ states are obtained by performing self-consistent Hartree-Fock (HF) calculations on the spinless interacting BM model (See Table. C.1 for details on HF calculations). For VP_B, the effect of a perpendicular magnetic field was modeled by $E_B \approx 0.5\,\mathrm{meV}$ between the $C = \pm 1$ Chern-polarized VP_0 states. We have omitted including the FTLDOS, as we only observed featureless Bragg peaks for these states.

We now describe the qualitative features of each phase observable from the numerical data.

(iv) DSM: The ground state of the non-interacting BM model [4] (or a dressed version thereof) respects all symmetries of MATBG. In particular, it has $\mathcal{C}_3$ and $U_V(1)$ symmetry, which prohibits a nematic axis and Kekulé signal, respectively. The LDOS is indeed fully symmetric.

(v) $\mathrm{VP}_0/\mathrm{VP}_B$: The valley-polarized state VP_0 is obtained by doubly occupying one valley (e.g. $|\tau = 1, C = 1\rangle$, $|\tau = 1, C = -1\rangle$), breaking $\mathcal{C}_2$ and $\mathcal{T}$ while preserving $\mathcal{C}_3$ and $\mathcal{C}_2\mathcal{T}$. $\mathcal{C}_2\mathcal{T}$ rules out sublattice polarization, so the LDOS is fully symmetric, as can be confirmed from the numerical LDOS. However, when $B > 0$, $\mathcal{C}_2\mathcal{T}$ is broken and we expect sublattice polarization to emerge in a narrow range of tunneling bias ($\sim E_B$) close to the van-Hove (vH) singularity. We indeed observe a substantial sublattice polarization for VP_B near the lower vH singularity. As discussed for the K-IVC in the main text, this reflects the sublattice-polarized nature of the Chern-polarized states.

(vi) VH: The valley-Hall state is obtained by occupying either the $\sigma = A$ or B sublattice (e.g. $|\tau = 1, C = 1\rangle$, $|\tau = -1, C = -1\rangle$), breaking $\mathcal{C}_2$. We thus expect strong sublattice polarization, with opposite sign in the filled / empty DOS. In the numerical LDOS, we indeed see a highly sublattice-polarized signal.

K-IVC$_B$: LDOS/FTLDOS for D_3-configuration

In order to confirm that our predictions do not rely on the detailed geometry (in particular the existence of an exact $\mathcal{C}_2$-symmetry at the AA-region) of a TBG lattice, we performed LDOS calculations on MATBG in the D_3-configuration (Fig. C.4(a)). For concreteness, we computed LDOS/FTLDOS for approximately $C_2\mathcal{T}'$-invariant K-IVC$_B$ states at $E_B = 0.1\,\mathrm{meV}$. As we see in Fig. C.4(b,c), not only are the Kekulé -LDOS patterns are similar to those of D_6-configuration, the same θ_{IVC} can be extracted from the phases of the FTLDOS up to a small error (c.f. Fig. C.2(a)).

K-IVC: magnetic field dependence of the Kekulé -DOS spectrum

In Fig. C.5 we show the total DOS and Kekulé -DOS of K-IVC states under various magnetic fields at $\eta = 0.1\,\mathrm{meV}$. The Kekulé -DOS signal increases approximately linearly as a function of the perturbation strength E_B, and reaches $\sim 10\%$ of the total DOS signal (near the

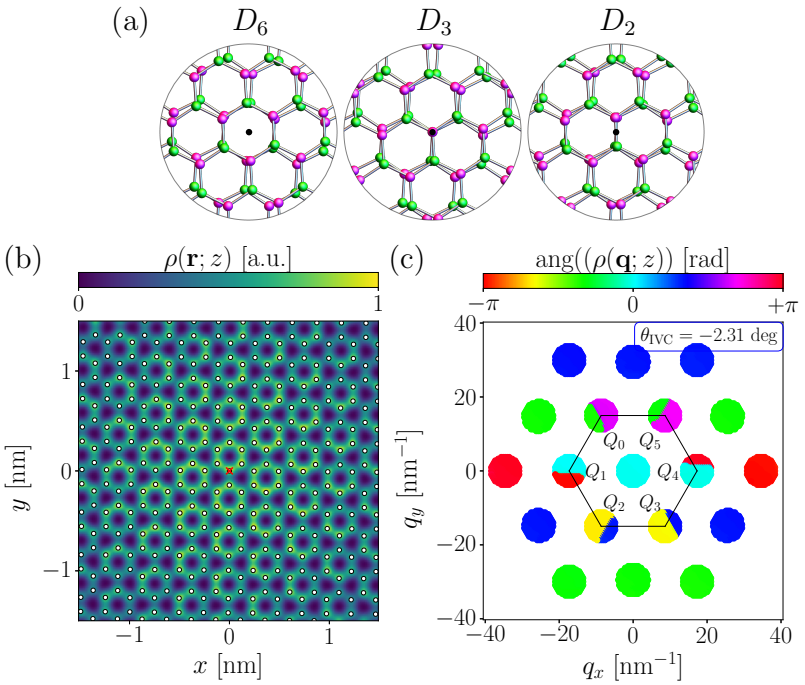

Figure C.4: (a) Zoomed-in view of the AA-region of MATBG in various lattice configurations at twist angle $\theta \sim 7.34°$. Each configuration is generated by choosing a plaquette-, site-, and bond-center as the rotation-center, and respects symmetries of the point group D_6, D_3, and D_2, respectively. (b) Total LDOS $\rho(\mathbf{r}; z = E + i\eta)$ and (c) phases of total FTLDOS $\rho(\mathbf{q}; z)$ for the spinless, approximately $\mathcal{C}_2\mathcal{T}'$-invariant K-IVC states at CNP under magnetic field $E_B = 0.1\,\mathrm{meV}$, defined on a MATBG in D_3-configuration. Using Eq.(C.29), we extract $\theta_{\mathrm{IVC}} = -2.31°$ mod $60°$. The data shown is for the AA-region of bottom layer, at $E = -19.8\,\mathrm{meV}$ and $\eta = 0.1\,\mathrm{meV}$.

energies indicated by the dotted vertical lines) at $E_B = 0.1\,\mathrm{meV}$. This is consistent with our prediction in the main text that $E_B \gtrsim \eta$ is necessary for observing substantial Kekulé signal.

nSM: comparison of the full DOS spectrum and charge-density signals at different heterostrain parameters

We show in Fig. C.6 the total DOS spectrum and the energy-integrated LDOS (charge-density) $\rho(\mathbf{r}) = \int \mathrm{d}E \rho(\mathbf{r}; E)$ of the conduction/valence band (CB/VB) for the two distinct nSM states at CNP, computed at heterostrain parameters [91] (a) $\epsilon = 0.1\%$ and (b) $\epsilon = 0.5\%$. Via shape distortion and Moiré-scale spatial distribution of the charge-density signals in the AA-regions, we can observe the global charge-nematicity and the effect of strain. Furthermore, we observe that CB↔VB switches its nematic axis; following Ref. [33], this feature can be quantified by measuring the 'net-charge' $\Delta\rho(\mathbf{r}) = \rho_{\mathrm{VB}}(\mathbf{r}) - \rho_{\mathrm{CB}}(\mathbf{r})$ (Fig. C.7), where the blue/red signifies the degree of electron/hole doping. We see clearly the emergence of a stripy, quadrupolar net-charge order at the AA-regions (more prominently for $\epsilon = 0.5\%$),

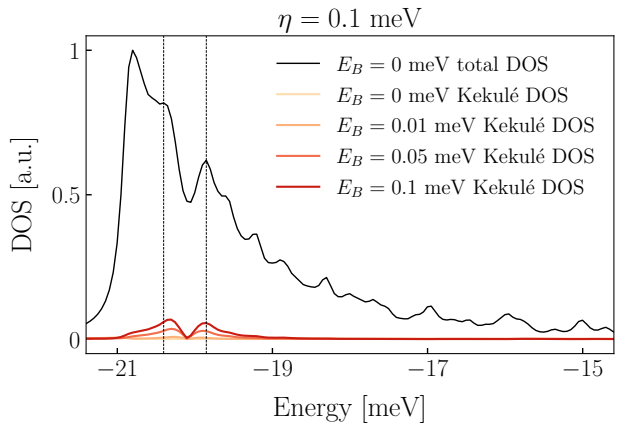

Figure C.5: Total DOS $\rho(z = E + i\eta)$ and Kekulé -DOS $\rho^{\text{Kekulé}}(z)$ (Eq.(C.15)) spectrum of the valence bands for the spinless K-IVC states at CNP under various magnetic fields, at $\eta = 0.1$ meV. Dotted vertical lines identify two sub-peaks ($\sim -20.4, -19.9$ meV) within a van-Hove singularity peak of the valence-bands.

which qualitatively matches with an experimental data [33].

We show in Fig. C.8 the graphene-scale charge-density of the CB/VB for the same nSM states shown in Fig. C.6 at (a) $\epsilon = 0.1\%$ and (b) $\epsilon = 0.5\%$, focusing on the very center of the AA/AB/BA-regions in bottom layer. From the AA-region, we see that the direction of local bond-anisotropy switches as VB↔CB for both strain values, in a similar spirit to the switch of nematicity observed in Moiré-scale signals. At the AB/BA-regions the signals are dominantly sublattice B/A-polarized, same for the CB/VB. This can be explained from the chiral limit phenomenology of the valley/Chern basis $|\mathbf{k}, \tau, C\rangle$ [7, 8] for the flat bands which are $\sigma = A/B = C\tau$-polarized; as shown by Ref. [7], each A/B-polarized flat band wavefunction then has zero density at the AB/BA-region respectively, resulting in local sublattice polarization. This phenomenology survives away from the chiral limit, as evidenced by the polarization of CB+VB.

Comparing the strain-dependence of the AB/BA-region signals, we see a more striking feature, the prominence of B/A-centered "tadpole-like" bond-anisotropy along a zigzag direction ($\pm 60°$ from the y-axis) for $\epsilon = 0.5\%$, in contrast to the strong equal-weight bond-anisotropy observed in the AA-region for both heterostrain values. A similar qualitative feature has been observed in experiment as well [33]. Such stripy bond-nematicity in the AB/BA-regions (with graphene translation symmetry) could be a signature of a non-IVC phase stabilized under a weak strain. Along with the quadrupolar net-charge distributions shown in Fig. C.7, our observations suggest that strain significantly alters the charge order of an nSM state.

We comment that the observed bond-nematicity patterns should be sensitive to choice of the Wannier orbitals and direction of the applied strain, which can enter as tuning parameters for reproducing experiment.

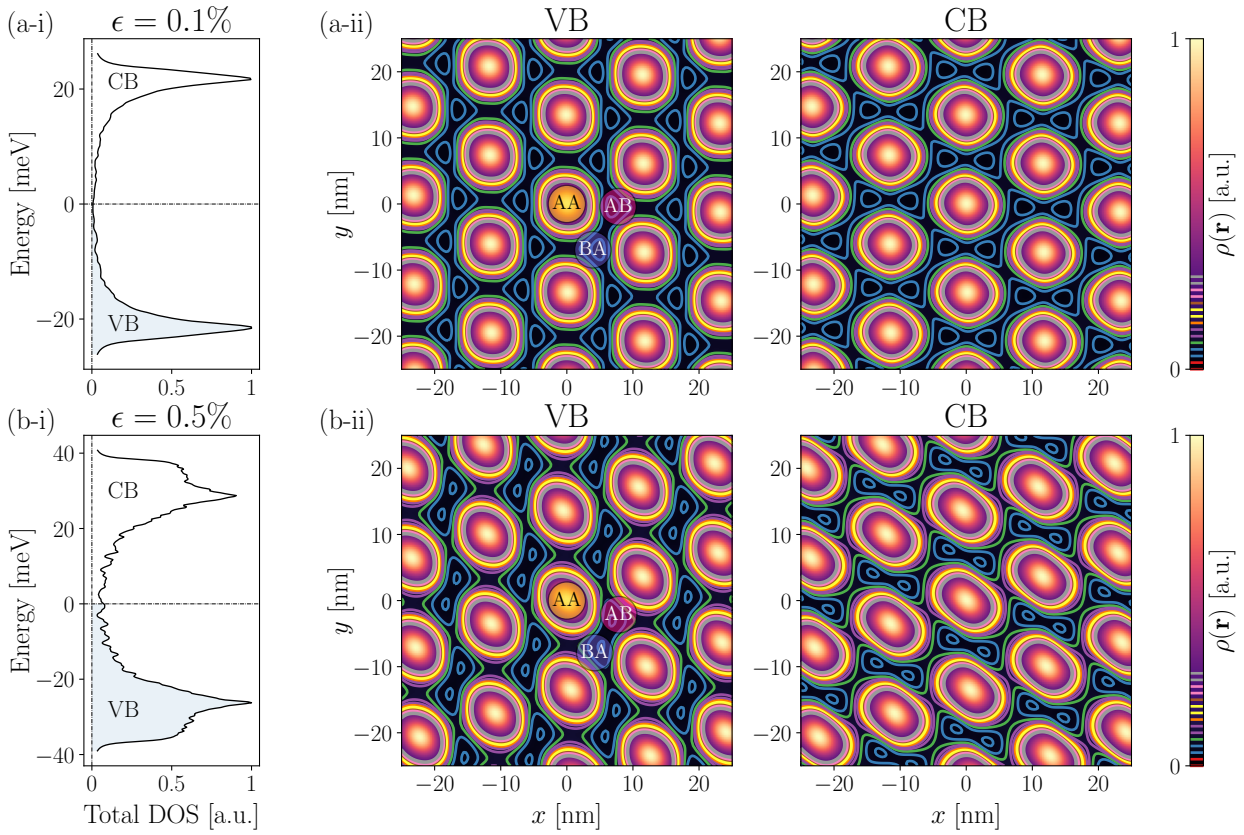

Figure C.6: (i) Total DOS $\rho(z = E + i\eta)$ spectrum with $\eta = 0.5\,\text{meV}$ and (ii) total charge-density $\rho(\mathbf{r})$ of the conduction/valence bands (CB/VB) for the two spinless nSM states at CNP, obtained at heterostrain parameter (a) $\epsilon = 0.1\%$ and (b) $\epsilon = 0.5\%$. The electrons fill 2 bands out of the 4 bands (VB, shaded blue area of (a-i,b-i)). The colored contour lines in (a-ii,b-ii) represent the iso-signal contours within [0.0, 0.3]-range of the normalized $\rho(\mathbf{r})$. The data shown is for the bottom layer.

IKS: full DOS spectrum and charge-density signals at the AA/AB/BA-regions

We show in Fig. C.9 the total DOS and Kekulé -DOS spectrum of the spinless IKS states at $\nu = -1$ and heterostrain $\epsilon = 0.7\%$. There are 12 bands total available due to three-fold translation symmetry breaking along $\mathbf{L}_1$ [12]. The IKS is an insulating state at $\nu = -1$ with a band gap $10 - 20\,\text{meV}$, where the electrons fill 3 out of the 12 bands (VB). In contrast to the VB and low-energy conduction bands (CB1) which have a sizable Kekulé -DOS, we find that the Kekulé -DOS signal is significantly reduced for the higher-energy conduction bands (CB2) at $E \gtrsim 30\,\text{meV}$. Because there exists no symmetries such as $\mathcal{T}'$ in IKS which enforce selection rules in $\rho_{\mathbf{q}}$ (Eq.(C.21),(C.25)), the absence of Kekulé -DOS implies that the CB2 has lost intervalley coherence. Such "IVC-depletion" of the IKS has been theoretically analyzed via energetic considerations of the momentum-dependent valley-hybridization pattern, and

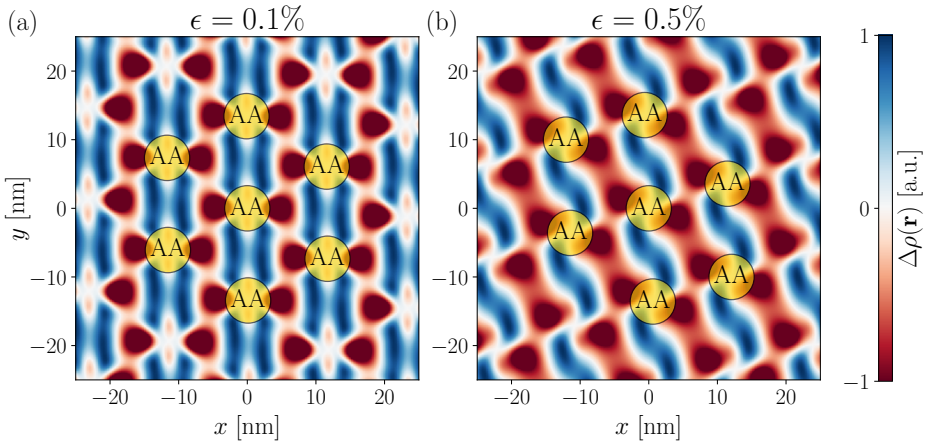

Figure C.7: Net charge-density signal $\Delta\rho(\mathbf{r}) = \rho_{\mathrm{VB}}(\mathbf{r}) - \rho_{\mathrm{CB}}(\mathbf{r})$ for the nSM states shown in Fig. C.6, at heterostrain parameter (a) $\epsilon = 0.1\%$ and (b) $\epsilon = 0.5\%$. The data shown is for the bottom layer.

is consistent with high valley-polarization predicted for the upper bands (see Ref. [12] for detail.)

We show in Fig. C.10 the graphene-scale charge-density of the valence/conduction bands (VB, CB1, CB2) for the same IKS states at the very center of the AA/AB/BA-regions. For CB2, we find that the Kekulé pattern disappears as expected from the vanishing Kekulé - DOS while the signal resembles those of the nSM conduction bands (c.f. Fig. C.8), indicating a non-IVC but nematic charge order. For VB and CB1, we see clear $\sqrt{3}\times\sqrt{3}$ Kekulé patterns as well as sublattice polarizations in the AB/BA-regions. The equal-weight bond-anisotropy in the AA-region and the stripy "tadpole-like" bond-anisotropy in the AB/BA-regions are also observed. Such resemblances to the nSM charge order under the heterostrain $\epsilon = 0.5\%$ (c.f. Fig. C.8) shows that a strain leaves sharp density fingerprints on IVC states as well, via bond-anisotropic charge order.

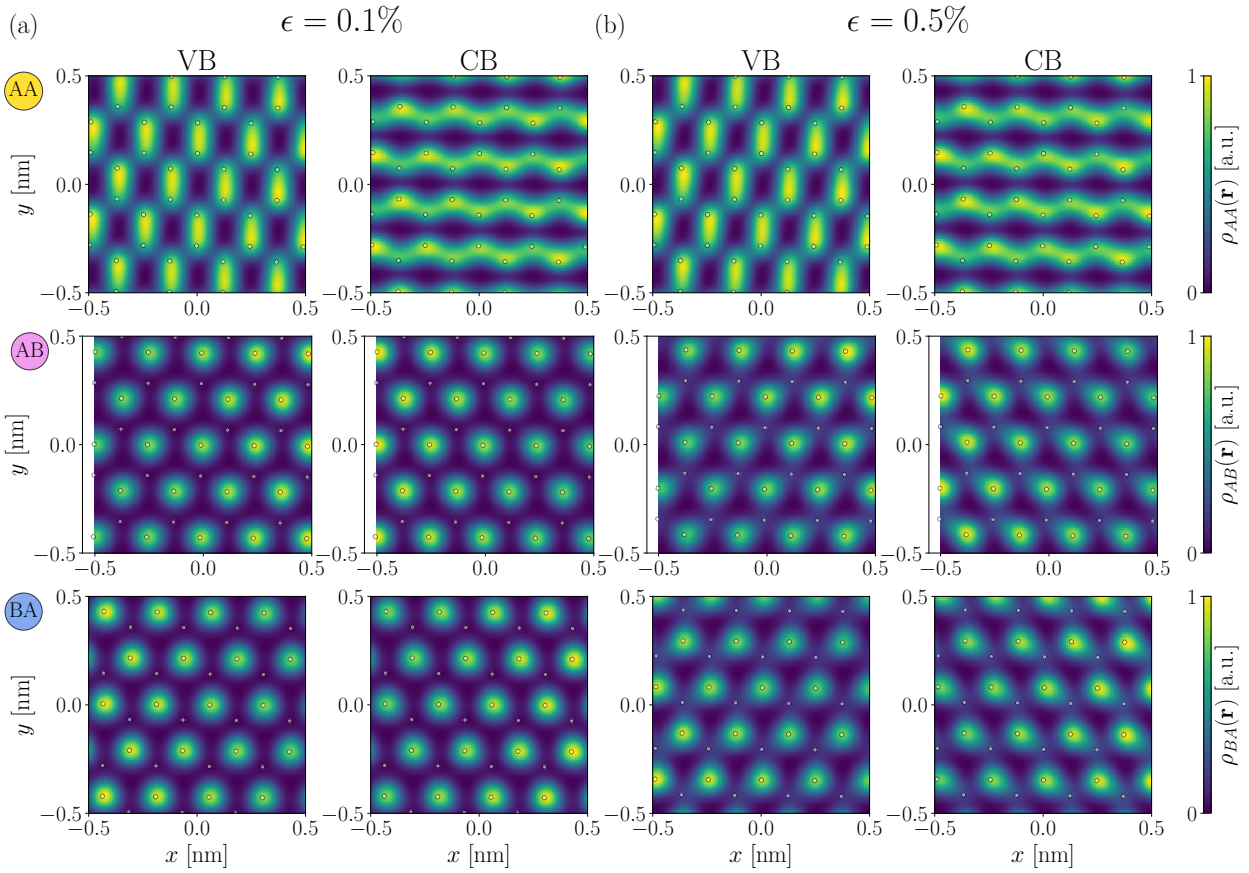

Figure C.8: Graphene-scale charge-density $\rho(\mathbf{r})$ of the conduction/valence bands (CB/VB) for the nSM states shown in Fig. C.6, at heterostrain parameter (a) $\epsilon = 0.1\%$ and (b) $\epsilon = 0.5\%$. Subplots at each row are centered at the AA/AB/BA-regions of the strained MATBG lattice, depicted in Fig. C.6(a-ii,b-ii). The data shown is for the bottom layer.

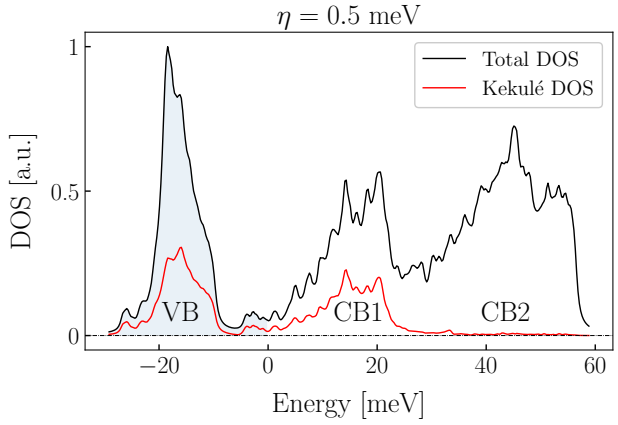

Figure C.9: Total DOS $\rho(z = E + i\eta)$ and Kekulé -DOS $\rho^{\text{Kekulé}}(z)$ (Eq.(C.15)) spectrum of the spinless IKS states at filling $\nu = -1$, $\eta = 0.5\,\text{meV}$, and heterostrain $\epsilon = 0.7\%$. The electrons fill 3 valence bands (VB, shaded blue area) out of the 12 bands to form an insulating state. The conduction bands are grouped into CB1 and CB2 separated by a dip near 30 meV, corresponding to holes filling 3 and 6 bands respectively.

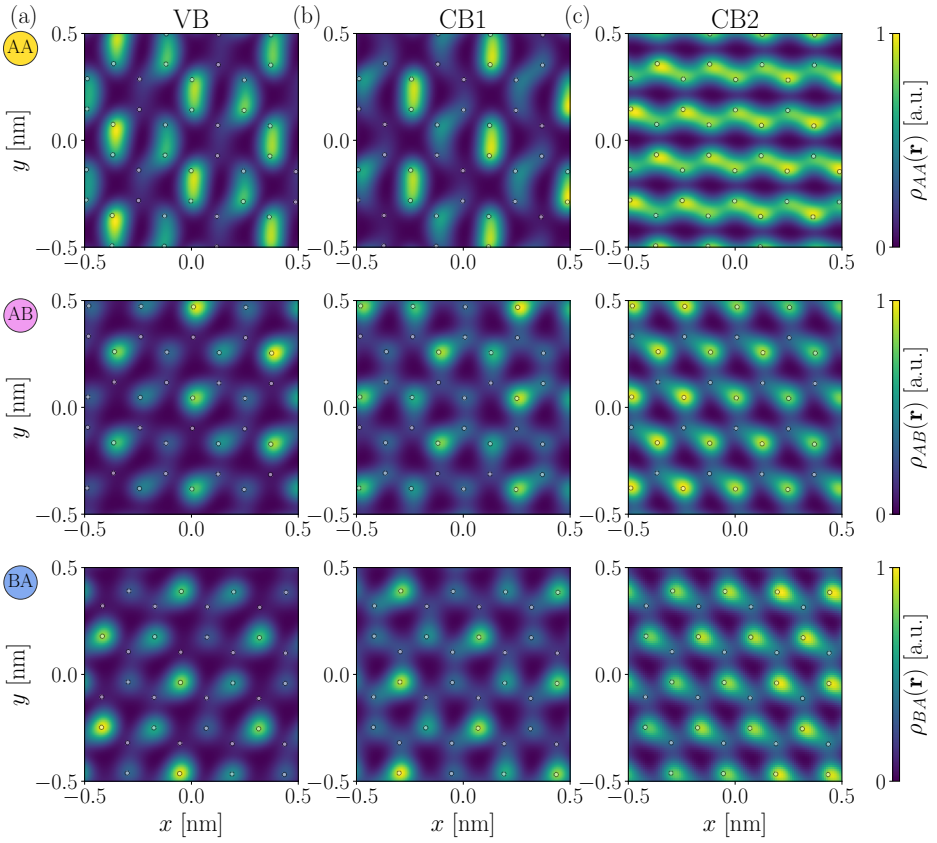

Figure C.10: Graphene-scale charge-density $\rho(\mathbf{r})$ of the valence/conduction bands (a) VB (b) CB1 (c) CB2 for the IKS states shown in Fig. C.9, at filling $\nu = -1$ and heterostrain $\epsilon = 0.7\%$. Subplots at each row are centered at the AA/AB/BA-regions of the strained MATBG lattice (c.f. Fig. C.6(a-ii,b-ii)). The data shown is for the bottom layer.